Newcastle University, Biosciences Institute
Framlington Place, Newcastle upon Tyne NE2 4HH

Computational modelling and experimental investigation of retinal tissue self-organisation

Thesis submitted for the Degree of
Doctor of Philosophy

Supervised by Dr. Roman Bauer and Prof. Evelyne Sernagor

Jean de Montigny
3 year Full time PhD

Submitted in May 2020

Abstract

Individual retinal cell types exhibit semi-regular spatial patterns called retinal mosaics. These mosaics could enable uniform sampling of visual information and are formed to varying degrees across cell types. Retinal ganglion cells (RGC) and amacrine cells are notably known to exhibit such layouts. RGCs dendritic arbours also form organised structures, laminating at different levels and exhibiting specific morphologies depending on the considered type.

Mechanisms responsible for the formation of such organised structures and their requirements are still not well understood. Mosaic formation follows three main theories: (1) homotypic cells prevent nearby cells from adopting the same type, (2) cell tangential migration, with homotypic cell repulsion, (3) cell death (with RGCs exhibiting high rates of apoptosis).

Here, we use BioDynaMo, an agent-based simulation framework, to build a detailed and mechanistic model of mosaic formation. In particular, we investigate the implications of the three theories. We report that the cell migration mechanism yields the most regular mosaics. We also found that cell death can create regular mosaics only if the death rate is kept below 30%, after which cell death have a negative impact on mosaic regularity. We also investigate the implication of intrinsic and extrinsic factors in the development of RGC dendritic tree morphologies.

Waves of spontaneous activity sweep across the RGC layer from postnatal day (P) 0-10 and may drive the development of some cellular features (mosaic, dendritic lamination). Using a combination of immunohistochemistry and pan-retinal activity recording, we report transient clusters of auto-fluorescent cells around the optic disc during the period of cholinergic waves. They migrate towards the periphery between P2-9 and then disappear, coincidentally with the switch from Stage II to stages III waves. Waves origin follow a similar centre-to-periphery developmental pattern. We propose here that these clusters represent activity hotspots and are the sites for wave initiation.

Acknowledgements

First, I would like to thank my supervisor Dr. Roman Bauer for giving me the opportunity to conduct my PhD at the Newcastle University, and to do a fruitful one-month placement at CERN openlab. I gratefully acknowledge Newcastle University for funding my PhD through the Research Excellence Academy (REA) Postgraduate Research Studentship.

I would like to thank Prof. Evelyne Sernagor, my second supervisor, for the support and encouragement she gave me, but also for always being available and patient with me. Without her guidance and feedbacks this PhD would not have been the same. I want to thank her for making me feel at home and for all the memorable diners at her place with lab members.

I am also thankful to Vasileios Vavourakis for the enriching collaboration we have done and all the hard work he put in. Thanks for your support and advices.

Many thanks go out to the other lab members, especially Vidhya and Gerrit, for their precious help and advices. I also want to thank Melissa for the time we spent together in the lab and for the antibody song.

I want to give a very special thanks to all my friends in Newcastle, who have made these past years a unique and enjoyable period of my life. I want to thank Myrto, for mutually sharing food, for laughing at my terrible jokes, and for being a precious friend, including in difficult times. I want to thank Thomas for the endless discussions and for his support, but also Anderson and Mo, for their warm welcome and for all the time we spent together. I cannot forget to thank all the present and former members of the lunch club, Tamara, Beth, Ashan, Mark, Clare and Felix, for all the laughs and the memorable moments. I also want to thank the friends I made in Switzerland, Lukas and Ahmad for their humour and for their help.

I would also like to thank my friends on the French side, who, despite the distance, have always been here for me. Firstly, Dadou and Baptist, for all their support and for being amazing friends for more than twelve years, but also Antoine, Corentin, Nicolas and Cerise for making me laughs and clearing my mind.

Finally, I want to thank my parents and my siblings, for their unconditional support, for always believing in me, and especially for bearing me during the write up period.

Table of content

List of Figures and Tables

List of abbreviations

AB: Agent-based
CAF: Cancer-associated fibroblast
CD: Cell death
CF: Cell fate
CG: Cancerous glial cell
CM: Cell migration
CN: Closest neighbour
CNS: Central nervous system
DTS: Delaunay triangulation segment length
ECM: Extra cellular matrix
G: Glial cell
GCL: Ganglion cell layer
hCG: Hypoxic cancerous glial cell
LED: Local edge detector
INL: Inner nuclear layer
MMP: Matrix metalloproteinase
Nc: Necrotic cell
Ne: Neuron
OCT: Optimal cutting temperature
OPL: Outer plexiform layer
PBS: Phosphate buffer solution
PDGF: Platelet-derived growth factor
PFA: Paraformaldehyde
RAV: Representative averaging volume
RGC: Retinal ganglion cell
RI: Regularity index
SAC: Starburst amacrine cell
VDA: Voronoi diagram angle
VDR: Voronoi diagram area

Chapter 1. Introduction

The central nervous system (CNS) is a vast and complex assembly of neurons responsible for information integration, resulting in an astonishing variety of phenotypic responses. This highly complex structure emerges from a few progenitor cells that self-organize through precise local developmental rules. Chemical guidance cues and local interactions (including neural activity) interact with genetically encoded rules to regulate this complex assembly and to give rise to the appropriate structure. Many of these mechanisms remain to be fully understood. Using experimental work on neonatal mouse retinas and computational simulations, we address here some of these important points.

This chapter will introduce general knowledge about the retina (its different cell types and its development) and computational modelling of neural development. More precise information about stage II retinal waves, retinal mosaics formation, dendritic development, and the various mechanisms that could be involved to give rise to a coherent retina will also be discussed.

1.1 The Mammalian Retina

As part of the CNS, the retina originates from the same embryonic tissue: the neural tube. During development, out-pocketing structures emerge bilaterally from the neural tube (more precisely from the diencephalon), forming the optic vesicles. The optic vesicle invaginates to form the optic cup. The inner part of this cup forms the neural retina, while the outer part forms the pigment epithelium. During this process, the optic nerve reaches the diencephalon, forming connectivity between the retina and the brain. The retina is the only part of the CNS that is non-invasively accessible and thus represents an ideal region for studying neural function. Originating from the same progenitors and governed by the same developmental principles as the rest of the CNS, it represents an ideal organ for developmental studies as well.

1.1.1 Retinal structure and function

The retina is the light sensitive neural tissue lining the back of the eye. It represents a hollowed sphere of around 40mm in diameter in human, and 3mm in mouse. Light hits the cornea, where it is diffracted, and penetrates the eye through the pupil. It is then diffracted further by the lens, eventually generating an inverted two-dimensional image of the visual world on the retina. Seen through an ophthalmoscope the retina presents several distinctive features. First, a large yellowish disc, the optic disc, or

optic nerve head, where all axonal fibres originating from the retina gather together to form the optic nerve which carries impulses from the retina to the central visual areas. It also contains most of the blood vessels irrigating the retina. The other distinct feature is a dark area devoid of blood vessels called the fovea, located approximatively 16 degrees more nasal than the optic nerve and is the place where high acuity vision is generated (Kolb 1995). This 0.35 mm diameter disc in human contains the highest density of retinal cells and almost half of the optic nerve fibres.

Retinal organisation is notably well-preserved across species (fish, reptiles, birds, mammals), even if some anatomical particularities differ between species (Erskine and Herrera 2014). This allows animal models to be particularly relevant, including for developmental studies (Baker 2013).

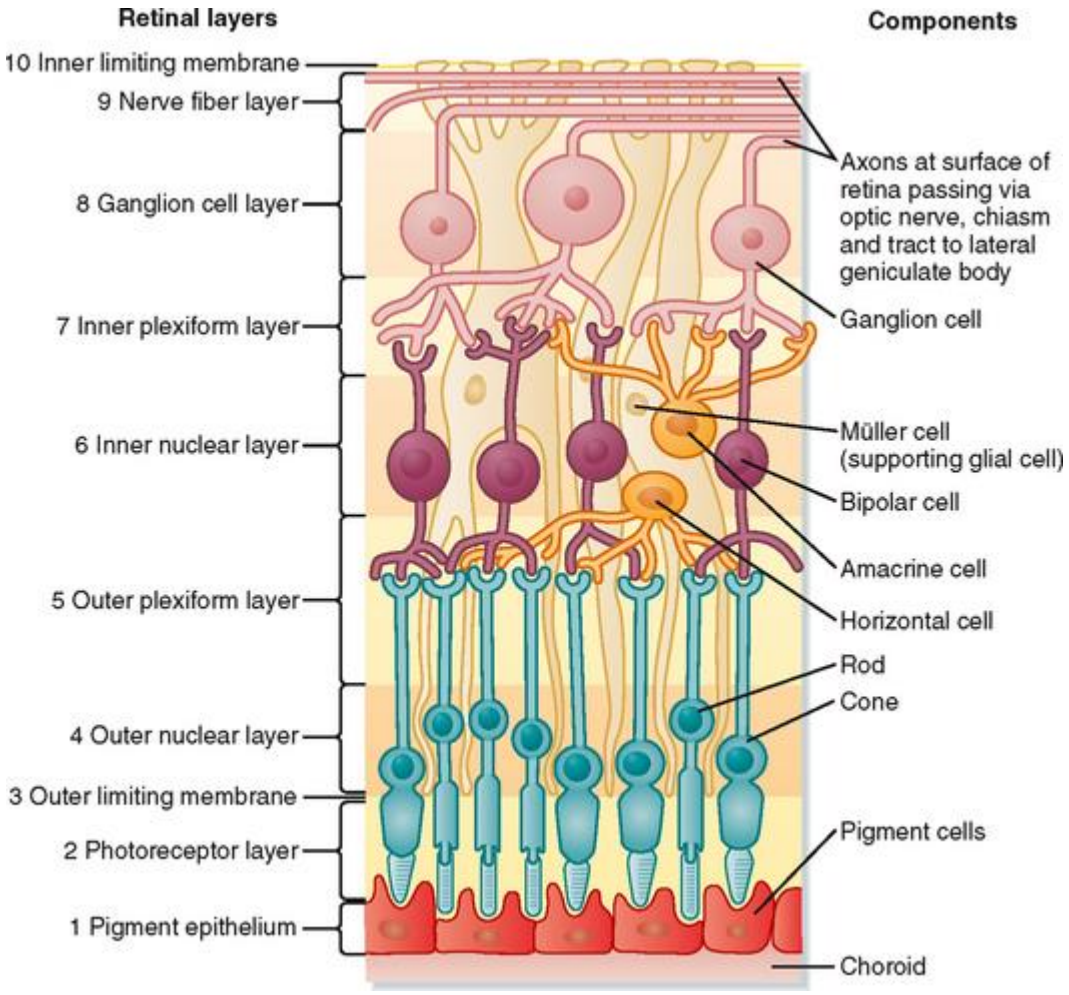

Figure 1: From Berne & Levy Physiology, figure 8-2: Layers of the retina. Light impinging on the retina comes from the top of the figure and passes through all superficial layers to reach the photoreceptors rods and cones. (Koeppen and Stanton 2014).

As the rest of the CNS, the retina is characterised by a complex organisation and connectivity comprising six cellular classes: photoreceptors, bipolar cells, horizontal cells, amacrine cells, ganglion cells (RGCs) and Muller cells. These cells are organised in three nuclear layers and two synaptic (plexiform) layers (see Figure 1). Cell bodies and synaptic connections are strictly laminated.

As represented in Figure 1, photoreceptors cell bodies are located in the outer nuclear layer which establish synaptic connections with bipolar and horizontal cells in the outer plexiform layer (OPL). Bipolar, horizontal and amacrine cell bodies are located in the inner nuclear layer (INL), while the inner plexiform layer (IPL) is where bipolar, RGCs and amacrine cells establish their synaptic connections. More precisely, the IPL itself can be subdivided into two distinct sub-layers, the On and Off sub-laminae. On bipolar cells are depolarised by an increase of light and establish connections with On RGCs in the On layer while Off bipolar cells are depolarised by a decrease of light and establish connections with Off RGCs in the Off layer. The ON layer is closer to the RGC layer (Kolb 1995). Finally, RGC bodies (and some displaced amacrine cell bodies) are located in the ganglion cell layer (GCL). RGCs axons form the optic nerve. They project mainly to the lateral geniculate nucleus of the thalamus and to the superior colliculus.

Photoreceptors

The retina comprises two types of photoreceptors, cones and rods, both with a specialised inner and outer segment involved in phototransduction. The proportion of these two types varies depending on the retinal eccentricity, the centre being rich with cones in species that have a fovea, and the periphery being rich with rods. Rods are specialized in low-light vision, and so are very sensitive (a single photon is able to activate a rod) but have a very low spatial resolution. Cones are less sensitive (a cone needs around 100 photons to respond), but deliver faster responses (better temporal resolution) with a better spatial resolution (Fu and Yau 2007). The presence of more than one type of cone is responsible for the perception of different colours. The photoreceptors inner segment is rich in mitochondria (due to the important energy consumption of photoreceptors), and is connected to the outer segment by a thin cilium. The outer segment is composed of discs containing the visual pigments molecules that will migrate along the outer segment. After 12 days, used discs reach the photoreceptor tip, and, pushed out by more recent incoming discs, are detached from the photoreceptor (Purves et al. 2008). Visual pigments are light sensitive and

responsible for phototransduction in photoreceptors. Contrary to other sensory systems, the activation of a receptor does not set off an action potential, but rather induces a slow, gradual change in membrane potential. Moreover, light will not depolarise the cell, but hyperpolarise it. Indeed, in the dark, there is a constant cationic current (dark current) flowing through Cyclic guanosine monophosphate (cGMP-gated) channels that depolarises the membrane to -40 mV. Upon activation of the photopigments by light, these channels close, resulting in membrane hyperpolarisation to around -65 mV. This is the process of phototransduction (Purves et al. 2008). So, in the dark, photoreceptors are depolarised and release glutamate onto second order neurons. Once triggered by light, they hyperpolarise, resulting in a sharp drop in glutamate release.

Horizontal cells

Horizontal cells are connected specifically with photoreceptors, and respond to them with an inhibitory feedback. They are present in all vertebrates, and have usually two distinct types (Masland 2012b). Those two types present differences both in morphological and molecular features, and can be useful for studying cell type formation. Some types of horizontal cells seem to connect preferentially either to rods or to cones (Boije et al. 2016). Horizontal cells take part in both short and long interactions between photoreceptors, by giving them inhibitory feedback, providing the first level of signal integration. This inhibitory mechanism is crucial for a better perception of contrast and colour opponency (Twig, Levy, and Perlman 2003). Indeed, because horizontal cells widely spread processes, they receive and average the luminosity over a significant area of the retina. If this region receives a lot of light, it will create a strong feedback to the surrounding photoreceptors, inhibiting their response. Because of that, objects surrounding a bright object will have their signal reduced, and so will be less well perceived (Masland 2012b). This mechanism will participate in the creation of the centre-surround receptive fields in the retina.

Bipolar cells

Bipolar cells are glutamatergic neurons, and can be divided into two types depending on the photoreceptor type they connect to. One connects preferentially to rods (rod bipolar cells), and the other, to cones (cone bipolar cells). It is important to note that bipolar cells must also be separated into two functional types, ON-bipolar cells and OFF-bipolar cells. The first type will depolarise in a situation of increased brightness, the second will hyperpolarise. Rod bipolar cells are solely ON-bipolar, while cone

bipolar cells can be either ON-bipolar or OFF-bipolar (Hoon et al. 2014). With those types, three distinct parallel visual information pathways are created at an early stage of the signal processing (cones ON; cones OFF; rods ON). Up to fifteen types of bipolar cells have been identified (Shekhar et al., 2016), having a different response to the photoreceptor input, depending on temporal or structural properties. In this way, each bipolar cell type is able to transmit a different type of information from the photoreceptor to their postsynaptic partners (Masland 2012b).

Amacrine cells

Amacrine cells interconnect bipolar and RGCs, providing inhibition to RGCs and to other amacrine cells. They receive their excitatory input from the bipolar cells. Their main role is to modulate the vertical information pathway (photoreceptors → bipolar cells → RGCs). They integrate, modulate and interpose a temporal domain to the visual message presented to the RGCs (Kolb 1995). Even if the majority of amacrine cells are inhibitory, at least one excitatory type exists, the cholinergic starburst amacrine cell (SAC).

Despite being the more abundant inhibitory neuronal class of the retina, amacrine cells remain one of the most poorly understood retinal cell class (Jacoby et al. 2015). Nowadays, the role of only few amacrine cells in retinal functional circuitry has been fully described, as in the case with the implication in colour-coding (Chen and Li 2012) or steady illumination (Jacoby et al. 2015). Amongst all retinal cell classes, amacrine cells are the most diverse, as illustrated in Figure 2, with more than 30 subpopulations in mammals (Kunzevitzky et al. 2013) complicating the understanding of this heterogeneous cell population. Their morphologies vary from short and thin to long and bushy dendritic tree, having a drastic impact on retinal information processing. The functional necessity of such a huge diversity of amacrine cells remains an open question (Masland 2012a). Amacrine cells can be divided into four categories, depending on their morphology and their dendritic tree size, narrow-field (30-150 µm), small-field (150-300 µm), medium-field (300-500 µm) and wide-field (>500 µm) (Kolb 1995). However, another anatomical and functional criterion is the neurite level of stratification inside the IPL. The stratification level of amacrine cells is thus an important clue for functional classification.

Ganglion cells

RGCs receive and process information form bipolar cells and amacrine cells. They play a primary role, as they are the final retinal cell to receive information, and the only one sending an output from the retina to the brain. They also are the only retinal neurons that generate action potentials, encoding the information into spike trains (Kolb, Fernandez, and Nelson 2016). RGCs can be divided into three basic functional groups, ON, OFF and ON-OFF cells. ON cells receive input from ON-bipolar cells in the ON layer of the IPL and respond to an increase of brightness. OFF cells connect with OFF-bipolars in the OFF layer of the IPL, responding to a decrease in light intensity. ON-OFF cells are bi-stratified, having connections in both ON and OFF IPL layers, and so, responding to both increase and decrease of brightness. However, as well as the amacrine cells, RGCs show a great morphological (see Figure 2) and functional diversity, with over twenty types well identified so far (numerically, morphologically, molecularly and functionally). Every RGC type is believed to carry information about a different visual feature, even if only a few of these types have been fully functionally understood so far (Baden et al. 2016). In any case, RGCs appear to respond particularly well to contrast.

Using multi-electrode array recording from the RGC layer, studies have been able to functionally classify RGCs into more than thirty groups, depending on the stimuli they respond to (Farrow and Masland 2011; Sanes and Masland 2015a). However, more RGC types are still to be discovered (Sanes and Masland 2015; Reese and Keeley 2015; Baden et al. 2016). The fact that some RGCs will respond to a specific stimulus (motion, motion direction, etc) reflects the upstream processing of visual signals.

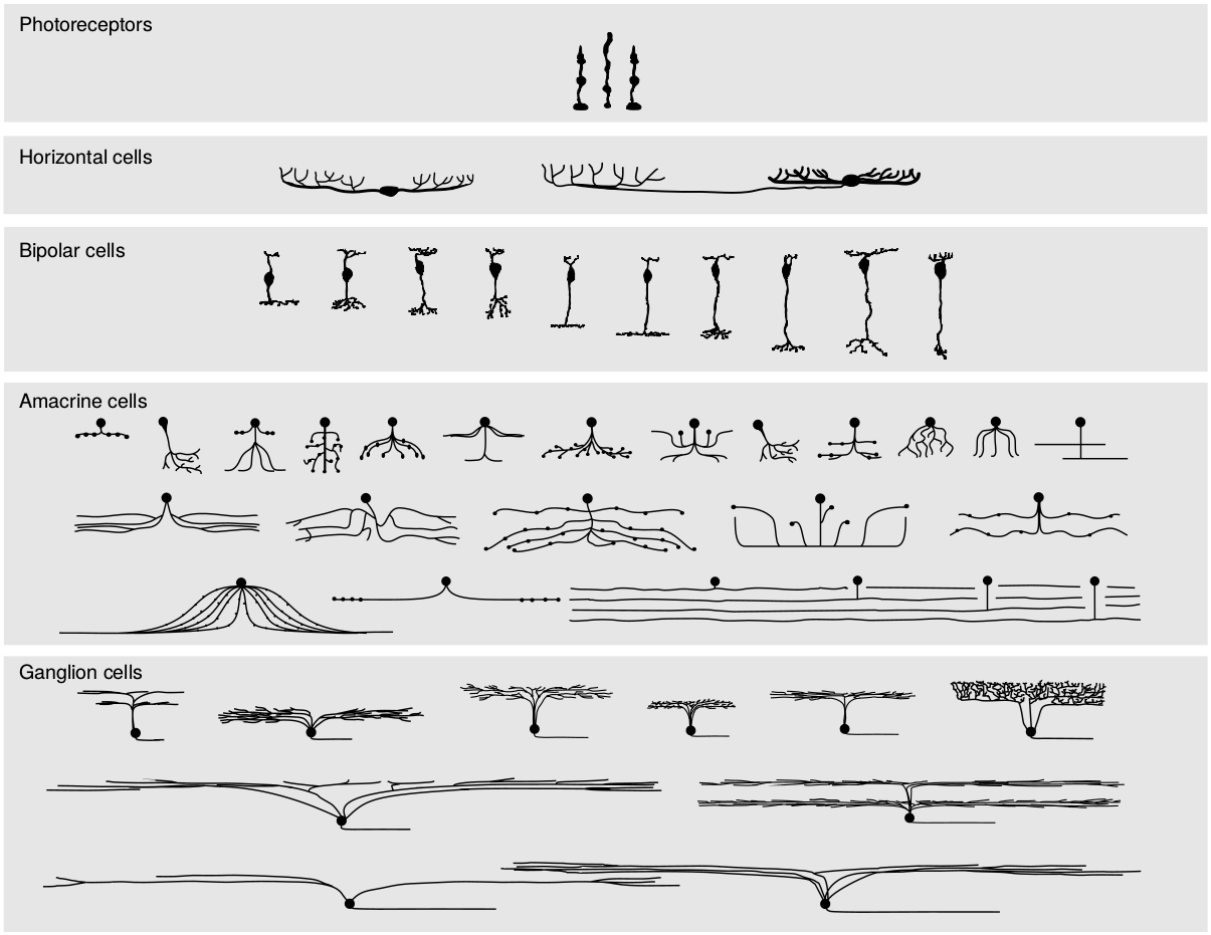

Figure 2: From Masland 2001, figure 1: The major neuronal populations of a generic mammalian retina. Only a subset of the wide-field amacrine and ganglion cells are shown; the total number of cells in the illustration is 49. (R. H. Masland 2001).

Visual pathway

Retinal vertical synaptic connectivity is excitatory (using glutamate), going from photoreceptors to RGCs via bipolar cells. This vertical pathway is modulated by horizontal connections, established by interneurons (horizontal cells and amacrine cells). Those connections use GABA (horizontal and amacrine cells), glycine (amacrine cells), acetylcholine (amacrine cells) and dopamine (amacrine cells) (as well as a whole array of other signalling molecules).

Different cell types are not distributed randomly across the retinal plane, but rather arranged in semi-regular patterns, forming retinal mosaics between homotypic cells. These mosaics concern cells of the same type, and are independent of other cell types (Hoon et al. 2014). Both cell bodies and dendritic fields obey mosaic distribution rules. While the dendritic trees of different cell types frequently overlap, those of same type tile avoiding each other. The formation of mosaics patterns

concerns every cell type within their respective layer (Nguyen-Ba-Charvet and Chédotal 2014). Retinal mosaics could ensure smooth and even coverage across the retina, preventing the formation of perceptual blind spots.

The process of visual information can be divided into three main stages (Masland 2012b). Firstly, rods and cones information is decomposed into more than twelve parallel pathways of information. Secondly, those information pathways are connected to specific RGCs, each RGC type carrying specific visual information. Finally, the modulation of this second stage by bipolar and amacrine cells creates the great diversity and specificity of visual information encoding that is sent to the brain.

1.1.2 Murine retinal development

To generate such a complex layered structure capable of encoding specific visual information, the development of the retina is governed by complex and dynamic mechanisms. All the different retinal cell types arise from the same progenitors, which rely on intrinsic factors to give rise to the correct cell type (Byerly and Blackshaw 2009). Cell type birth and differentiation occurs at different but overlapping times during development. Thus, RGCs are the first to be born, followed by horizontal cells, cones, amacrine cells, rods, bipolar cells and finally Muller cells (Rapaport et al. 2004). This sequence of differentiation and the establishment of connectivity is common is all vertebrate species, mainly varying in terms of gestation length (from hours in zebra-fish to several weeks or months in reptiles and mammals) (Morgan and Wong 2005).

The mouse retina is a widely used model to study retina function and development because it is so amenable to genetic manipulations (Baker 2013), even though there are differences compared with the human retina (mainly in rod/cone proportion and the lack of a fovea, mice being nocturnal). The basic organisation and developmental process are very similar between these species. In addition, and in contrast to primates, rodents (including pups) are born with an immature retina, providing an ideal model for developmental studies.

Cellular differentiation, organisation and dendritic development

RGCs are the first cell class to differentiate in the immature retina, generated in the ventricular zone then migrating to the GCL, where they start extending dendrites towards the IPL. This dendritic growth depends on both intrinsic (genetically encoded) and extrinsic (environmental) factors (Montague and Friedlander 1989;

1991; Hoon et al. 2014). After cell generation and dendritic tree growth, synaptic connections have to be refined. For instance, On-Off pathways require electrical stimulation to become functional (Bodnarenko and Chalupa 1993; Tian and Copenhagen 2003). Indeed, depending on the nature of the input they receive, some bi-stratified RGCs will become mono-stratified (either in the On or Off layer). By this mechanism, bi-stratified cells, representing 65% of RGCs in immature retina, will only represent about 30% in the adult retina (Landi et al. 2007). It is important to note that light deprivation during development leads to a loss of a dendritic pruning mechanism (Tian and Copenhagen 2003; Mehta and Sernagor 2006). Moreover, RGCs are the only cell class notably more numerous in the immature retina compared to the adult retina. Indeed, around 60% of newly born RGCs undergo programmed cell death (apoptosis) during the perinatal period (Farah 2006). Interestingly, not much is known yet about the impact of RGC apoptosis on the maturation of retinal circuitry and visual pathways.

The differentiation of RGCs is closely followed by amacrine cells. Their progenitors are born close to the pigment epithelium and then migrate close to RGCs where they differentiate into amacrine cells (Chow et al. 2015). We still do not know whether the huge amacrine cell diversity seen in the adult retina is predetermined by intrinsic factors (nature), by the external environment (nurture) or by a combination of both (Kunzevitzky et al. 2013). Yet, there is some evidence that both nurture (Godinho et al. 2005), and nature (Kunzevitzky et al. 2013) mechanisms are involved. During the formation of amacrine cells dendritic arbours, dendrites will preferentially innervate either the On or the Off part of the IPL, even if initially their arborisation is diffuse across the entire IPL (Godinho et al. 2005). Importantly, even in the absence of RGCs, amacrine cells are able to laminate correctly into On and Off IPL layers, indicating that cues needed for proper lamination of their dendrites could be independent of RGCs (Godinho et al. 2005; Hoon et al. 2014). However, interactions between amacrine cells alone appear to be sufficient to explain the formation of the IPL sub-laminae (Kay et al. 2004).

RGCs and amacrine cells are the first cells to develop a dendritic arbour and to establish connections in the future IPL. During wiring of the developing IPL, amacrine cell dendrites are believed to provide important developmental cues for the stratification of other cell types (Kay et al. 2004). Around Postnatal day (P) 14, the IPL already exhibits all its sub-laminae, demonstrating its functional maturation (Nguyen-Ba-Charvet and Chédotal 2014).

Horizontal cells are also one of the first cell classes to differentiate. Their progenitors are born close to the pigment epithelium and later migrate to the inner part of the INL (close to RGCs) where they differentiate into horizontal cells. Then, they migrate back to their laminar location, on the outer edge of the INL, close to the OPL (Chow et al. 2015) where they will establish their connections with photoreceptors. In the absence of amacrine cells, horizontal cells seem unable to do their retrograde migration (Boije et al. 2016) indicating a developmental cue from amacrine cells. In the absence of amacrine cells, horizontal cells adopt morphologies close to amacrine cells, without adopting their functional properties. A retinal model without photoreceptors exhibits horizontal cells sprouting in the ONL, thus showing the key role of photoreceptors in the establishment of the OPL.

In rodents, as in other mammals, photoreceptors are the third cell class to be born (Rapaport et al. 2004). However, they establish their connections later in development, first with horizontal cells, forming the OPL (Hoon et al. 2014). Their connections to bipolar cells arise later on in development. In mouse, the OPL formation starts around P4 (Nguyen-Ba-Charvet and Chédotal 2014). After their proliferation phase, photoreceptor's outer segment does not change diameter later on, but they elongate rapidly toward the pigment epithelium from P11-17, reaching their adult length around P19-25 (Fu and Yau 2007). Photoreceptors can already transduce light into electrical signals before eye-opening (at P12 in mouse), but responses to light will gain in robustness as development progresses after eye-opening (Hilgen et al. 2017).

Bipolar cells are the last neuronal cell class to differentiate. They interconnect between the outer and inner retina, making connections both in the OPL and IPL. These excitatory cells require the presence of photoreceptors to laminate in the correct synaptic layer, suggesting a strong developmental cue from photoreceptors (Nguyen-Ba-Charvet and Chédotal 2014). However, they are able to laminate correctly even in the absence of RGCs and amacrine cells (Hoon et al. 2014).

Figure 3 illustrates the temporal steps of cell differentiation and vertical (apico-basal) migration. The precise timing and location of proliferation and differentiation play an important role in the molecular and morphological properties of newly born cells. Thereby, correct cellular lamination during development is mandatory to grow a functional retina (Hoon et al., 2014).

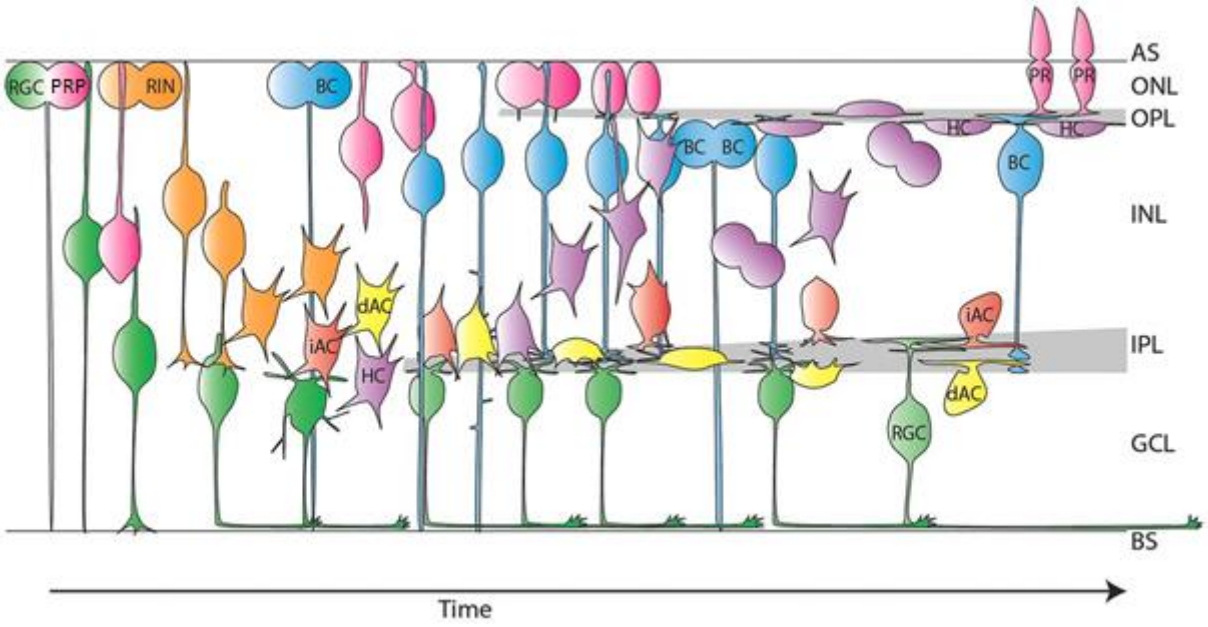

Figure 3: From Chow et al. 2015, figure 10: Model of retinal inhibitory neuron (RIN) migration. All RIN types migrate via bipolar morphologies away from the apical surface before transitioning to multipolar morphology. They gather as a single population in the middle of the retina until the IPL starts to form. Horizontal cells (HCs) then migrate apically and divide en route to, or at, the outer plexiform layer (OPL). HCs sometimes migrate into the outer nuclear layer (ONL) before taking on mature morphology in the inner nuclear layer (INL). Inner nuclear layer amacrine cells (iACs) stabilize processes at the apical side of the bipolar cell (BC) plexus, whereas displaced amacrine cells (dACs) preferentially localize processes to the interface between BC axons and retinal gangion cells (RGC) dendrites before moving into the ganglion cell layer (GCL). AS, apical surface; BS, basal surface; PRP photoreceptor progenitor; PR, photoreceptor. The model shown takes into account results from chow et al. 2015 and previous studies (Choi et al. 2010; He et al. 2012; Mumm et al. 2006; Randlett et al. 2013; Suzuki et al. 2013; Weber et al. 2014).

Molecular guidance

Chemical (molecular) guidance is known to play a key role during retinal development (Erskine and Herrera 2007; Huberman et al. 2008). In particular, it concerns both cells body migration and neurites growth.

In the retina, cells all emerge from the same pool of progenitors, in a stereotypic order. Mechanisms exist to allow cell proliferation at correct proportions and at precise developmental stages. Such mechanisms use either intrinsic factors (internal clock) (Alsio et al. 2013; Saurat et al. 2013; La Torre, Georgi, and Reh 2013) or extrinsic molecular guidance. For the latter, several proteins influencing either the cell birth or the differentiation timing have been identified (X. M. Zhang and Yang 2001; Rodriguez et al. 2012; Kohwi and Doe 2013).

In addition to temporal guidance (cell differentiation), molecular cues could also be implicated in spatial guidance (cellular migration). Such mechanism has been demonstrated in mouse cortex (Tissir and Goffinet 2003), where the Reelin protein plays a key role for cells to reach their proper location at the end of their migration pathway. This molecular cue diffuses through the extracellular space and is captured by two receptors of the lipoprotein receptor family. The Reelin protein could act as a stop signal during cellular migration, allowing cells to laminate in the appropriate stratum (Tissir and Goffinet 2003). As previously stated, progenitor cells and newly born retinal cell types migrate vertically (mono or bi-directional migration, see Figure 3) in order to reach their specific laminar location. Molecular guidance plays a role in cellular migration and final location in the retina as well. Hence, in mouse, the laminin receptor β1-Integrin is mandatory for RGCs to reach their appropriate apico-basal location (Riccomagno et al. 2014). Deletion of this integrin results in cellular misplacement, RGC somata continuing their migration after reaching their supposed lamination level (Edwards et al. 2010; Pinzón-Duarte et al. 2010). Thus, this molecular cue seems to act as a stop signal for RGCs migration.

Furthermore, chemical guidance plays a role in tangential migration in the retina. Indeed, the spacing of SAC and horizontal cell bodies depends on the signal initiated by two trans-membrane proteins, MEGF10 and MEGF11 (Kay, Chu, and Sanes 2012). This molecular cue acts as a repellent for homotypic cells, thus triggering fine tangential repositioning of their somata.

In order to establish functional connectivity, axonal terminals have to target the appropriate postsynaptic targets (dendrites, cell body). As previously mentioned, molecular guidance influences the regulation of dendrite growth in the brain (Valnegri, Puram, and Bonni 2015). More precisely, several families of extrinsic factors have been identified, being either secreted cues or contact-mediated regulators. While the former can influence dendritic morphologies at a distant range, the latter requires physical contact between the dendrite and another cellular element. Secreted cues particularly includes neurotrophins, semaphorins and ephrins (Valnegri, Puram, and Bonni 2015). Neurotrophins are a family of secreted proteins comprising notably neurotrophin-nerve growth factor, brain-derived neurotrophic factor and neurotrophins 3 and 4 (Huang and Reichardt 2003). In rodent cortex, they promote dendritic growth and arborisation (McAllister, Lo, and Katz 1995). Semaphorins are secreted proteins known to control neurite guidance, notably in the olfactory system (Komiyama et al. 2007) and hippocampal CA1 pyramidal neurons

(F. Nakamura et al. 2009). They can act as inhibitory signals, preventing axons from growing in inappropriate regions and establish connections to irrelevant neurons, or as dendritic growth promoter (Shelly et al. 2011). Finally, ephrins can act as guidance for dendritic growth (Clifford et al. 2014) and they are implicated in dendrite pruning mechanisms and synaptic formation (N.-J. Xu et al. 2011).

In the retina, several studies provide evidence that molecular guidance cues regulate appropriate stratification of neurites into the IPL or OPL, via either an attractive or repulsive mechanism. This has been found across vertebrate species (Yamagata and Sanes 2008; Matsuoka et al. 2011). Thus, even if previous studies have shown the role of intrinsic factors in the development of RGC dendritic tree morphologies (Montague and Friedlander 1989; 1991, 1), it is now clear that intrinsic mechanisms alone are not enough to explain how RGC dendrites grow and remodel (Hoon et al. 2014). Specifically, the neurotrophin family regulates RGC dendritic arborisation (Cohen-Cory and Lom 2004). Likewise, trans-membrane semaphorins play a crucial role in controlling the laminar stratification within the IPL (Matsuoka et al. 2011). Thereby, amacrine cell dendrites are believed to give stratification cues to RGCs while they grow and branch, in order for RGC dendrites to laminate at the correct location and establish relevant connections (Kay et al. 2004; Huberman, Clandinin, and Baier 2010; Matsuoka et al. 2011). Interestingly, RGCs provide some lamination cues during development of amacrine cell dendrites as well (Matsuoka et al. 2011). This effect can be repulsive for the dendrites of some amacrine type. In particular, this could explain why some amacrine cells laminate inside the Off IPL sub-layer rather than the On sub-layer. On the contrary, the dendritic tree of other amacrine types are significantly less sensitive to these semaphorins (Matsuoka et al. 2011), thus allowing dendritic stratification closer to RGCs. The vast diversity of amacrine cell types at the molecular level — and thus with different sensitivities to chemical clues — could in part explain the observed diversity of amacrine cells morphologies.

Despite the importance of molecular guidance for dendritic arborisation and lamination, it is important however to remember that not all cells express high sensitivity to these cues, with different neuronal groups adopting different dendritic growth strategies. Hence, while some RGCs seems to target more directly their sub-lamina, other RGCs exhibit preferentially an exploratory behaviour, with extension followed by retraction of misplaced dendrites (Hoon et al. 2014).

1.1.3 Retinal waves

Maturation and refinement of neural networks through activity is a well-established mechanism in cortex (Luhmann et al. 2016). Spontaneous activity in the CNS before sensory input is believed to play a key role in this process. In the developing mouse retina, this spontaneous activity emerges long before eye-opening and is manifested by waves of spikes spreading across the RGC layer (Meister et al. 1991). The link between this early activity and development of visual connectivity has also been previously demonstrated (Huberman et al. 2008; Assali et al. 2014). Retinal waves have also been shown to be implicated in the refinement of retinal projections (Torborg and Feller 2005) and the establishment of retinal receptive fields (Sernagor et al. 2001). The advent of population recording using either imaging or multi-electrode array (MEA) electrophysiology allows the simultaneous recording of a large portion (if not the totality) of the retina, thus facilitating the characterisation of retinal waves, as illustrated in Figure 4 (from (Maccione et al. 2014).

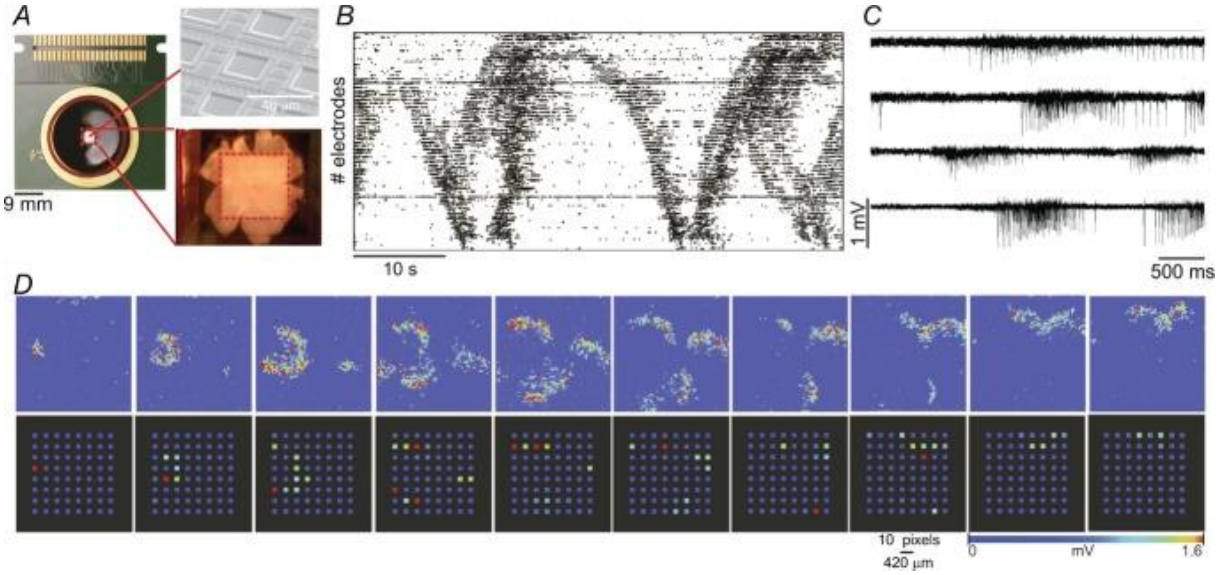

Figure 4: From Maccione et al., 2014, Figure 1: **A**, the Active Pixel Sensor MEA chip. The red dotted line demarcates the active area of the 4096 electrodes on the chip (64x64 configuration, 41 µm electrode pitch). Top inset, scanning electron micrograph illustrating the topography of individual electrodes on the chip. Bottom inset, magnification of the active area of the chip with a retina positioned on the electrodes. **B**, spike raster plot of spontaneous episodes of activity in a P11 retina. **C**, raw signals on four sampled channels from the same recording. **D**, two-dimensional time-lapse (every 1 s for 10 s) view of the activity. The s.d. of the voltage is estimated in 10 ms bins and plotted using an exponential colour coding scheme to emphasize large deviations and effectively threshold small deviations. Bottom row: same episode after downsampling the resolution to a simulated 8 × 8 array with an electrode pitch of 334 µm. (Maccione et al. 2014).

Three distinct stages of waves follow one another, characterised by specific propagation patterns and underlying mechanisms (Maccione et al. 2014). The first one (stage I) is mediated by gap junctions and occurs during late gestation (Catsicas et al. 1998; Syed et al. 2004). Due to the very early retinal developmental stage at which these waves occur, not much is known about stage I retinal waves precise dynamic and characteristics. Stage II waves occur between birth and P9-10, characterised by slow, but very large propagating events. Their initiation points are reported to be random, as well as their trajectories. They are mediated by cholinergic synaptic transmission (Sernagor et al. 2000; Zhou and Zhao 2000; Sernagor et al. 2003), but wave modulation by GABAergic signalling emerges around P5 (Zhang et al. 2006; Hennig et al. 2011). In the first period of stage II waves (P2-5) GABA signalling depolarises RGCs while at later stages, it switches to mature inhibition. At P7, a decrease in wave size is observed, as a result of this shift in GABAergic signalling effect. Stage II activity density (how many RGCs are recruited per unit area within waves) stays low until P6-7, where it substantially increases (Maccione et al. 2014) to reach its highest value when activity shifts to stage III at P10. Stage III waves are mediated by glutamate signalling originating from bipolar cells (Zhou and Zhao 2000; Blankenship et al. 2009). They are characterised by short, fast and repetitive events that tile the entire retina.

Changes in waves dynamic between P2-12 are summarised in Figure 5 (from Maccione et al., 2014).

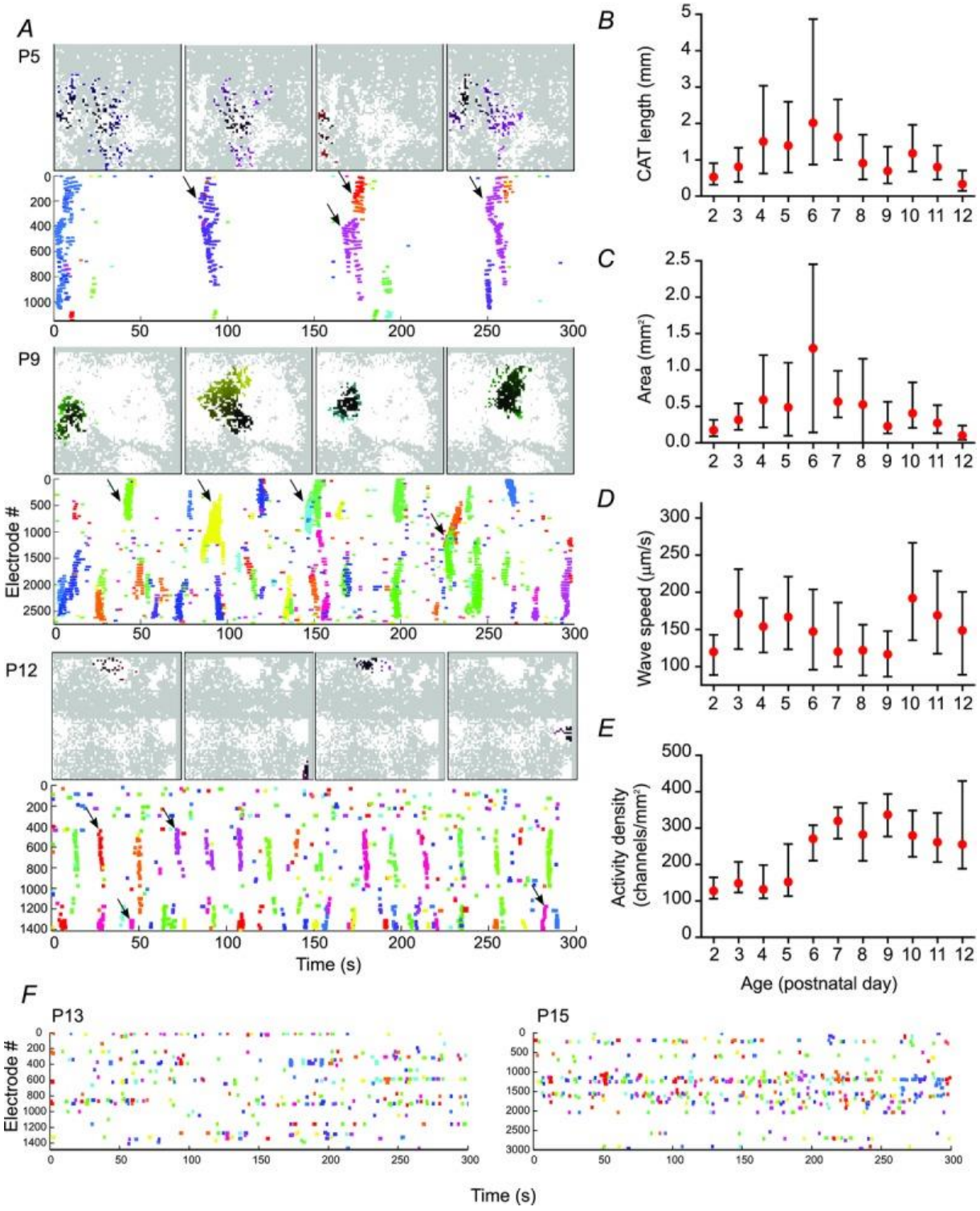

Figure 5: From Maccione et al., 2014, Figure 5: A, examples of waves at postnatal day (P) 5, P9 and P12. Each plot shows a raster of detected bursts, and two-dimensional projections of selected waves, as indicated by arrows. **B–E**, median wave centre of activity trajectory (CAT) length (B), area (C), propagation speed (**D**) and activity density (**E**) for all waves at all developmental stages [postnatal day (P) 2: one retina, 106 waves; P3: two retinas, 191 waves; P4: four retinas, 204 waves; P5: four retinas, 188 waves; P6: five retinas, 99 waves; P7: three retinas, 72 waves; P8: four retinas, 232 waves; P9: eight retinas, 659 waves; P10: seven retinas, 631 waves; P11: six retinas, 945 waves; P12: four retinas, 718 waves]. Error bars

indicate interquartile ranges. F, rasters of burst activity recorded at P13 and P15. No propagating activity can be seen at these ages. (Maccione et al., 2014).

1.2 Computational Modelling of Neural Development

In the past decades, mathematics and computer modelling (referred as computational modelling, or *in-silico*) have been increasingly used, alone or complementary to biological experiments. They consist of representing a particular aspect of the biology in the form of mathematical equations or series of basic functions. They are used in a wide range of fields, including functional modelling (for instance in epilepsy (Wendling et al. 2016)) and anatomical modelling (for instance in tumour growth (Vavourakis et al. 2017; de Montigny et al. 2020) or neural branching structures (Cuntz et al. 2010)). Of course, models that incorporate several simulation aspects (for example anatomical and functional) also exist.

Providing it is biologically inspired and conscientiously and rigorously built, computational modelling can represent a powerful tool. More specifically, it can:

1. Provide a reasoning aid. As biological functions are complex dynamic systems, the consequences derived from a hypothesis influence a large amount of interacting elements. All these consequences are particularly difficult to comprehend, but can be investigated using simulations. Modelling can also allow access to direct measures and quantities where biological experiments can only offer indirect measures or quantities. This allows detection and analysis of interactions, or impact of modifications, within a complex system, that would have not been noticed otherwise.

2. Remove ambiguity from biological theories. Assumptions verbalised through a biological theory can entail some hidden vagueness. Formalisation of a theory can help to remove ambiguity by ensuring that the assumptions it carries are explicit, coherent and consistent. By this way, some biological hypotheses have been proved wrong when they failed to be implemented in a computer modelling (Abbott 2008). In addition, predictions resulting from a computational model are unambiguous and can be reproduced very easily, for verification or further investigation, simply by running the simulation again. Nonetheless, succeeding in modelling a working hypothesis can help to strengthen it.

3. Explain a large system by small simple elements. As previously stated, biological systems are particularly complex and incorporate many interacting elements. Understanding and explaining observed complex functions (for instance cognition or

local neuronal activity) can be difficult. Likewise, explaining the precise implication of smaller elements (like independent neurons) in this function can be arduous. Dividing a single convoluted, hardly resolvable, problem into smaller simpler ones can be of great help to solve it. This is especially well suited for computational modelling where each small element and their interactions can be simulated, while their impact and implication on the whole system is observed. This allows verifying the implication of small elements in the emergence of a higher level function.

4. In some cases, replace or minimise the use of animal experimentation. This point has to be examined in regard to the 3Rs rule for animal experimentation: Replacement, Reduction and Refinement. In addition, and in view of the increasing financial and ethical difficulties of experimental research, modelling can represent an interesting alternative, being usually cheaper and less time-consuming than *in-vivo* or *in-vitro* experiments. Experimental work is still crucial, but computer simulations can be used to verify preliminary assumptions and so, reduce the number of plausible outcomes. They can be used to build promising predictions that can later be tested in an animal or cellular model. In addition, they can be used to identify potential biological features, for instance an electrophysiological property that can be used as an epileptogenesis biomarker (Wendling et al. 2016). In addition, computational modelling presents the advantage of precisely controlling all parameters, which is obviously not possible in experiments. By modifying various parameters, it becomes possible to develop an understanding of the role of these parameters in biological processes. All these points are only possible if the constructed model is especially robust.

Two main branches of biological computational simulation co-exist: continuum-based and agent-based (AB) models. Rather than being antagonist, they are complementary, usually answering different questions.

Continuum-based simulations (one category of mathematical simulations) are the description of a system by mathematical functions and concepts, in which objects are represented in a continuous manner. They can take several forms, including dynamical systems (description of time dependence of a point or flow in a geometrical space) or differential equations (relation between unknown functions and their successive derivatives). In most cases, they describe the dynamic of a system or an object, by representing physical quantities (temperature, volume, voltage, etc.). This approach is well-suited to perform equation-based simulations and is overall

efficient. However, modelling independent cell behaviour is more challenging using continuum-based simulations. Indeed, cellular populations are usually represented by equations as an aggregate rather than individual objects. Likewise, they are less suited to model emergence, a phenomenon in which the properties of a high-level system emerge from the interactions of lower level sub-systems. In addition, being based on continuous equations, this approach usually needs a discretization process before being numerically evaluated. This can be carried out by several methods, being either exact (negligible discretization error), or an approximation (for instance the Euler's method). Exact discretization can sometime be intractable (involvement of integral operations and heavy matrix exponential), and so an approximation of the solution is preferable. Approximation also presents the advantage of being less resource-demanding. Finally, they are usually built with a global supervisor that orchestrates the whole simulation, and that has access to all parameters and variables values. This last point in particular has to be taken into account carefully in order to build biologically realistic simulations.

On the other hand, **Agent Based (AB) simulations** are built on the principle of agents. Agents are tangible and explicitly represented objects in the simulation space. They are characterised by attributes, describing either their anatomy (size, shape, etc.), physical properties (weight, electrical charge, conductivity, etc.) or status. More importantly, their behaviour in response to particulars external or internal stimuli is stipulated. The environment in which these agents exist can also be specified, for instance by its physical properties (extracellular matrix, fluid flow, etc.) or by the presence of chemical substances and their diffusions. These properties can then influence the behaviour of agents, that in turn can influence the environment. Importantly, each agent is independent and autonomous, without any central control with access to all agents. Furthermore, they only have access to local information, either from the environment or from other agents in their vicinity. Simulations are built by placing one or several of these independent objects and simulating their interactions, with the environment and other agents, according to their internally encoded rules. This simulation approach is particularly well suited for the emergence phenomenon, where complex systems emerge by using only simple AB local rules. For this reason, AB approach is especially relevant for modelling cells self-organisation during development, allowing the generation of complex structures, like neural tissues. However, simulating autonomous agents gives rise to considerable demands in computer resources, especially for large scale models where millions of

agents coexist. Contrary to continuum-based approach, AB models also present the characteristic of being discretized by nature. Indeed, simulations are run step by step, with agents and environment characteristics being updated from one step to another.

Of course, the appropriate modelling approach and characteristics depend on the specific scientific question. Thus, the simulation depends on the desired level of analysis and detail. The level of analysis represents the physical scale of the simulation, for instance, simulation at the ion channels level, or at the whole nervous system level. This level of analysis is the main parameter determining the construction of the model. Multi-scale simulations also exist, concerning both physical and temporal scales, where several levels of analysis co-exist. They offer the advantage of incorporating the precise co-influence of mechanisms of different scales, for instance modelling molecular dynamics with precise information of every individual atoms and their co-influences. However, multi-scale simulations generally require an important amount of computation resources to run efficiently. The decision of what mechanism should be included and what mechanism can be neglected is left to the modeller, depending on the relevance of each mechanism with regard to the scientific question. For illustration, it seems irrelevant to model every gas atom in a weather forecasting simulation, modelling air flows at a higher level being more appropriate. For its part, the level of detail determines the precision of a modelled phenomenon, for example if an action potential is described as a square signal or if the precise shape through time of the impulse is modelled. Thereby, the more precise the simulation, the more resources are required to run it. Similar to the level of analysis, the modeller has to decide if a mechanism should be precisely implemented (for example if the precise dynamic of an action potential is important) or simplified (for example if just the presence/absence of an action potential is important).

As building a biological simulation (either continuum-based or AB) requires expertise in both biology and computer science, each model represents an important investment of resources. Computational models are complex programs that need time before being validated and robust enough to build assumptions or verify biological hypotheses. In addition, simulations face an even more problematic limitation, as they are so specialized to answer a scientific problematic, that they usually cannot be used for another scientific question without undergoing heavy re-factoring. For this reason, modelling frameworks start to emerge, proposing a flexible

platform to build simulations. They usually consist in series of generic tools and functions, allowing the modular development of simulations, but also simplifying data manipulations and visualisations. Several frameworks for neural development already exist, providing various functionalities (see Table 1 for an overview of existing modelling frameworks and their characteristics).

	Cell body Dynamic	Neurite Growth	Mechanical Interactions	Agent Based Modelling	Multi-CPU	Electro-Physiology	Open Source
Cx3D	yes	yes	yes	yes	no	no	no
NETMORPH	no	yes	no	no	no	no	no
LAMMPS	yes	no	yes	yes	yes	no	no
CellModeller	yes	no	yes	yes	yes	no	no
iDynoMiCS	yes	no	yes	yes	yes	no	no
Biocellion	yes	no	yes	yes	no	no	no
Chaste	yes	no	yes	yes	yes	yes	no
NeuroMac	no	yes	no	yes	no	no	no
Nengo	no	no	no	no	yes	yes	no
NEST	no	no	no	no	yes	yes	yes
Virtual Brain	no	no	no	no	yes	yes	yes

Table 1: Comparison of current frameworks for biological dynamics simulations.

However, most frameworks are not able to account for cell body dynamics (cell growth, division, migration, etc.), neurite growth and mechanical interactions (objects cannot overlap). The only listed one (Cx3D) is however not able to take full advantage of modern hardware, in particular it is not parallelised and so cannot use multi-core CPU efficiently. In addition, existing parallelised and scalable frameworks (meaning that the more computer resources are added to the system, the more work they can process) are not designed to be user-friendly and thus require advance knowledge in both computer science in general and the considered framework in particular. Another major issue of simulation frameworks is the code availability. Few major frameworks are open-source, thus drastically limiting their possible usage. Hence, novel solutions are required to combine software performance, flexibility, open-source and ease of use. For this reason, the BioDynaMo project has been created by a collaboration between Newcastle University and CERN openlab (Breitwieser et al. 2020), aiming to develop a novel, flexible and powerful simulation framework. The BioDynaMo framework is already available and free for use.

1.3 Aims of Investigation

Despite continual advances in the field of retinal development, many mechanisms are still to be fully understood. Thus, some questions remain unanswered concerning

the emergence of stage II waves, but also concerning cellular organisation. Thus, primary goals here are to:

1. Analyse potential mechanisms underlying cholinergic hyperactivity generating stage II waves.

2. Analyse mechanisms underlying retinal mosaics self-organisation. In particular, the biological requirements and the effect of individual mechanisms generating these cellular patterns will be investigated. In addition, an investigation of the requirements for normal dendritic development will be conducted.

1.4 State of the Art

1.4.1 Stage II retinal waves initiation

As mentioned, different mechanisms mediate the various waves stages: first gap junctions, then cholinergic activity (with GABAergic modulation from P5), and finally glutamate signalling.

Stage II waves are particularly interesting as they have been reported to be a key feature in visual pathway circuit elaboration, both within the retina, and between the retina and its projections to the brain (Mrsic-Flogel 2005; Burbridge et al. 2014; H.-P. Xu et al. 2016). They are believed to be mediated by a network of SACs, the only reported cholinergic cells in the retina, initiating waves that are then propagated to RGCs. Indeed, evidence of acetylcholine release in the vicinity of neighbouring SACs and RGCs have been reported (Zheng, Lee, and Zhou 2004). This neurotransmitter release propagates hyper-excitability across SAC and RGC populations. In addition, SACs make direct homotypic connections at these early developmental stages, facilitating lateral propagation of activity across their network (Zheng, Lee, and Zhou 2006; Ford, Felix, and Feller 2012). Theoretical studies have also been conducted, suggesting that SACs play a fundamental role in wave dynamics (Butts et al. 1999; Hennig et al. 2009; Matzakos-Karvouniari et al. 2019). In particular, they are believed to drive both wave initiation and their propagation pattern. Active SACs have also been reported to impose a refractory period, creating boundaries for activity propagation and controlling wave frequency (Ford et al. 2012). It is important to point out that some studies concluded to the existence of a transient network of directly interconnected SACs that would be responsible for cholinergic bursting activity (Zheng et al. 2006; Ford et al. 2012). Thus, according to this proposed mechanism, the hyper-activity responsible for cholinergic wave initiation would only be present

during the first ten days after birth in mouse, before disappearing with the switch from cholinergic to glutamatergic driven waves (stage III waves).

Despite being the most characterised waves, mechanisms underlying stage II retinal waves generation remain to be fully elucidated. In particular, clear evidence of the precise mechanism responsible for the SACs hyper-excitability and spontaneous depolarisation is not fully understood. Likewise, no clear information exists about the dynamics of wave initiation locations.

1.4.2 RGCs, mosaics formation and dendritic development

Mosaic formation

Retinal mosaics are a key feature of retinal cells' organisation, and are observed within all retinal nuclear layers. Regular spacing between homotypic cells enables homogeneous processing of the light signals, leaving no perceptual holes within our visual field. In particular, sub-groups of RGCs and SACs are known to form regular mosaics and both cell types are widely used to study mosaic organisation. As previously stated, RGCs can be divided into more than 30 types (Sanes and Masland 2015; Reese and Keeley 2015; Baden et al. 2016), each having different functional and anatomical characteristics. At present, a group of RGCs has to fulfil four criteria in order to be considered a RGC type (Sanes and Masland 2015): 1. Morphological homogeneity (dendritic tree shape), as used for the original RGC classification by Cajal using Golgi staining in 1892. 2. Identical physiological properties (electrophysiological response to light). 3. Similar gene expression (molecular signature). 4. To exhibit regular spacing. Thus, being organised in mosaics also represents an important feature of each RGC type. It is important however to point out that recent studies question this last criteria, with evidence of at least three RGC types (W3, Jam-B and Drd4) that do not exhibit regular spacing (Keeley et al., 2020).

Even if the total number of types is estimated to more than forty, only nineteen have been fully characterised (cellular density, morphology, molecular signature and functions) (Sanes and Masland, 2015). These types comprise four On-Off directionally selective RGCs (DSGC), three On DSGC, one On-Off local edge detector (LED), one On Alpha, two Off Alpha, three On Melanopsin (M2, M4 and M5), one Off Melanopsin (M1), one On-Off Melanopsin (M3) and three Off J-RGC (J-RGC, mini-J-RGC and midi-J-RGC).

On-OFF DSGC represents a coherent group, exhibiting similar morphologies between the four groups, with a large dendritic tree stratifying in the On and Off IPL. In addition, an exclusive molecular signature is observed, with the expression of the neuropeptide cocaine and amphetamine regulated transcript (CART) distinguishing them from other RGCs (J. N. Kay et al. 2011). However, physiological differences can be observed between the four On-Off DSGC groups, with strong response to a single preferred direction of motion, upward, downward, backward or forward (Elstrott et al. 2008). Likewise, different molecular signatures characterise each of the four On-Off DSGC groups (Kay et al. 2011). Finally, four distinct mosaics are observed (Devries and Baylor 1997), indicating the existence of four distinct On-Off DSGC groups.

On DSGC groups characteristics are very similar to On-Off DSGCs, with the exception that they stratify only in the On IPL. Thus, they express homogeneity in their dendritic tree shape, but differences in their molecular signatures, physiological responses to light and they form distinct, separate mosaics.

LED RGCs exhibit a narrow (approximately 100 µm) but extensively branched dendritic tree, with the particularity of a large stratification level, from the Off level to the centre of the IPL, despite responding to Off stimulus (van Wyk, Taylor, and Vaney 2006; Russell and Werblin 2010). LED are particularly numerous in retina, representing around 13% of all RGCs in mouse (Y. Zhang et al. 2012). This can be surprising as LEDs respond specifically to one visual feature, which is a small stimulus falling entirely within a single LED receptive field. It has been proposed that this particularity is well suited for the detection of small mammal's predators, such as a bird in the sky (Zhang et al. 2012).

Alpha RGC are characterised by a large dendritic tree and the production of more neurofilament than other RGCs (for this reason, a SMI-32 staining marks these cells particularly well). They also exhibit a specific molecular signature, with the expression of spp1 (encoding the secreted phosphoprotein osteopotin) and kcng4 (encoding a voltage-gated potassium channel subunit) (Duan et al. 2015). However, they can be divided into three groups, one On and two Off, based on the IPL level they laminate in, but also based on their physiological responses to light and specific molecular signatures (Kim et al. 2010; Huberman et al. 2008; Estevez et al. 2012). In addition, they form independent mosaics.

Melanopsin RGCs represent a particular RGC category as they are the only known non photoreceptor (rods, cones) light sensitive cells in the retina. They can be divided into five sub-groups (M1-M5), depending on their physiology, molecular signature, and the independent mosaics they form (Berson et al. 2010; Hu et al. 2013). Their dendritic arbour is known to be large but sparsely branched.

J-RGCs respond exclusively to Off stimuli and are characterised by a notable preference in their dendritic tree direction, resulting in a very strong asymmetry of their dendritic arborisation. They however can be divided into three more coherent groups, J-RGC, mini-J-RGC and midi-J-RGC, depending on their specific molecular signatures, dendritic morphology and the independent mosaics they form. Indeed, despite all exhibiting strongly asymmetric dendritic arbours, mini-J-RGC and midi-J-RGC are characterised by a smaller dendritic tree (Sanes and Masland, 2015).

More RGC types are known to exist, but are incompletely characterised, such as suppressed-by-contrast cells or chromatically sensitive RGCs.

Importantly, advances in single-cell transcriptome sequencing (scRNA-seq) recently brought a new light to neuronal cell-type classification (zeng and Sanes, 2017). This technic represents a new and unique opportunity to precisely describe individual cells and so to classify them based on their expression profiles. It represents a useful tool to better understand already described cell types, but also to discover new types. This is particularly true when the existence of additional types was suspected, but the demonstration of their existence impossible in the absence of specific markers (molecular). Thanks to scRNA-seq, it could be possible to classify every RGC in the retina, and so to obtain a close estimation of the number of RGC types and their corresponding cellular density. It could also benefit mosaic studies, as each type could be independently investigated. More, by performing sequencing in early development, it could be possible to study retinal cellular organisation and development of independent types (or their progenitors) before electrophysiological or molecular markers are available. This could help study mosaic formation but more generally better understand retinal self-organisation.

The existence of such a vast diversity or RGCs gave rise to two different hypotheses to explain it. The first one, proposed by Jerome Lettvin, is the feature detection hypothesis, in which each cell type exists to extract one precise relevant feature (Lettvin et al. 1959). Thus, the more types exist, the more features the retina is able to extract from a visual scene. The second one is the efficient coding hypothesis

(Atick and Redlich 1990; Gollisch and Meister 2010), in which the diversity of RGCs helps to code visual information into an efficient form, minimising the number of spikes needed to transmit a signal to the brain. In this second hypothesis, the variety of RGC type simply helps to reduce the signal processing within the retina, while in the first one, each RGC type exist to detect a specific visual feature.

Despite being an important feature of retinal organisation, retinal mosaics' formation is not fully understood yet. In particular, three mechanisms are believed to potentially take part in their development: cell-fate determination, programmed cell death and tangential migration (Eglen 2006; Reese and Keeley 2015).

Cell-fate determination

Cell-fate determination is a process in which a cell of a certain type will prevent the emergence of same type cells at its vicinity (McCabe, Gunther, and Reh 1999). Emerging from a pool of progenitors, cells are for a time undifferentiated and later choose their type depending on intrinsic and extrinsic factors. More precisely, after passing through an intrinsically determined state, retinal progenitors are still left in an undifferentiated state, but are now only capable of giving rise to a limited subset of cell types. The precise type the cells choose to differentiate into depends on extrinsic signals (Livesey and Cepko 2001). These extrinsic signals, consisting of chemical cues, may be delivered by an already differentiated retinal cell, in order to block neighbouring undifferentiated cells to differentiate into the same cell type. This mechanism has been demonstrated in the retina (Livesey and Cepko 2001) and is believed to be ubiquitous in the developing CNS.

Programmed cell death

RGCs exhibit a very high rate of programmed death, or apoptosis (60-80% of the initial population (Finlay and Pallas 1989)) during normal development. Other cell classes also exhibit programmed cell death, like amacrine cells (Young 1984), but in notably smaller proportions. As creating cells that will rapidly die requires substantial energy consumption, death has to play an important role in order for this energy consumption not to be a waste. Thus, this mechanism is believed to be implicated in the selection of relevant cells in order to build a functional retina. Following this principle, cellular death has been proposed to be a consequence of RGCs not being able to establish correct axonal connection in the lateral geniculate nucleus (Jeffery, 1984). RGC cell death has also been shown to depend on neighbouring cells'

electrical activity (Jeyarasasingam et al. 1998; Eglen and Willshaw 2002). Creating competition between homotypic cells (either spatial or functional competition) could lead to the formation or refinement of mosaics. The importance of programmed cell death upon mosaic formation seems however to vary between cell classes, due to major differences in death rate, but also within a cell class (between types). Thus, the implication of cell death in SACs mosaic formation has been suggested (Hoon et al. 2014), the suppression of this mechanism on the SAC population leading to irregular mosaic patterns. However, this result has not been demonstrated for other amacrine cell types.

Tangential migration

All retinal cells undergo migration during retinal development, both vertical (from one layer to another) and tangential (horizontal migration within the same layer). Cells can move between 20 and 100 µm tangentially from their initial location (B. E. Reese, Harvey, and Tan 1995; B. E. Reese et al. 1999). Furthermore, cellular tangential migration and mosaic regularity are correlated, hence, this mechanism is believed to be implicated in mosaic formation. This has been precisely demonstrated for SACs mosaic formation, where cells move tangentially away from cells of their own type (Galli-Resta et al. 1997). Mechanisms responsible for tangential migration are not fully understood, even if chemical cues seem to play a key role, such as in the case of SACs (Kay, Chu, and Sanes 2012). Thus, diffusible signals or contact-mediated interactions between homotypic cells may be responsible for mosaic formation (Reese and Galli-Resta 2002). It is important to note that mosaics appear, partially or completely, before extensive dendritic growth (Galli-Resta 2002; Nguyen-Ba-Charvet and Chédotal 2014) and thus without contact-mediated interactions. However, other studies point out the importance of dendritic growth upon tangential migration (Galli-Resta 2002; Huckfeldt et al. 2009; Kay, Chu, and Sanes 2012). In all cases, cell-cell interaction seems to be a mandatory mechanism for tangential migration.

Of course, it is likely that the formation of mosaic patterns is due to combinations of those three mechanisms (Nguyen-Ba-Charvet and Chédotal 2014). Previous modelling of mosaic development have been conducted in order to investigate mechanisms responsible for mosaic creation (Eglen and Willshaw 2002; Eglen 2006). These studies were based on simple yet realistic biological rules. They notably participated in showing that a minimal exclusion zone is enough to ensure regular mosaics, and demonstrating that homotypic tangential migration is the most

appropriate mechanism to create this exclusion zone, compared to cell-fate and cell death mechanisms.

Previous mathematical simulations of retinal mosaic formation have been conducted (Eglen and Willshaw 2002; Eglen 2006). These studies investigated the involvement of the CF, CD and CM mechanisms, suggesting a central role for the CM mechanism. However, these studies do not always follow the principle of locally available information, and are limited to a 2D physical space. The later prevents the implementation and investigation of several mechanisms, such as cellular vertical migration (for instance during RGC layer collapse) or realistic dendritic development. No model of mosaic formation in 3D space following the AB principles currently exists.

Dendritic development

In addition to cell body mosaics, RGC dendritic arbours are known to exhibit homotypic self-avoidance (competition for space). While RGCs of dissimilar types exhibit overlap of their dendritic arbours (Gauthier et al. 2009), RGCs of the same type do not overlap, but instead they tile. This phenomenon has been shown for various RGCs (Dacey 1993; Vaney 1994). RGC arbours exhibit dendritic field limited to around half the distance to their homotypic neighbours. In other words, dendritic field sizes are comparable to the voronoi domain areas defined by their homotypic neighbours (Reese and Keeley 2015). This strongly suggests the existence of an interaction mechanism between dendrites of the same type for the establishment of their respective dendritic arbours. This assumption is supported by studies where cellular density is increased, resulting in a reduction of their dendritic arbour size (Kirby and Chalupa 1986). In addition, RGC dendrites have been shown to grow preferentially towards dendrite-depleted regions of the retina (Perry and Linden 1982). This dendritic self-avoidance is believed to be mediated by contact-mediated interactions between homotypic dendritic arbours (Hoon et al. 2014).

Homotypic interactions however are not the only mechanism influencing dendritic development. Indeed, both intrinsic and extrinsic factors play a role in the final arbour shape. For instance, some amacrine cells have intrinsic cues dictating their dendritic morphology, enabling them to laminate correctly even in the absence of RGCs (Günhan-Agar, Kahn, and Chalupa 2000; Kay et al. 2004). On the contrary, and as previously discussed, chemical guidance plays a key role in dendritic development. Thus, amacrine cells provide critical developmental cues for RGCs dendritic

development. Indeed, amacrine cell dendrites have been reported to be targeted by RGC dendrites (Galli-Resta et al. 2008). Along these lines, some RGC types are known to especially target other dendritic arbours, such as the On DSGC dendrites stratifying precisely with On SACs or the On-Off DSGC stratifying with On and Off SACs (Sanes and Masland, 2015). Another illustration of RGCs using amacrine cells' dendrites as a developmental cue is given by Matsuoka et al., 2011. Using a mouse model with non-functional semaphorin (Sema6A) receptors (PlexA4), they showed that the gene deletion responsible for these proteins results in misplaced lamination depth of dopaminergic amacrine cells. More interestingly, they showed that melanopsin RGCs (M1) dendrites still target the misplaced dopaminergic amacrine cells' dendrites, as they usually do in normal development. This demonstrates that amacrine cells can give strong chemical guidance for RGCs dendritic development. However, there is also evidence that some RGCs appear to be less driven by chemical guidance, and target more directly their correct sub-laminae (Hoon et al., 2014).

Previous computational studies have investigated the requirements for realistic neurite growth or morphologies (Nowakowski, Hayes, and Egger 1992; Torben-Nielsen and De Schutter 2014; Kassraian-Fard, Pfeiffer, and Bauer 2020). These studies follow AB rules and yield realistic dendritic development and final cellular morphology. However, the majority of AB computational simulations of dendritic development are focusing on cortical neurons, and few to no AB simulations of RGC dendritic growth has been conducted, raising the need for such simulations. Here, we apply the same AB development principle to simulate RGCs dendritic growth.

In conclusion, the impact and implications of all mechanisms involved in mosaic formation (cell-fate, cell death, tangential migration) and dendritic development (intrinsic, extrinsic factors) are not fully understood, and much remains to be done in order to establish the detailed mechanisms governing mosaic formation and dendritic growth.

In this work we will investigate potential mechanisms underlying hyperactivity generating stage II retinal waves, using a combination of immunocytochemistry and large-scale electrophysiological recordings. We will also investigate mechanisms underlying retinal mosaics formation and dendritic development, using agent-based computational modelling.

Chapter 2. Experimental Investigations: Cellular Populations evolution, Transient Clusters of Cells and Retinal Waves

Waves of spontaneous activity spread across the RGC layer from birth to eye-opening. They are driven by interconnected cholinergic SACs from P0-10 (Stage II waves), followed by waves driven by glutamatergic bipolar cells (Stage III waves) (Maccione et al., 2014). This chapter reports the discovery of a transient population of cellular clusters during Stage II waves, gradually migrating from the optic nerve head to the periphery of the retina. Using a combination of immunocytochemistry and large-scale, high-density multielectrode array recordings from the RGC layer, this study shows that these cellular clusters may be the pacemakers of Stage II waves, and discusses their potential role in guiding retinal angiogenesis.

2.1 Methods

2.1.1 Immunohistochemistry

Retinal sections

To obtain retinal sections, eye cups from postnatal day (P) 3 to P9 mouse pups were fixed for 45 minutes using 4% paraformaldehyde (PFA), incubated in 30% sucrose in 0.1M phosphate buffer solution (PBS) for at least 12 hours, then embedded in Optimal Cutting Temperature (OCT) cryo embedding compound and frozen at -20°C. Eye-cups were sliced as 28µm thick sections using a cryostat (Model : OTF5000, Bright Instruments), washed with PBS to remove OCT, and incubated in blocking solution for 1 hour (5% secondary antibody host species serum with 0.5% Triton X-100 in PBS) prior to staining with antibodies.

Primary antibodies used were: ChAT (AB144P, goat polyclonal, Merck Millipore), VAChT (PA5-77386, rabbit polyclonal, ThermoFisher Scientific) and Caspase 3 (Cleaved Caspase-3 (Asp175), polyclonal rabbit, cat number 9661, cell signaling).

Secondary antibodies used were: Donkey anti rabbit Alexa 568 (A10042, Invitrogen), Donkey anti goat Dylight 488 (SA5-10086, ThermoFisher Scientific).

Two different immunostaining combinations were used:

(1) Primary antibodies' solution: 0.5% Triton X-100 with VAChT (1:500) and ChAT (1:500) in PBS. Secondary antibodies’ solution: 0.5% Triton X-100 with Donkey anti rabbit Alexa 568 (1:500) and donkey anti goat Dylight 488 (1:500) in PBS.

(2) Primary antibodies' solution: 0.5% Triton X-100 with Caspase 3 (1:400) and ChAT (1:500) in PBS. Secondary antibodies' solution: 0.5% Triton X-100 with Donkey anti rabbit Alexa 568 (1:500) and donkey anti goat Dylight 488 (1:500) in PBS.

Retinal sections were incubated with the primary antibodies' solution for 12 hours at 4°C. Sections were washed with PBS, followed by incubation with fluorescent secondary antibodies' solution for 1 hour at room temperature. Finally, slices were washed with PBS and embedded with OptiClear refractive-index homogenisation solution. OptiClear solution consists of 20% w/v N-methylglucamine, 25% w/v 2,2'-Thiodiethanol, 32% w/v Iohexol, pH 7-8. The solution is clear and colourless, with a refractive index of 1.47-1.48. Sections were imaged using the Zeiss LSM 800 confocal microscope. Regions of interests were selected by looking for ChAT expression in order to localise clusters.

Retinal wholemounts

Retinal wholemounts were prepared from mouse pups aged P2-P11, flattened on nitrocellulose membrane filters and fixed for 45 min in 4% PFA. Retinas were then incubated in blocking solution (5% secondary antibody host species serum with 0.5% Triton X-100 in PBS) for 1 hour.

Primary antibodies used were: ChAT (AB144P, goat polyclonal, Merck Millipore), RBPMS (1830-RBPMS, rabbit polyclonal, Phosphosolutions), Sox2 (MAB2018, mouse monoclonal, R&D Systems), Ki67 (polyclonal rabbit, Abcam) and Olig2 (AB9610, rabbit polyclonal, Merck).

Secondary antibodies used were: Donkey anti rabbit Alexa 568 (A10042, Invitrogen), Donkey anti goat Dylight 488 (SA5-10086, ThermoFisher Scientific) and Rabbit anti mouse FITC (315-095-003, Jackson ImmunoResearch).

Three different immunostaining combinations were used:

(1) Primary antibodies' solution: 0.5% Triton X-100 with RNA-binding protein with multiple slicing (RBPMS) (1:500) and ChAT (1:500) in PBS. Secondary antibodies' solution: 0.5% Triton X-100 with donkey anti rabbit Alexa 568 (1:500) and donkey anti goat Dylight 488 (1:500) in PBS.

(2) Primary antibodies' solution: 0.5% Triton X-100 with Ki67 (1:200) and ChAT (1:500) in PBS. Secondary antibodies' solution: 0.5% Triton X-100 with donkey anti rabbit Alexa 568 (1:500) and donkey anti goat Dylight 488 (1:500) in PBS.

(3) Primary antibodies's solution: 0.5% Triton X-100 with Olig2 (1:500) and ChAT (1:500) in PBS. Secondary antibodies' solution: 0.5% Triton X-100 with donkey anti rabbit Alexa 568 (1:500) and donkey anti goat Dylight 488 (1:500) in PBS.

Retinas were incubated with the primary antibody solution for 3 days at 4°C, then washed with PBS and incubated with the secondary antibody solution for 1 day at 4°C. Finally, retinas were washed with PBS and embedded with OptiClear.

Zeiss AxioImager with Apotome processing and the Zeiss LSM 800 confocal microscope were used to image the retinas. High-resolution of the whole retinal surface was achieved by imaging multiple individual adjacent areas. Individual images were subsequently stitched back together to view the entire retinal surface. To compensate for variability in retinal thickness, several focus points were set across the retinal surface in order to keep sharp focus on the desired cell layer. Each individual picture was then acquired at all wavelengths at 20x magnification, and with 10% overlap between neighbouring areas. This overlap is used to correctly align and stitch together all pictures using the Zen Pro software (Zeiss). In addition, three to six mid peripheral regions of interest were selected per retinal wholemount, as illustrated by blue squares in Figure 6. These regions were used to perform RGC and SAC count and cells position extraction.

Z-stacks of images at 40x magnification were also acquired at regions of interest to visualise cells in 3D. Z-stacks consisted of images taken every 1 µm from the RGC layer to below the INL. These regions of interests were selected by using the ChAT staining in order to localise clusters, as illustrated by white squares in Figure 6.

To calculate the relative position of the cell clusters between the optic disc and periphery, lines were traced and measured from the middle of the optic disc to the middle of a cluster (D1) and then from the same point in the cluster to the periphery of the retina (D2). D1/D2 represents the relative position of the clusters. One-way ANOVA was used on all 233 ratio values for all eight groups. Tukey post-hoc test was used to identify significant changes in cluster positions between consecutive developmental days.

Pups aged P2 (N=18 retinas), P3 (N=19), P4 (N=19), P5 (N=19), P6 (N=16), P7 (N=13), P8 (N=10), P9 (N=10), P10 (N=4) and P11 (N=4) were used for immunohistochemistry.

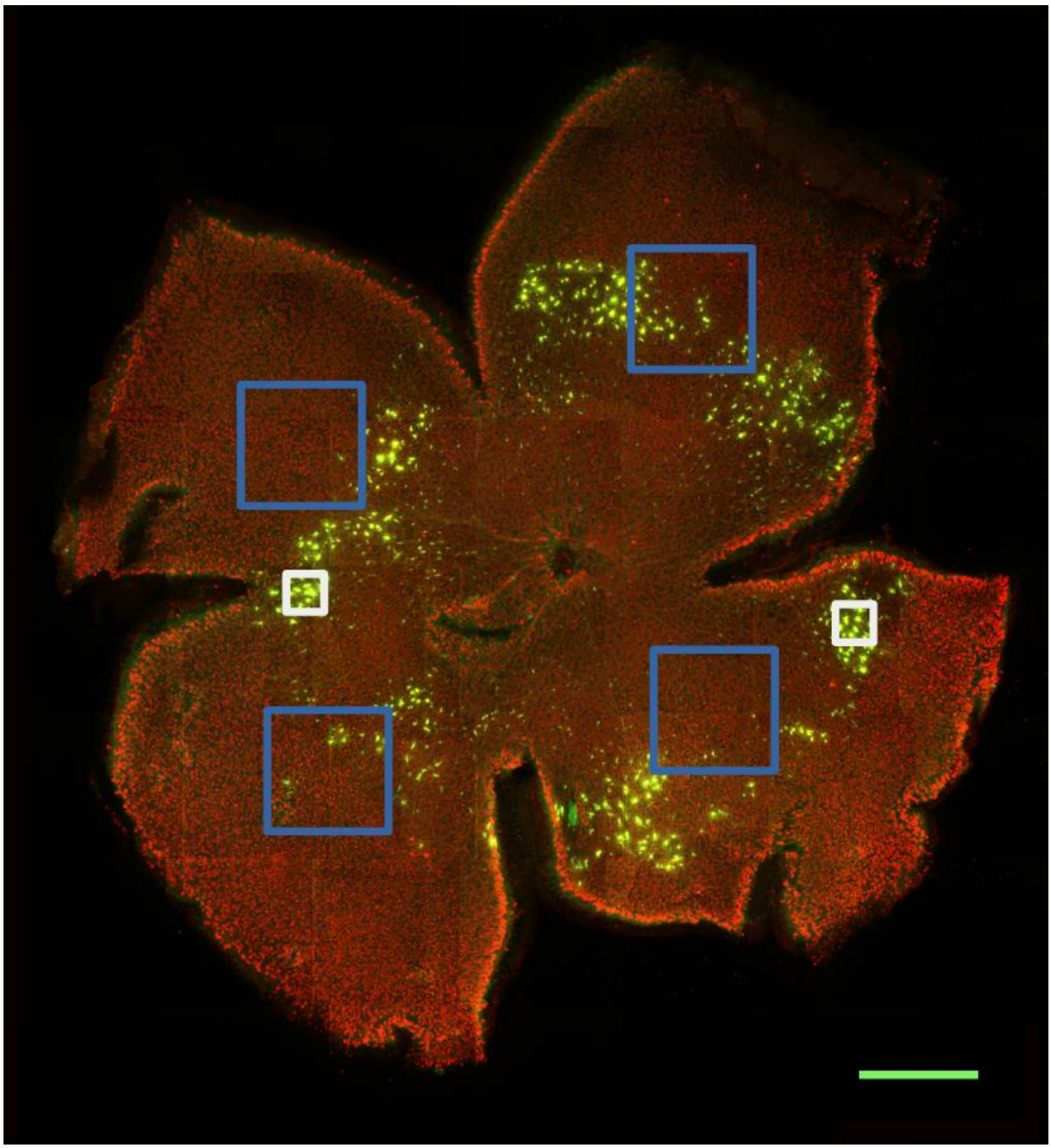

Figure 6: P5 pup retinal wholemount stained with RBPMS (red) and ChAT (green). Blue squares illustrate regions of interest used for RBPMS positive cell count, taken with a 20x magnification. White squares illustrate regions of interest used for clusters and re-imaged at 40x magnification. Scale bar: 500µm.

2.1.2 Electrophysiology

Retinas from mouse pups (P2 (N=4 retinas), P3 (N=4), P4 (N=5), P5 (N=6), P6 (N=3), P7 (N=2), P8 (N=2), P9 (N=2), P10 (N=2), P11 (N=2), P12 (N=1), P13 (N=1) were extracted and flattened, RGC layer facing down onto a Multi Electrode Array (MEA). They were maintained stable by placing a small piece of polyester membrane filter (Sterlitech, Kent, WA, USA) on the retina followed by a home-made anchor. The

retina was kept in constant darkness at 32°C with an in-line heater (Warner Instruments, Hamden, CT, USA) and continuously perfused using a peristaltic pump (~1 ml/min) with artificial cerebrospinal fluid containing the following (in mM): 118 NaCl, 25 $NaHCO_3$, 1 NaH_2PO_4, 3 KCl, 1 $MgCl_2$, 2 $CaCl_2$, and 10 glucose, equilibrated with 95% O_2 and 5% CO_2. Retinas were left to settle for 2 hours before recording, allowing sufficient time for spontaneous activity to reach steady-state levels.

High resolution extracellular recordings of spontaneous waves were performed as described in Maccione et al. (2014). In brief, the BioCam4096 platform with APS MEA chips type HD-MEA Stimulo (3Brain GmbH, Switzerland) were used, providing 4096 square microelectrodes of 21µm x 21µm in size on an active area of 5.12 x 5.12 mm, with an electrode pitch of 81 µm. Raw signals were visualised and recorded at 7 kHz sampling rate with BrainWaveX (3Brain GmbH, Switzerland). Each dataset consisted of 30 minutes of continuous recording of retinal waves.

Retinas were photographed on the MEA at the end of the recording session to ensure we document the precise orientation of the retina with respect to the array of electrodes. Burst and wave detection was done in Matlab (Mathworks) as described in Maccione et al. (2014), using the analysis protocol of Hennig et al. (2009). In brief, bursts were detected by taking into account the inter-spike interval and spike count in a fixed time window, but also using a two threshold criterion based on the mean firing rate on each electrode. The end of a burst was determined as the time of the spike where the spike count first dropped below half of the onset threshold (Hennig et al. 2009). Waves were detected as temporally overlapping groups of bursts. A maximum duration was imposed on burst to avoid the overlap of temporally separated waves (Hennig et al. 2009). The x, y coordinates of wave origins were plotted on the MEA and overlaid with the retina itself in the appropriate orientation with respect to the MEA. The outline of the retina was drawn for each preparation and overlaid with the array of wave origins. An ellipse was drawn to delimit the retina outline while a second concentric ellipse with half the dimension of the outer ellipse was drawn to divide the retina into central and peripheral areas. Wave origins were then classified as either central or peripheral and numbers were used to calculate the periphery/centre ratio of wave origins.

2.2 Results

2.2.1 Immunohistochemistry

RGCs density through development

Using RBPMS staining in P2 to P10 mouse pup retinas, we performed a manual cell count of RGCs on selected retinal areas (see Figure 6 for an illustration). Counting RGCs allows us to deduct the average RGC density for each developmental day (see Figure 7A). The density value of 3537 cells/mm^2 measured at P10, the end point of the developmental period used in this study, is in agreement with the literature, reporting similar RGC density for mid-peripheral retina location (Sanes and Masland 2015a). As expected, an important decrease of RGC density is observed from P2 to P10, diminishing from 6979 cells/mm^2 (standard deviation of ±270) to 3537 cells/mm^2 (±132), corresponding to a decrease of about 49%.

However, this density decrease does not provide a direct measure of CD as the retinal surface itself stretches through development, as shown by Figure 7B. Indeed, pup retinas are far from mature at birth, undergoing progressive and profound anatomical and functional changes from birth until eye-opening around P13 and even beyond. Thereby, the retinal surface significantly expands by about 35% between P2 and P10, increasing from 11.36mm^2 (±0.73) to 15.05mm^2 (±1.75). Such mere surface growth has a significant inherent impact on cell density, independently of programmed CD during the same period. By accounting for this surface expansion, we estimated changes in RGC population through development. More precisely, the estimated total RGC population of a given retina is calculated by multiplying the averaged RGC density (obtained from 3-6 sample areas per retina) by its corresponding retinal surface. These individual measurements are then averaged for each developmental day to give an estimation of the total RGC population from P2 to P10, as shown in Figure 7C. Taking the retinal stretching factor into consideration, it is then possible to calculate the corresponding RGC death more accurately through development, as illustrated in Figure 7D. In detail, the RGC population measured on day D+1 is subtracted from the RGC population measured on day D to measure the amount of CD between day D and D+1. The amount of apoptosis measured between two consecutive days is then averaged to calculate the daily death rate from P3 to P10. CD measurements indicate that the overall RGC population diminishes by 38% between P2 and P10. As RGC death during normal development begins shortly after birth (based on previous studies, notably by Braunger et al., 2014), we can estimate

the total CD rate to be between 60 and 70%. Considering a final death rate of 65%, we can estimate that the population measured at P2 represents only 56% of the initial RGC population. By using this surface corrected CD estimation, we also observe that about 92% of CD is achieved at P5, and 99.5% at P6. It is thus imperative to take retinal surface growth into consideration for these calculations, as measurements that consider only cell density indicate the end of RGC death at P8.

In addition to RGC population size estimation, RBPMS staining also allowed us to measure the relative RGC layer thickness during retinal development, revealing significant thinning from P3 to P9, decreasing from 11.8% (±0.7) to 9.5% (±0.1) of the total thickness of the retina. These results corroborate previous findings, reflecting RGC apoptosis and the collapse of a multi-cellular RGC layer into a mono-cellular layer around P7, once programmed CD is over. In parallel, we measured an average RGC diameter increase from 7.3µm (±0.67) at P3 to 12.4µm at P9 (±0.67), with no significant increase afterwards.

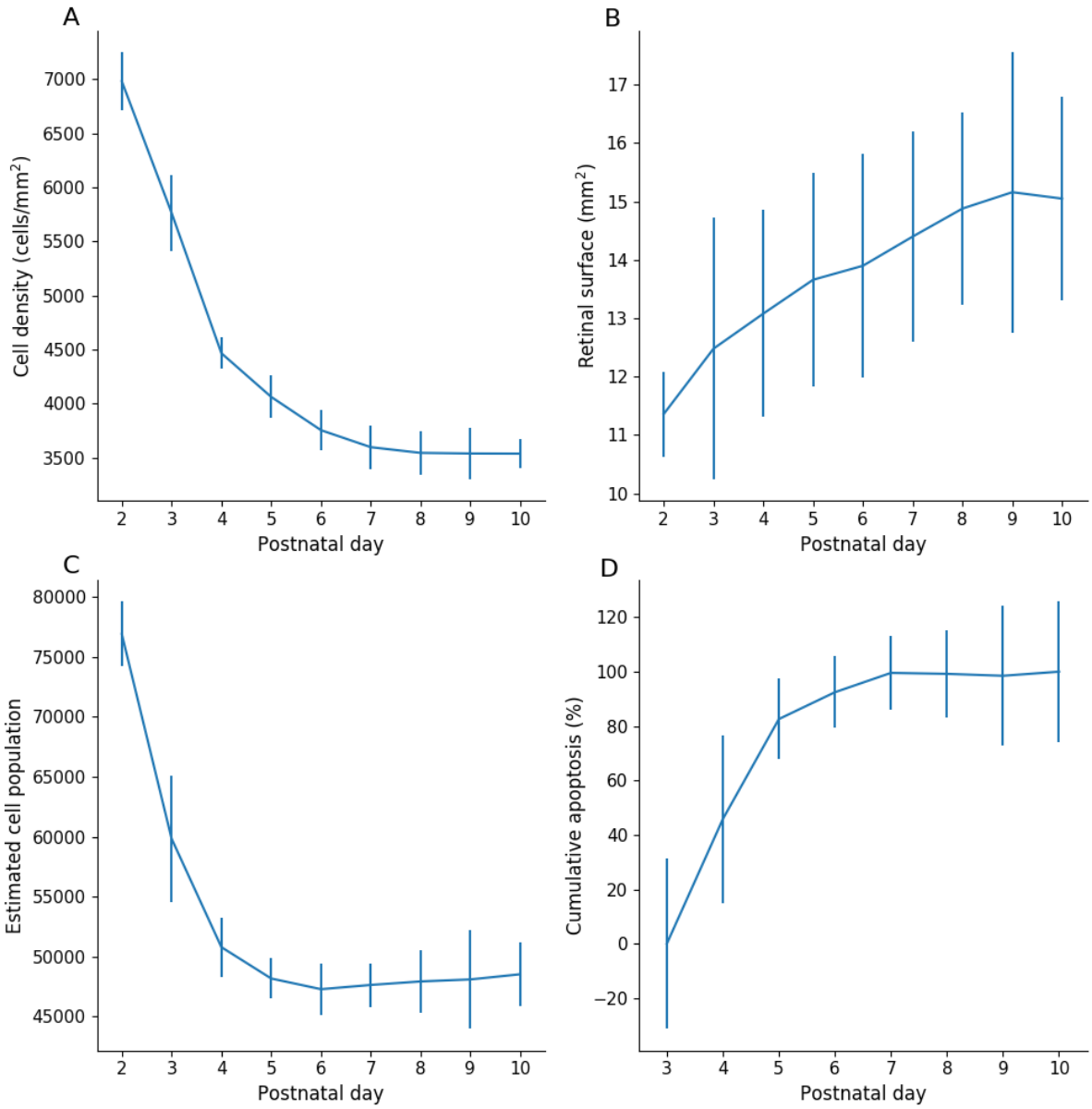

Figure 7: *In-vitro* RGC population characteristics through development. A: Cell density over time. **B:** Retinal surface over time. **C:** Estimated RGC population over time. **D:** cell death over time. Error bars represent the standard deviation. P2: n=16; P3: n=18; P4: n=14; P5: n=15; P6: n=14; P7: n=12; P8: n=10; P9: n=9; P10: n=10 for A, C and D. P2: n=7; P3: n=7; P4: n=8; P5: n=8; P6: n=6; P7: n=6; P8: n=6; P9: n=6; P10: n=5 for B.

RBPMS staining enables to determine the precise position of individual RGCs as well, allowing us to measure changes in RI for the global RGC population throughout development. As shown by Figure 8, RI increases from P2 to P5 ($p = 0.004$ using a T-test for two independent samples, n = 16 and 15 for P2 and P5 respectively), followed by a decrease or plateau between P5 and P6 (no significant differences), and then it rises again until P10. Overall, RI increases from 2.39 (±0.2) at P2 to 4.88 (±0.55) at P10, resulting in more regular RGC organisation at P10 ($p < 0.001$ using a T-test for two independent samples).

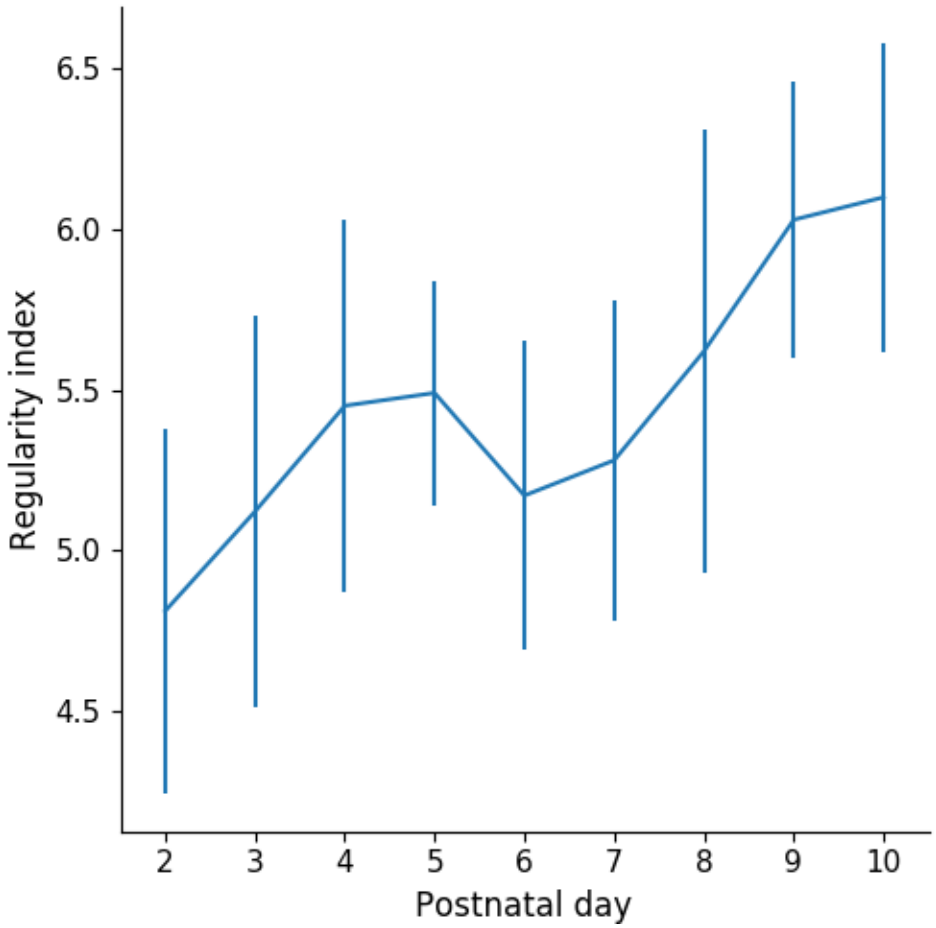

Figure 8: RI measure for the global RGC population from P2 to P10. Error bars represent standard deviation. P2: n=16; P3: n=18; P4: n=14; P5: n=15; P6: n=14; P7: n=12; P8: n=10; P9: n=9; P10: n=10.

SACs characteristics through development

Population analysis has been conducted for another retinal cell type known to exhibit mosaics, the SAC. However, immunocytochemical ChAT expression is not strong enough before P4 to allow a reliable cell counting and position extraction of SAC in the GCL and INL. Therefore, RI and cell density measures have been conducted from P4 to P10. No significant differences are observed in SAC density from P4 to P10, both for the GCL and INL populations ($p=0.27$ and $p=0.32$ respectively with a one way ANOVA test), as shown in Figure 9A. Likewise, no significant differences can be noted in RI score for both GCL and INL populations from P4 to P10, as shown by Figure 9B.

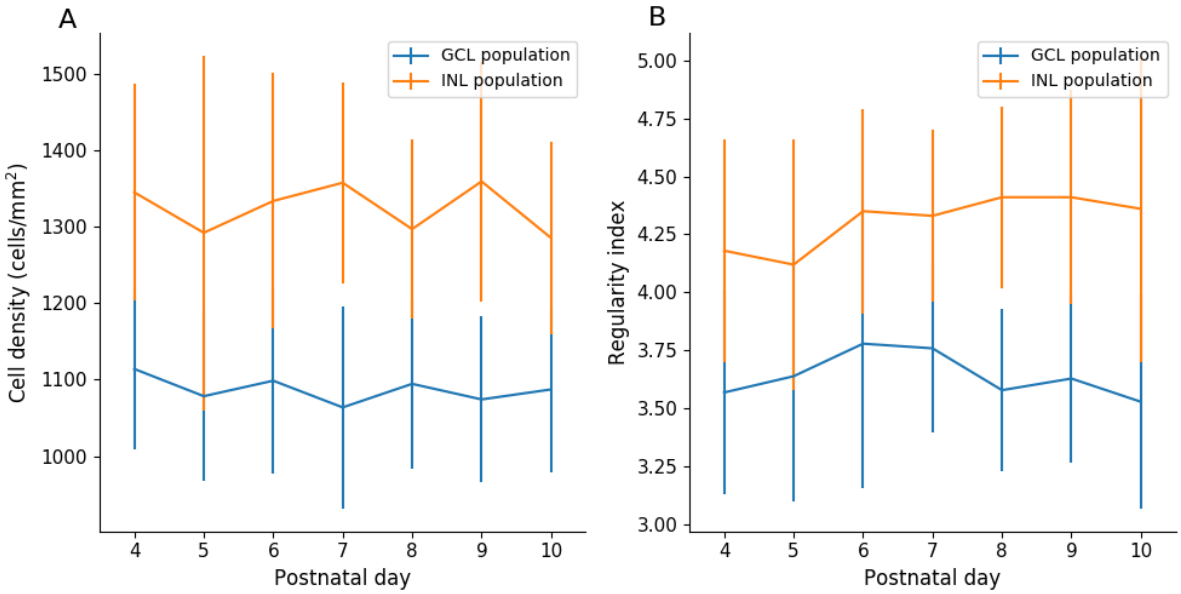

Figure 9: *In-vitro* SAC population characteristics through development. SACs in the CGL population are represented in blue, and the INL population is represented in orange. **A:** Cell density over time. **B:** Regularity index over time. Error bars represent the standard deviation. P4: n=14; P5: n=15; P6: n=14; P7: n=12; P8: n=10; P9: n=9; P10: n=10.

As GCL and INL SAC mosaics are independent, SAC populations in the GCL and the INL only moderately overlap (Rockhill et al., 2000 Kay et al. 2012; Chow et al. 2015). An illustration of SAC mosaics at the INL and GCL levels is shown in Figure 10.

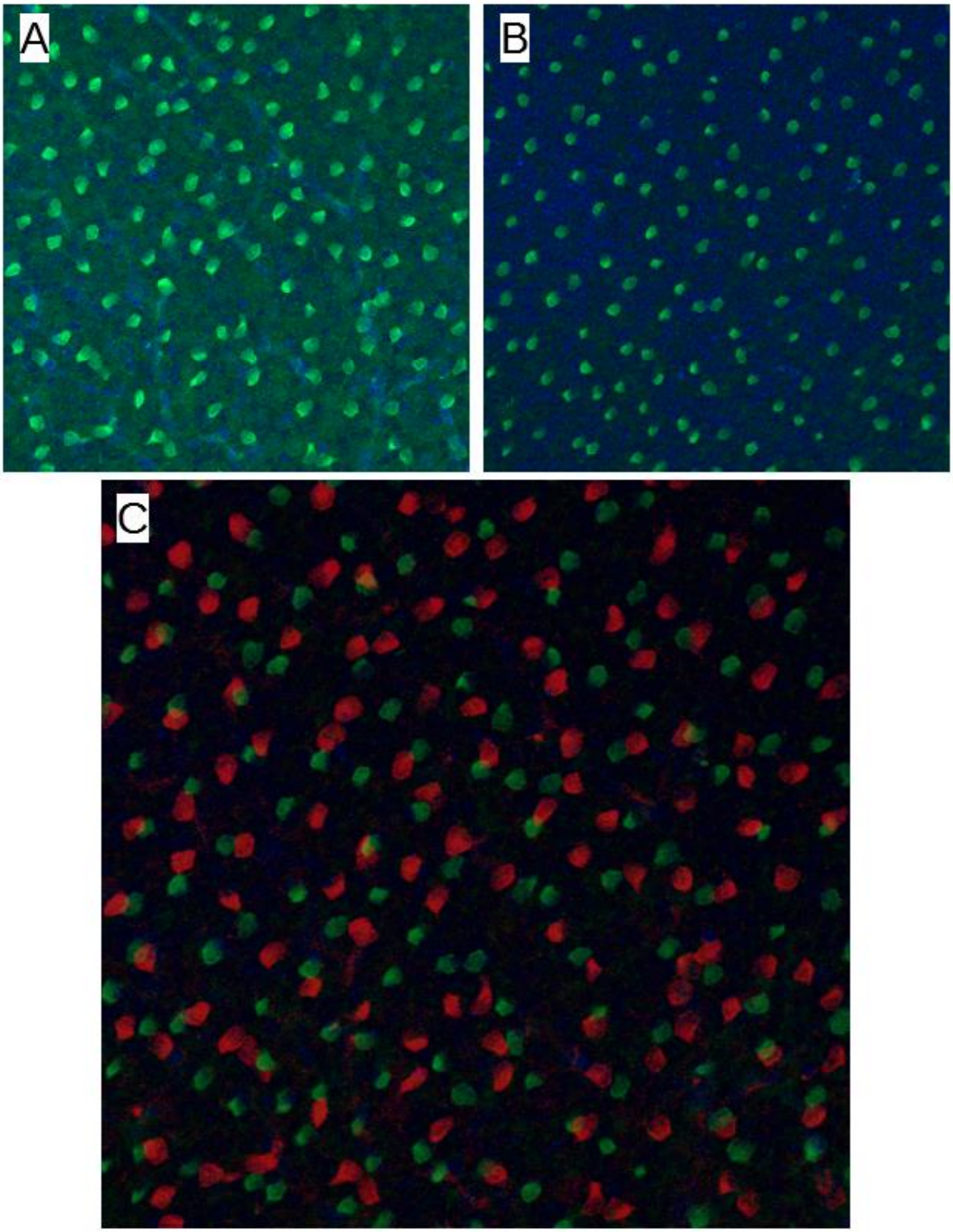

Figure 10: ChAT immunostaining on a P9 pup retina. A: GCL level. **B:** INL level. **C**: overlap of GCL (red) and INL (green) levels. GCL and INL level images are taken at the same x,y position, but at different depth focus. Regular SACs positioning can be observed in each cellular layer. Few cell overlaps between GCL and INL levels are noted.

A measure of populations' exclusion has then been conducted, showing no significant difference from P4 to P10, as shown by Figure 11. The exclusion factor is

based, for two distinct populations, on a count of cells from the first population that are located within a determined distance (exclusion diameter) from cells of the second population. This score is then normalised, to give an exclusion factor between 0 and 1. 1 denotes a perfect exclusion, meaning that all cells of the first population are located at a distance greater than the exclusion diameter from all cells of the second population. By consequence, only exclusion factors calculated with an identical exclusion diameter can be compared. Naturally, if the exclusion diameter is not appropriately chosen (either too large or too small), it is not possible to correctly discern differences between different conditions. For this reason, a unique exclusion diameter of 32µm has been chosen here. This distance allows a good discrimination between our different mosaics.

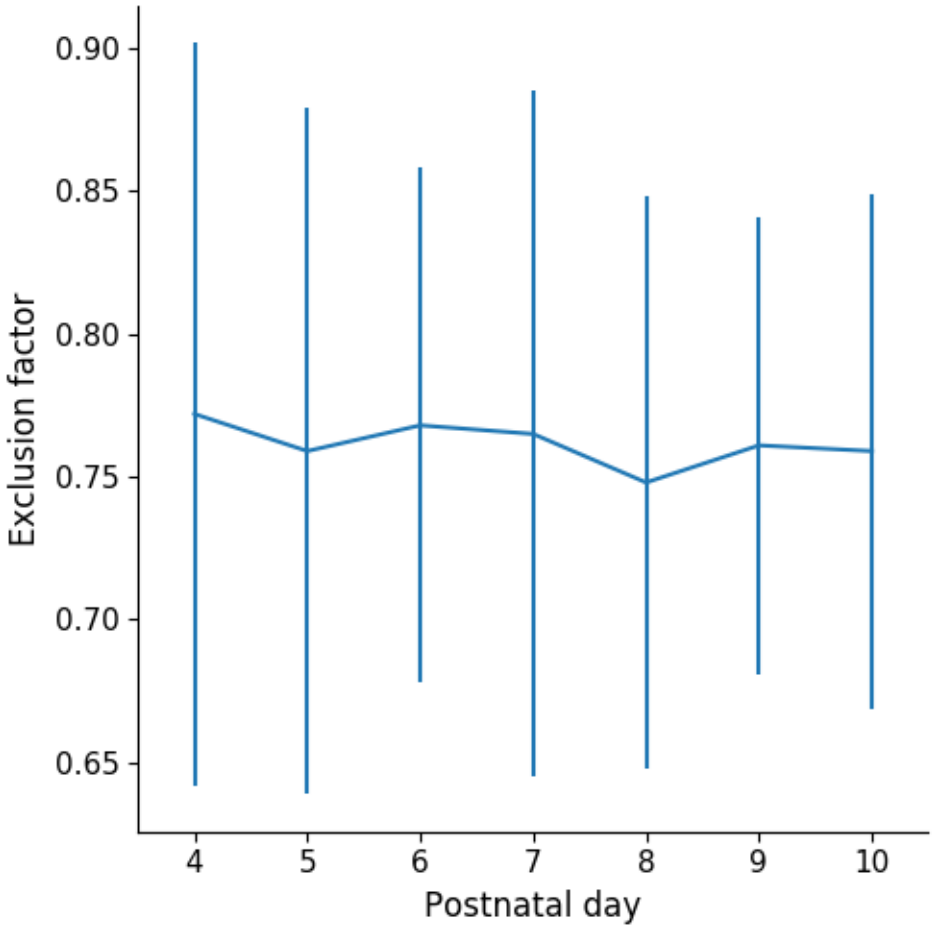

Figure 11 : GCL and INL SAC population exclusion. A score of 1 denotes two mosaics with a perfect exclusion and a score of 0 a total overlap of mosaics. Exclusion diameter of 32µm. Error bars represent standard deviation. P4: n=14; P5: n=15; P6: n=14; P7: n=12; P8: n=10; P9: n=9; P10: n=10. No differences are to be noted between P4 and P10.

Clusters of auto-fluorescent cells

Whole mount imaging of retinas during stage-2 waves (P2-P10) revealed clusters of auto-fluorescent cells in the RGC layer (marked with the RGC-specific RBPMS immunostaining, red in Figure 12). These cells are characterised by a strong auto-fluorescence (green dots in Figure 12), and are not homogeneously distributed across the retinal surface, but are organised as tight clusters forming an annulus at the proximity of the optic disc at P2. This annulus expands during development, reaching the retinal periphery around P6-P7 (see Figure 12), then starts to disintegrate and completely disappears by P10.

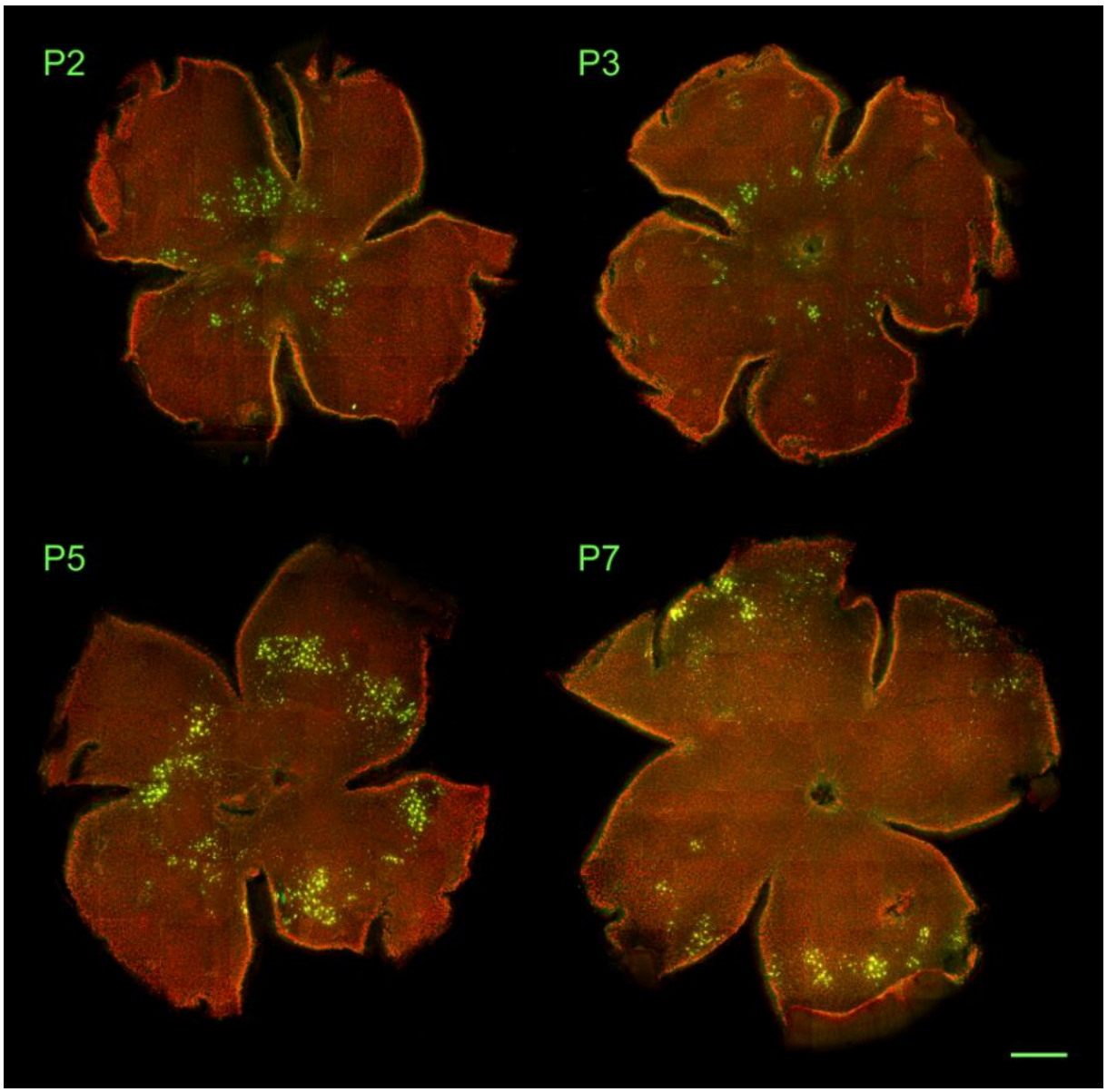

Figure 12: Auto-fluorescent cell clusters expanding from centre to periphery. Mouse retinal whole mounts stained for RBPMS (red) and imaged at the RGC-layer level. Clusters of strongly auto-fluorescent cells appear in green. Scale bar: 500 µm.

Their disappearance coincides with the switch from Stage-2 to Stage-3 waves. A quantification of clusters' relative distance from the optic disk shows that the majority

of the annulus expansion occurs between P3 and P6 (see figure 13A, B), with an expansion of 33.1% between P2-P3, 63.7% between P3-P4, 24.6% between P4-P5 and 25.7% between P5-P6. No significant evolution is observed after P6, with expansion of 3.5%, 4.8% and 6.8% for P6-7, P7-8 and P8-9 respectively. This phenomenon has been observed on all whole mount retinas (n=78 from P2 to P9).

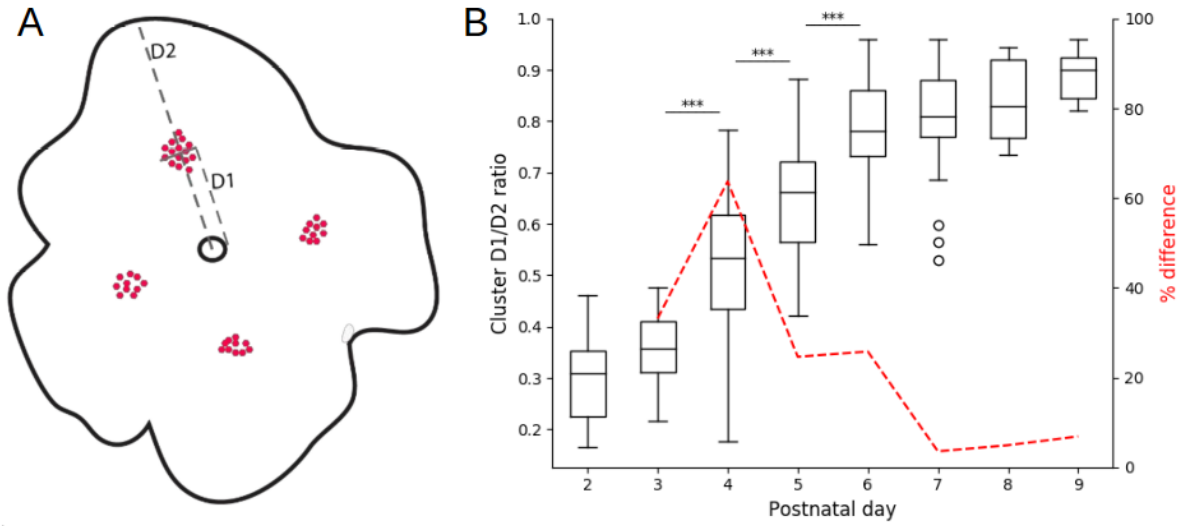

Figure 13: Clusters expansion from centre to periphery during the first postnatal week. A: Method for calculating the relative position of clusters between the optic disc (small black circle in the middle) and periphery. Cluster cells are represented by red dots. D1: distance from centre of optic disc to centre of cluster. D2: distance between centre of cluster to periphery. **B:** Box plot showing developmental changes in D1/D2 ratio. Each box illustrates the median (horizontal line) and interquartile range, with minimum and maximum values (whiskers). Asterisks indicate significant changes between consecutive days (One-way ANOVA with post-hoc Tukey test). The red dashed line illustrates the percentage difference in mean values between consecutive days, showing peak difference between P3 and P4 and no further significant changes from P6 onwards.

Closer inspection of clusters' cells revealed a cell diameter significantly bigger than RGCs (cells diameters of 13.09µm ±1.56 and 9.86µm ±0.53 respectively at P5, n=50 for each group, $p<0.01$ with an unpaired T-test). This difference can be observed in Figure 14 left panel, where some clusters cells are illustrated in white boxes and RGCs are stained in red. In addition, they are exclusively located in the RGC layer, (see Figure 14, left panel), but are absent from the INL, (see Figure 14, right panel).

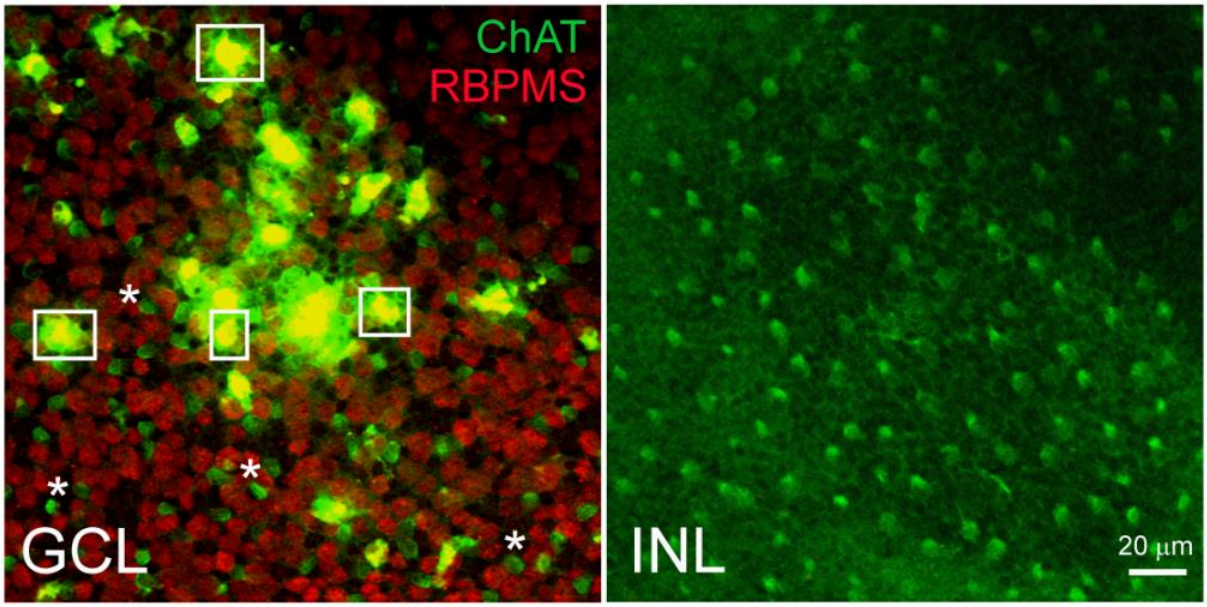

Figure 14: Clusters of auto-fluorescent cells located in the GCL. P5 cluster viewed at the ganglion cell layer (GCL, left) level and at the INL level (right). Red: RBPMS. At the GCL level, auto-fluorescent clusters cells exhibit bright green fluorescence (examples marked within white boxes). SACs are also marked in green (ChAT staining; examples marked with asterisks). At the INL level, there are only SACs.

Vesicular Acetyl Choline Transport (VAChT) expression is also found on the short processes of these clusters, suggesting the presence of cholinergic synaptic terminals (see Figure 15). SACs also express VAChT, in the classical double lamina pattern in IPL, flanked by cell bodies on both sides. VAChT is known to be responsible for acetylcholine transport into presynaptic vesicles, thus being a marker of both cholinergic neurons and neuronal activity. This suggests that these cells have established connectivity with cholinergic cells and are particularly active.

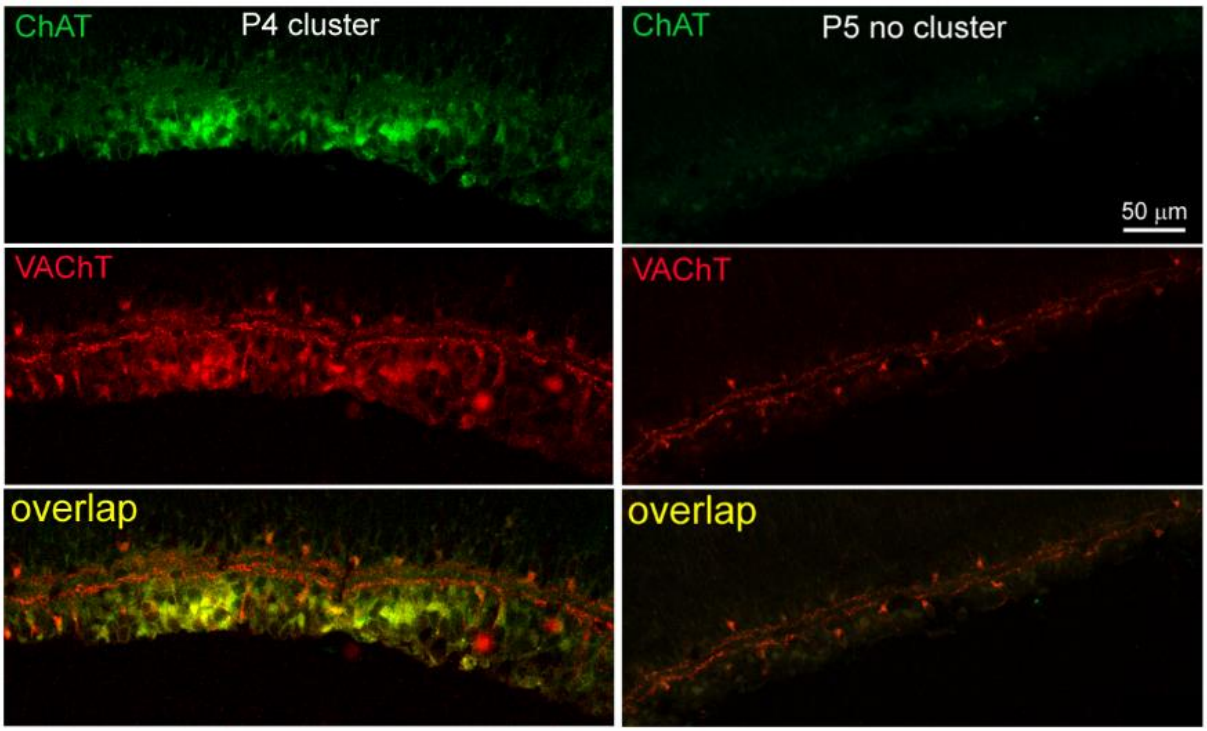

Figure 15: Cluster cells hyperconnectivity identified with VAChT immunolabeling. Retinal sections showing clusters auto-fluorescence (green and red in the left column), ChAT (green) and VAChT (red) expression within a cluster (P4 left column) and in an area without clusters (P5, right column). Cluster cells show strong VAChT expression on their processes, exhibiting a strong double laminar expression in the IPL flanked by cell bodies in the INL and GCL. SACs express VAChT as well, exhibiting the typical double laminar expression in the IPL (ChAT expression is weak in SACs at that age, increasing with development). In areas devoid of clusters, only the SAC expression pattern can be seen.

In order to investigate the clusters' role in the developing retina, Olig2 and ki67 staining has been conducted. Olig2 is a transcription factor expressed in embryonic and postnatal retina, involved in maintaining progenitor cells in an undifferentiated state (Nakamura et al. 2006; Hafler et al. 2012) while ki67 is a proliferation marker in embryonic and postnatal retina (Scholzen and Gerdes 2000). No expression of Olig2 and ki67 by cluster cells is observed. To investigate if clusters cells annulus expansion (P2-P6) and disappearance (P9-P10) are linked to programmed cell death, samples were stained for Caspase3, a hallmark of apoptosis. Likewise, no expression of Caspase3 is observed during clusters' development.

2.2.2 Electrophysiology

As stated previously, auto-fluorescent cells clusters are present only during the period of Stage-2 waves, following a centre to periphery expansion pattern between P2 to P6. Previous studies have shown that Stage II wave sizes increase from P2 to P6 (Maccione et al. 2014). Moreover, clusters disappear at P10, coinciding with the

switch from Stage-2 to Stage-3 waves. These coincidental events suggest that there may be a link between clusters and wave generation. If so, we can predict that wave origins would also follow a centre to periphery pattern from P2 to P6.

To investigate this possibility, we recorded waves from P2 to P13 using a MEA, large enough to span the entire retinal surface (recording surface of 5.12 mm^2). Figure 16A illustrates the electrical activity recording of a P5 retina, and allows us to see the entire retinal surface covered by the MEA (retina outline can be discerned at the boundaries of the MEA chip). A retinal wave can be noted in this figure (top right), corresponding to the arc of high activity (green to red trace). A sample of electrode traces is displayed in Figure 16B. Traces corresponding to electrode recording bursting activity during waves display a high firing rate while other electrodes remain relatively silent.

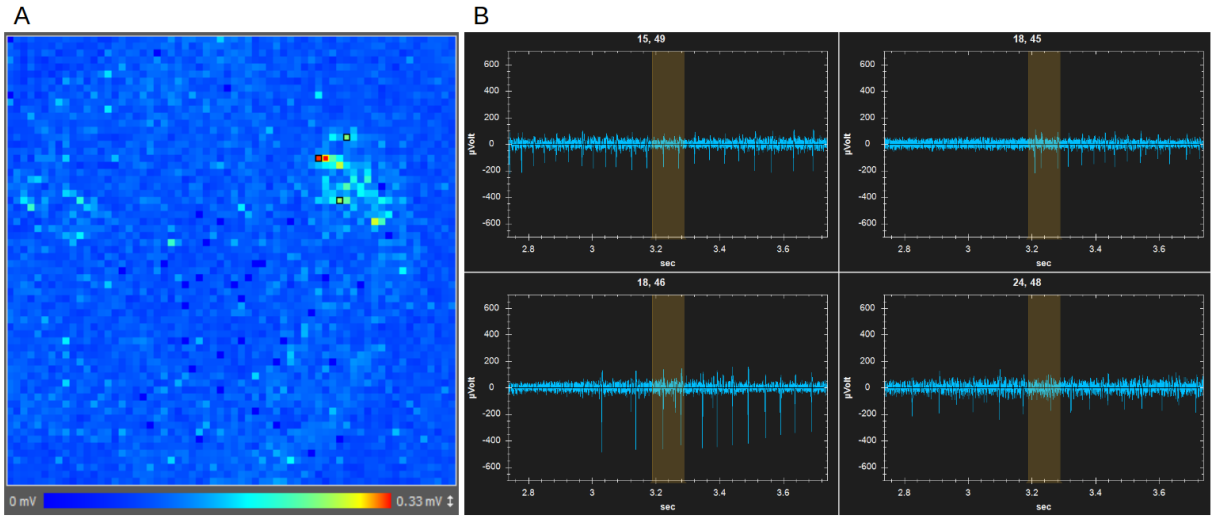

Figure 16: Spontaneous activity recording of a P5 retina. A: Retina activity overview, each pixel corresponds to an electrode. Colours correspond to the voltage ratio, between minimum and maximum voltage, computed over 100 ms. The outline of the retina can be discerned. **B:** Selection of 4 electrodes displaying 1 second of recording. Cells spiking can be noted, corresponding to bursting activity during wave. The four traces correspond to the electrodes delineated with small black squares in A (top right).

Following data processing, wave origins were aligned with the outline of the corresponding retina and used to calculate the periphery/centre ratio of wave origins as described in the Methods and as shown in Figure 17.

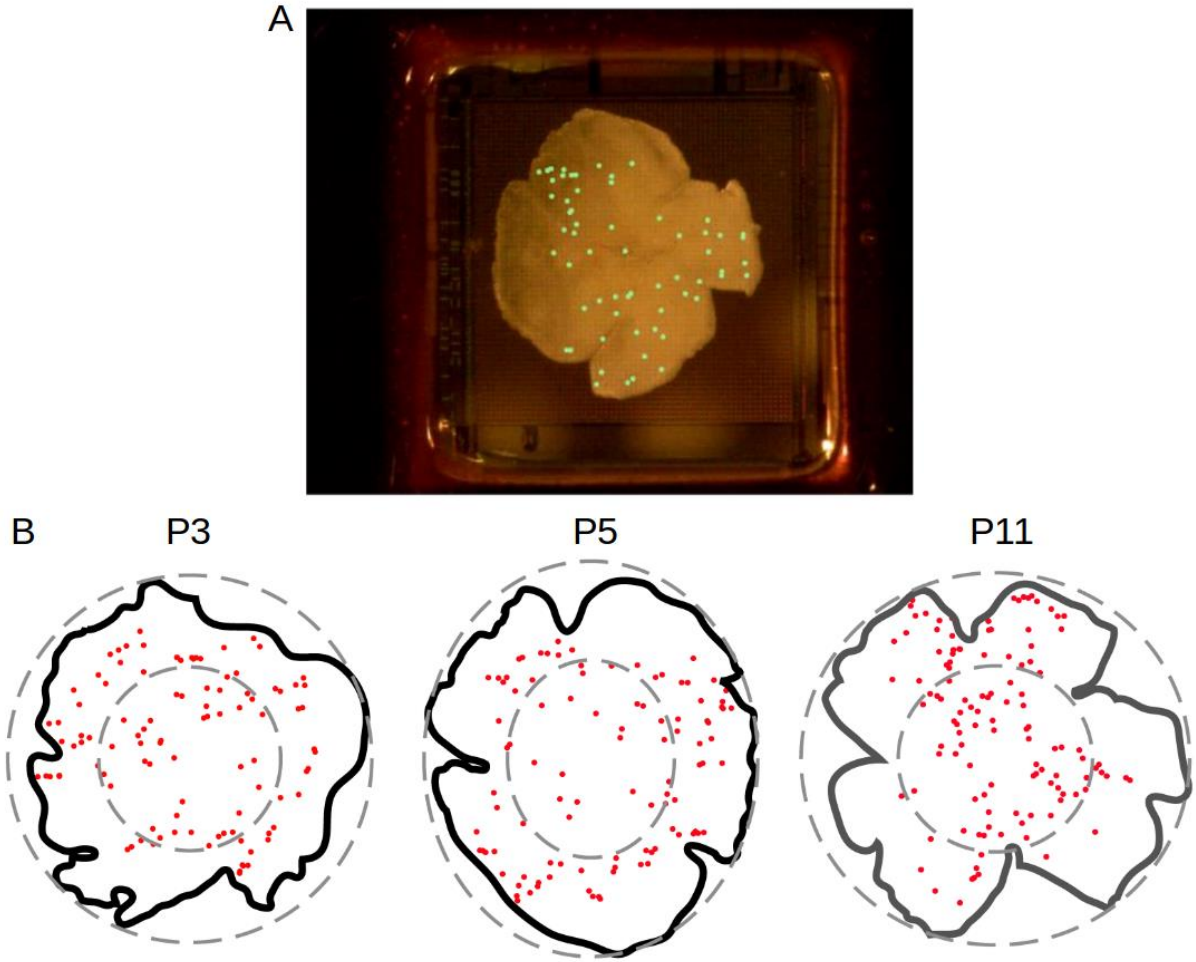

Figure 17: Retinal waves origin periphery/centre ratio quantification. A: Photograph of a P4 retina on the MEA, taken immediately at the end of the recording session. Wave origins (green dots) are overlaid on the photograph. **B:** outlines of retinal whole mounts (black lines) photographed on the MEA immediately after recording and overlaid with waves origins (red dots) detected during 30 minutes recording. Large grey dotted ellipses: encompass the whole retina. The smaller concentric ellipses (50% smaller than the large ones) indicate the central area.

Figure 18 shows changes in periphery/centre ratio of wave origins during development. For each retina, the periphery and centre areas' surface are measured in order to normalise waves origin count of each area by it's corresponding surface. Indeed, as the circle delimiting the centre of the retina has a diameter twice smaller that the circle delimiting the periphery of the retina, this peripheral area exhibits a theoretical surface three time bigger than the central area. Thus, in the case of a random distribution of retinal waves origin across the retinal surface, the peripheral area would contain three time more wave origins than the central area. Thus, after normalizing wave origin counts by their area surface (periphery or centre), a ratio of 1 denotes a random distribution. This wave origin random distribution scenario corresponds to the null hypothesis, and has been added for each developmental day in Figure 18 (red dots). Wave origins expand towards periphery between P2 and P6,

with maximum change between P3 to P5, similarly to the locations of cholinergic clusters. Once clusters disappear and waves switch to Stage III, the periphery-to-center ratio drops below 0.5, corroborating previous finding that glutamatergic waves are small activity hotspots that tile the entire retina (Maccione et al., 2014).

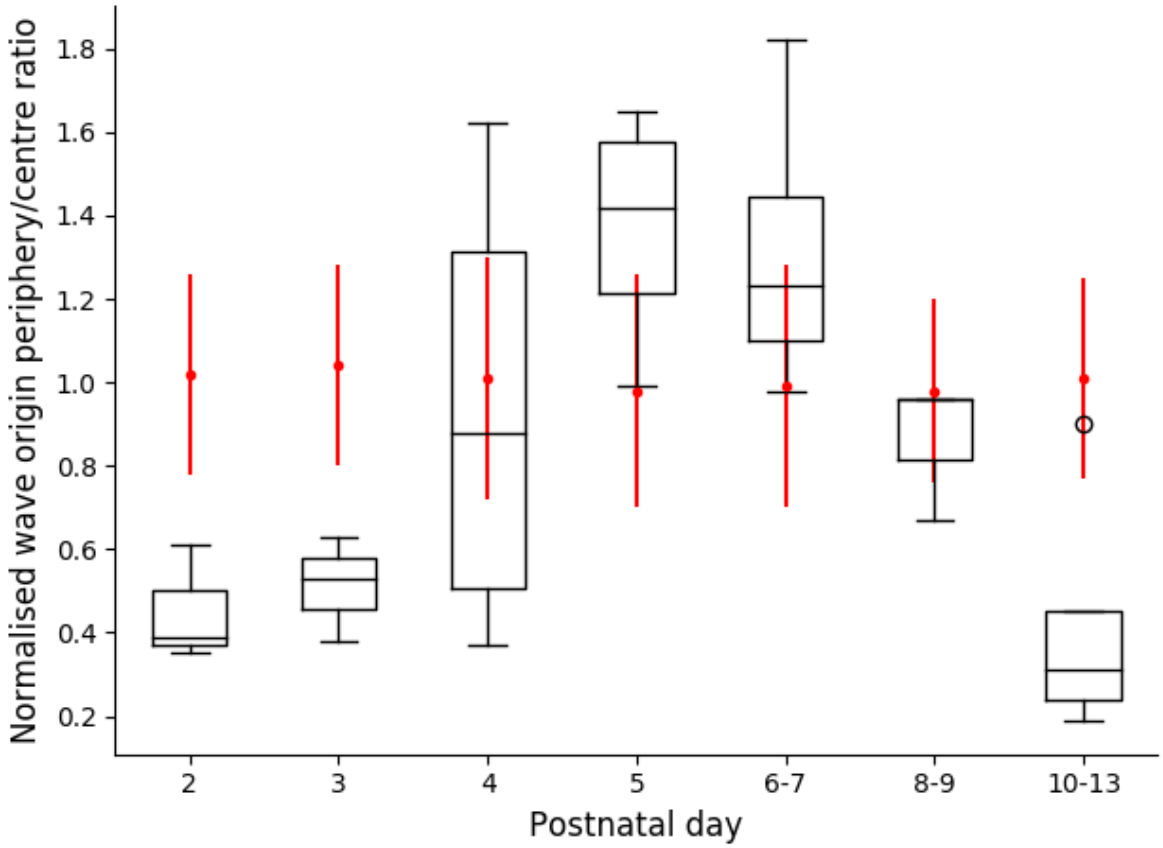

Figure 18: Normalised retinal waves origin ratio expansion toward periphery. Boxplot illustrating the normalised ratio between the numbers of wave origins in the periphery versus those in the central area. Control values, corresponding to a randomised spatial distribution of waves origin for each retina are displayed in red (error bars represent standard deviation). Wave origins expand from centre to periphery between P2 and P5-6, similar to the clusters themselves. Statistical analysis was not possible in this case due to the small numbers of values in each group (one ratio value per retina).

2.3 Discussion

RGCs density through development

Using RBPMS staining, we have been able to investigate the evolution of the RGC population during retinal development. By estimating the RGC population during development using a cell count, we have been able to investigate RGC death rate. Our measures are in agreement with the literature, reporting a total RGC population decrease from around 76,000 cells to around 48,000 cells. This cell population

decrease corresponds to a death rate of about 65% of the initial population, with 99.5% of this cellular death being achieved by P6. Importantly, we showed that it is imperative to take retinal surface growth into account for cellular death rate calculation. Indeed, if the RGC population is estimated through a cell density measure without taking retinal surface stretching into consideration, the corresponding death rate is calculated at the higher value of around 75%, with the end of cellular death at P8. The estimation of RGC population during retinal development could also have been conducted by counting the number of axons in the optic nerve (Jeon et al., 1998). Indeed, as RGCs are the only retinal cell type to establish connections to the brain, and as each RGC projects only one axon, counting the number of axons in the optic nerve provides a direct measure of the number of RGCs in the retina. This method has the advantage of providing a direct and precise measure of the number of RGCs, instead of an approximation of the population. However, due to the early developmental stage of these retinas and the resulting fragility of their optic nerve, such a measure would have been particularly difficult to conduct, and the resulting cell count would have been unreliable.

RBPMS staining also allowed us to precisely extract the position of each RGC and thus to calculate the RI evolution of the whole RGC population during retinal development. We found a global increase from P3 to P10, with a decrease or plateau between P5 and P6 (see Figure 8). It is important to note that no mosaic formation at the whole RGC population level has been reported (Sanes and Masland 2015a), mosaics concerning only sub-populations of homotypic RGCs (On-Off DSGC, Melanopsin M1, sustained On αRGC, etc.). However, as pointed out by Reese and Keeley (2015), regularity measures are strongly linked to cell density in a minimal-distance spacing rule case, such as in the vertebrate retina. To further investigate this relationship between regularity and density, we used simple simulations of the RI measure with a minimal-distance spacing rule in various conditions of initial cell density and layer organisation. These simulations demonstrate that in a mono-layer configuration, the regularity is directly dependent on cell density. In other words, the denser cells are, the higher the RI score. Indeed, at a cellular density of 3000 cells/mm^2, the RI score is 5.18 (±0.11), which is considered very regular. Of course, the cell diameters (or in other words the minimal-distance spacing value) has a significant impact on the regularity as well. For a fixed density, increasing the minimal-distance spacing results in cells being more densely packed, thereby increasing the measured regularity. The effect of the minimal-distance spacing and

the cell density upon RI diminish for independent cell types as the number of cell types composing the total cell population increases. More precisely, RI values measured for each cell type composing the cell population are below what is considered a regular mosaic RI value, if the population is composed of more than five cell types. By consequence, a RI of 2.3 (±0.09) has been measured for a total cell population density of 7000 cells/mm^2 and composed of six cell types. In a bi-layer configuration, the cell density impact on regularity measures is less significant, never reaching a RI value above 3.3, regardless of the cell density or the number of cell types. When a bilayer collapses into a single layer without CD, RI values gradually increase due to the cell density increase induced by the layer collapse. However, as this layer collapse is the result of a cell density reduction, this simplistic scenario does not reproduce RGC organisation evolution. So, if CD is added we note that RI initially increases, corresponding to the density effect described above (minimal-distance spacing), then subsequently decreases, corresponding to the effect of CD. As the involvement of CD in mosaic formation only concerns independent cell types, CD would appear as a random mechanism at the global population level. Thus, the death mechanism implemented in this preliminary simulation is random as well, and set at 65% of the initial population. This phenomenon could explain the RI decrease measured at the global RGC population level. As cell growth continues after the completion of CD, the observed RI increase in the global RGC population from P7 to P10 could be explained by the increase in cell diameter, which mechanically augments the minimal-distance spacing value, thus increasing the regularity.

SACs characteristics through development

In addition to RGCs, *in-vitro* experiments allowed us to investigate another retinal cell type known to exhibit regular spacing, the SAC population. This cell population has the particularity of being divided into the GCL and the INL. Each SAC layer forms a mosaic, and both mosaics are reported to be independent (Rockhill et al., 2000 Kay et al. 2012; Chow et al. 2015). By using ChAT staining, we have been able to measure the cell density for both the GCL and INL population. These cell densities do not vary between P3-4 (shortly after GCL and INL separation) and the end of retinal development (see Figure 9A), indicating an absence of cell death during this period. This ChAT staining also allowed us to measure mosaic regularity of GCL and INL SACs populations during development. Interestingly, no RI variation was observed from P3-4 (see Figure 9B), indicating that these two SACs populations have already created their mosaics by P3-4, hence shortly after SACs migration into

their respective cellular layer. This is notably different from RGCs, which express small tangential migration later on, a phenomenon believed to relate to mosaic refinement. In addition, we also observed that the calculated exclusion factor does not vary. This factor measures how GCL and INL mosaics exclude, or complement, each other, without vertical overlapping of their cell's positions. This also supports the assumption of early SACs mosaics establishment. Moreover, the few observed overlap of GCL and INL mosaics may indicates an absence of interactions between these two SAC populations during their cellular organisation, before they migrate to their respective layer. However, investigating this hypothesis *in-vitro* or *in-vivo* is particularly complex as SACs do not express ChAT strongly before P4. Moreover, no specific molecular signature - that could be used to determine in advance what cellular layer each cell will migrate to - have been reported between their GCL and INL populations. Thus, other experiments, using different techniques, are required in order to investigate further mosaic creation in the GCL and INL SAC populations.

Clusters of auto-fluorescent cells

In this chapter we reported for the first time a transient population of auto-fluorescent cells, present only during the Stage-2 waves period. They appear near the optic disk at P2 and migrate to the periphery by P7, before disappearing at P10, coinciding with the switch to Stage-3 waves. The precise nature of these cells remains however unknown and will require single cell gene sequencing in future studies to determine their genetic identity.

Our experimental observations suggest that these tight cellular clusters may generate strong neural activity during the period of Stage-2 waves. The strong VAChT staining observed at the cells' vicinity could also suggests high activity, as this protein is known to be directly linked to cholinergic activity, transporting acetylcholine from the cytoplasm to the synaptic vesicles (Oda, 1999). Thus, this strong VAChT expression could suggests strong connectivity between the cluster cells and cholinergic retinal neurons, as the presence of VAChT indicates synaptic terminals. Such strong connectivity and hyperactivity could suggest the presence of hyper-excitable hubs of cells capable of triggering activity in neighbouring SACs and RGCs. The auto-fluorescence of these clusters cells could be caused by an accumulation of mitochondrial Nicotinamide Adenine Dinucleotide reduced (NADH), which exhibits strong fluorescence at high concentration (Blinova et al., 2005).

Interestingly, this high concentration of mitochondrial NADH could denote hyperactivity in these auto-fluorescent cells.

Moreover, wave origin location dynamics support the hypothesis that these hyperactive clusters could be responsible for stage II retinal waves initiation. Indeed, wave origins follow a similar pattern of spatial and temporal dynamics across development, establishing a link between clusters and waves initiation locations.

Additional analysis has also been conducted by F. Rozenblit, from the Gollisch lab in the University Medical Center Göttingen, using electrical imaging from MEA recordings (Litke et al. 2004; Petrusca et al. 2007; Zeck, Lambacher, and Fromherz 2011; Greschner et al. 2016). This technique has been used to visualise wave-related electrical activity using either the MEA used for pan-retinal recording, or a high resolution MEA composed of square microelectrodes of 21µm x 21µm in size on an active area of 2.67 x 2.67 mm, with an electrode pitch of 42 µm. The second MEA is significantly more precise than the first one, with double electrode density. Moreover, activity was recorded with a newer system, at much higher sampling rate (17.855 kHz), which yields much better temporal resolution for the responses. Electrical imaging analysis is conducted independently for each electrode by first averaging the electrical activity over all electrodes surrounding the time of spikes in that electrode (spike-triggered average, STA). Then, for each active electrode, a window of -5 to +5 ms of raw MEA signal around wave-related detected spike is selected. By averaging the obtained recording snippets, it is then possible to visualise electrical activity in the spatiotemporal vicinity of spikes.

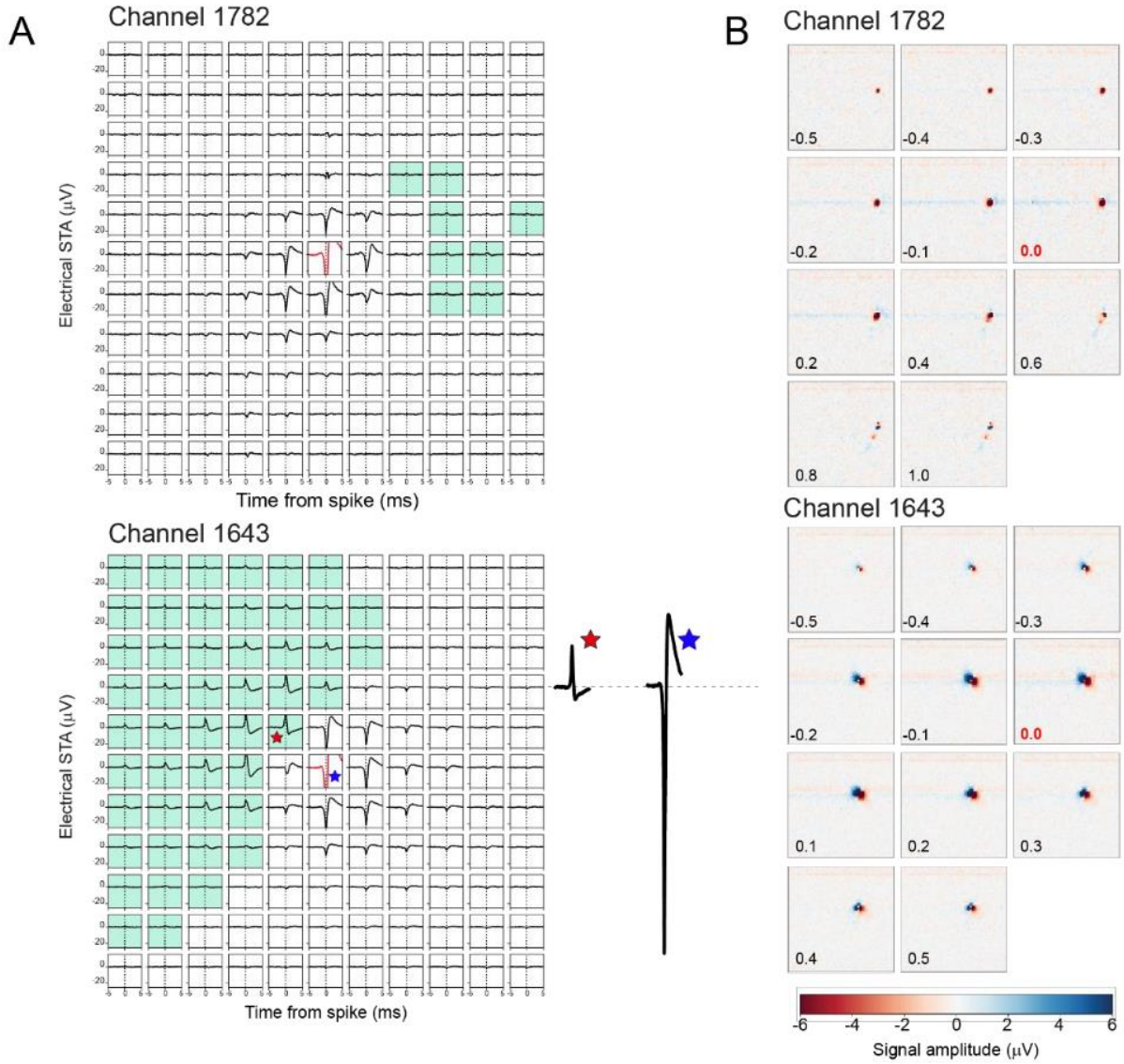

Figure 19: Electrical imaging of retinal waves. A: STAs for two trigger channels showing signals averaged over -5 to +5 ms relative to spikes on the trigger channel (in red) for 11x11 surrounding recording channels. Recording channels with dipole activity (with maximal positive deflections with z score>5 occurring before the maximal negative deflection) are marked with the green mask. Channel 1643 has a marked area with dipole signals near the trigger channel. The single traces on the right side of the electrode grid show the full size of the spike on the trigger channel (blue asterisk) and maximal positive deflection (red asterisk), emphasizing the fact that the amplitude of the dipole signals is significantly smaller than spikes, suggesting that they may represent slow, graded potentials. (P4 retina, 60 min recording). **B:** Time-lapse images taken from movies of the averaged activity for both channels illustrated in A. The precise time of each image is indicated in the bottom left corner of each frame (in ms). Time 0.0 (time of the spikes used for STA) is indicated in red. For Channel 1643, clear dipole signals are seen from the earliest time frame (-0.5ms). Such signals are absent in Channel 1782.

In some cases, a dipole activity was observed where positive deflections emerged simultaneously with the expected negative deflections of a spike, followed by a negative deflection. Although negative deflections smaller than the spike used for

spike-triggered averaging (STA) were detected around most STA channels, presumably reflecting wave-related activity propagation (as in Channel 1782, Figure 19A and 19B), on some channels there are conspicuous positive signals emerging simultaneously with the negative spike signal (Channel 1643, Figure 19A). These signals were significantly smaller (red asterisk) than the STA spikes (blue asterisk), but easily distinct from baseline activity.

Overall, when combining the activity footprint from all channels exhibiting such positive-negative “dipole” behaviour (Figure 20), these areas form clusters in proximity with wave origins (green dots in Figure 20). However, when plotting all maximal projections, regardless of whether they have a positive deflection or not (Figure 20, bottom row), the activity is more spread out over MEA channels, with less clear co-localization with the wave origins. The clustered layout of the dipole areas suggests that these signals may reflect activity originating from the cholinergic cell clusters.

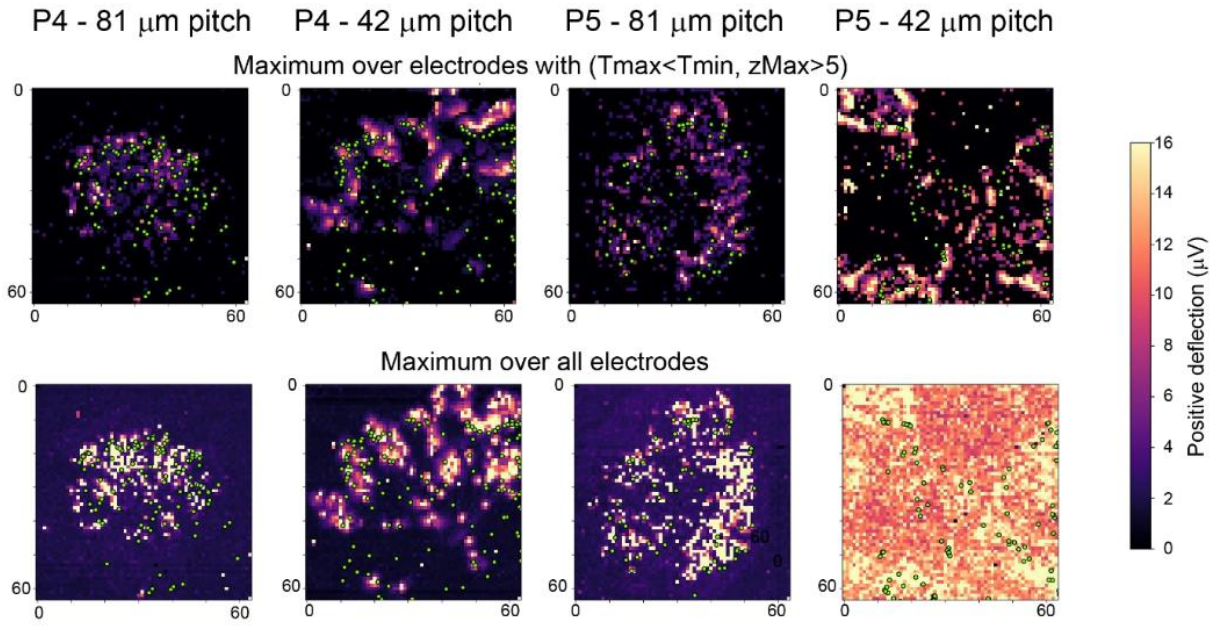

Figure 20: Recomposed electrical imaging of retinal waves. Maximal projections for signals with pre-STA spike signals with larger positive than negative deflections (top row) and for all maximal projections (bottom row) over the entire MEA. Maps are shown for two P4 and two P5 retinas, each with one example recorded on an array with 42 µm electrode pitch, and for another array with 81 µm pitch. Wave origins (green dots) are overlaid on the electrical signals

In summary, electrical imaging analysis reveals the presence of activity clusters characterized by simultaneous positive and negative small signals in proximity with wave origins, suggesting that these clusters may represent activity related to the cluster cells.

In addition to auto-fluorescent clusters electrical activity, we investigated their potential implication in retinal cellular proliferation. The absence of Olig2 signature suggests that these cells clusters are not undifferentiated progenitors' cells. Indeed, Olig2 is a transcription factor whose expression is observed only during early development and is known to be implicated in cellular differentiation and replication sustainment. Likewise, the absence of ki67 signature, known to be a cellular marker for proliferation (Scholzen and Gerdes, 2000), confirms that the clusters are not implicated in cellular proliferation.

One characteristic of the described population is its spatial evolution during development, with a displacement from the centre to the periphery in a brief period, from P2 to P7-8. However, this annulus “migration” cannot be explained by cellular displacement. The corresponding distance to travel and its associated cellular migration velocity would be too important. It would indeed imply a cellular displacement of about 1500µm in five days, corresponding to an average cellular migration speed of about 300µm per day during five days, far above the maximal 30µm tangential migration observed for both SACs and RGCs (Nguyen-Ba-Charvet and Chédotal, 2014).

As spatial migration cannot reasonably explain the centrifugal movement of the clusters, we looked into other potential mechanisms. One potential mechanism might be cellular death of more internal cells, and emergence of new more superficial cells. However, no caspase3 expression was detected in these cells from P2 to P10. As caspase3 is well-known to be implicated in the molecular cascade of cell apoptosis (Nicholson 1999), its absence here could suggest that these cells do not die through programmed cell death. Such non-apoptotic cellular death mechanism has been reported during retinal development, where microglia accumulate around astrocytes and exhibit phagocytic activity, leading to astrocytic death (Puñal et al. 2019). A similar mechanism could be implicated here and could be experimentally tested.

Very interestingly, a parallel can be established between clusters location evolution, and the dynamics of mouse retinal angiogenesis. As retinal vascularisation occurs after birth, conducting precise studies about its developmental dynamic has been possible. Thus, it has been documented that the superficial retinal vascularisation, at the RGC layer level, starts around P1, with the first blood vessels emerging from the optic nerve head, then expanding toward the retinal periphery (Dorrell and Friedlander 2006). This developmental pattern is very consistent, both spatially and

temporally, and strictly regulated. It is important to note however that this temporal course of development varies considerably depending on the considered mouse strains (Aguilar et al. 2008). The widely used C57Bl/6 mouse (the model used in this study) exhibits superficial angiogenesis starting at P1, reaching the periphery around P8 (see Figure 16 from (Stahl et al. 2010)). This vascular developmental pattern precisely matches the one observed for clusters location. This could indicate a direct link between clusters emergence and vascularity development. In addition, and as clusters are hyperactive cells, they need an important supply of both nutrients and oxygen, strengthening the link between clusters location evolution and this observed angiogenesis pattern.

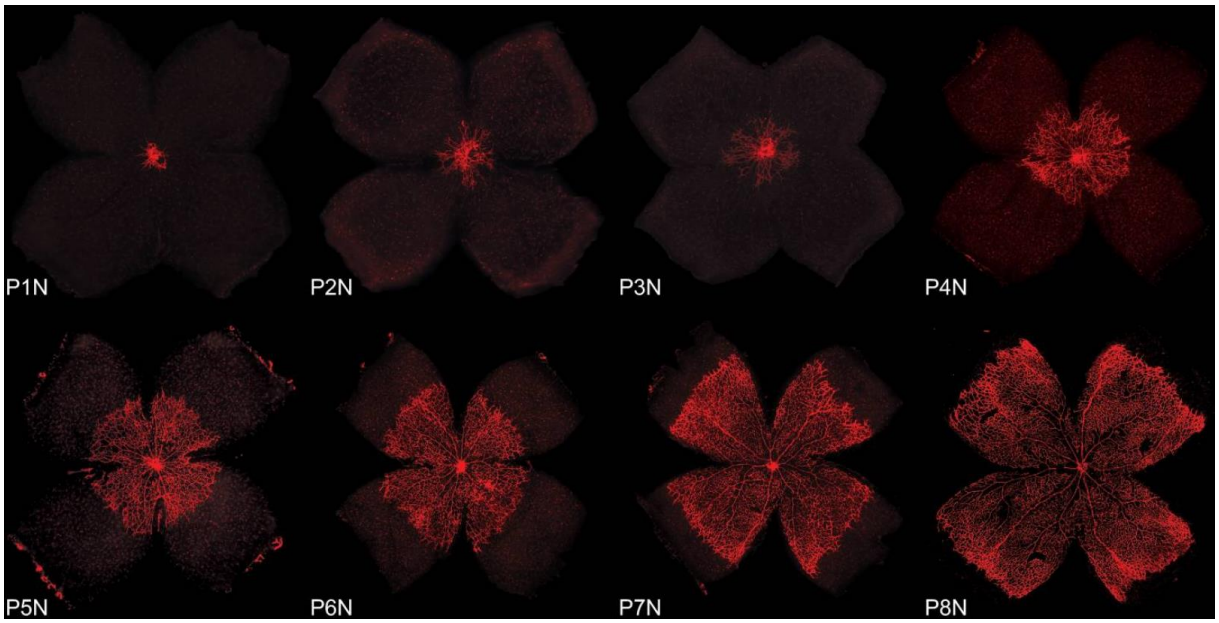

Figure 21: From Stahl et al., 2010, Figure 1: Development of the superficial vascular plexus in C57Bl/6 mouse retinas. Retinal whole mounts from postnatal day (P)1 to P8 were stained for endothelial cells with isolectin B4-Alexa 594 (red). N (normoxia) signifies normal development, as opposed to the hyperoxia time course (shown in Figures 4 and 5 of Stahl et al., 2010). At P1N, the mouse retina is almost completely devoid of blood vessels. The superficial vascular plexus can be seen originating from the optic nerve head. During the first week of postnatal development, the superficial plexus extends radially from the optic nerve head into the surrounding tissue, reaching the retinal periphery at ~P8N.

This however does not indicate the direction of this causality, meaning whether clusters hyperactivity drives the vascularity, or whether the newly created vascularity allows the emergence of these clusters with high metabolic needs.

Interestingly, it has been previously shown in the retina that hypoxia caused by neuronal activity induces angiogenesis (Stone et al. 1995), mediated by up-regulation of vascular endothelial growth factor (VEGF), in response to hypoxia. More recently,

cholinergic neural activity has been demonstrated to play a direct role in angiogenesis of the deeper blood vessels, during the second postnatal week (Weiner et al. 2019). Blocking cholinergic activity results in a reduction of VEGF expression that in turn reduces retinal angiogenesis. However, these manipulations have no effect on the superficial blood vessels, during the first postnatal week, when cluster cells are present. It should also be pointed out that SACs are already present across all the retinal surface from P2. Thus, blood vessels expansion does not follow SACs development, but rather follows clusters location evolution. If the clusters cells are indeed hyper-active, as suggested by our results, they may generate more hypoxic surrounding, leading to angiogenesis in their vicinity.

Very interestingly, new observations obtained from E. Sernagor's lab show a collocation of clusters and the vascularisation edge during development, as shown in Figure 22. A collocation of clusters and expression of HIF-1, a transcription factor activated in hypoxic condition, has also been shown.

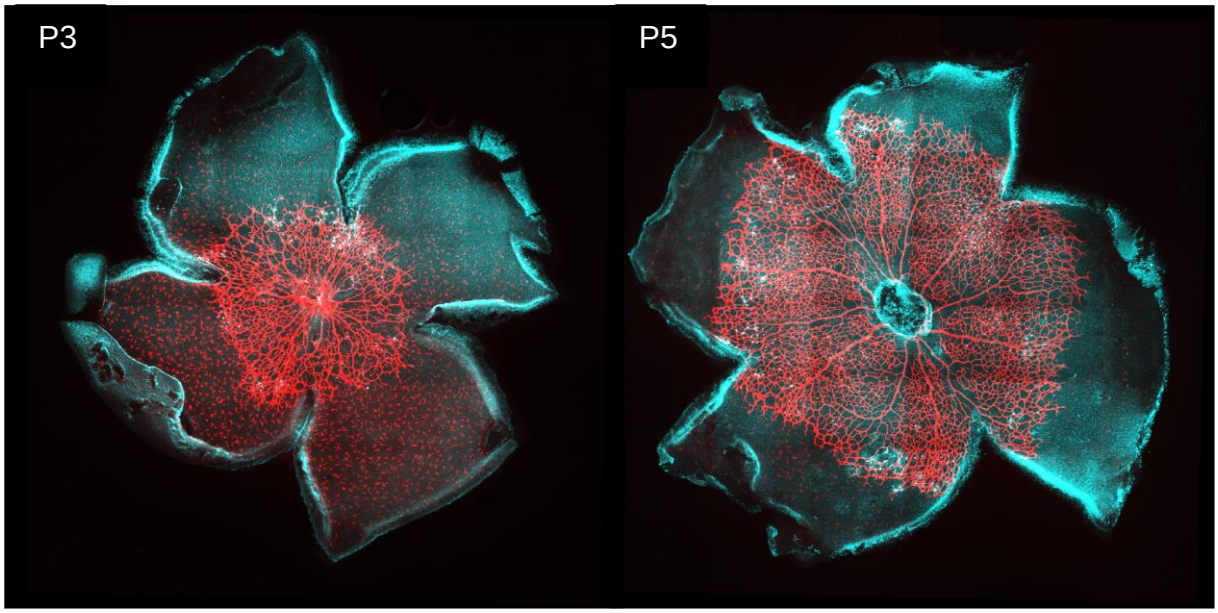

Figure 22: Collocation of auto-fluorescent clusters and vascularisation edge. Red: isolectin B4; cyan: RBPMS; white: clusters. In addition of endothelial cells, some microglial cells are also marked by isolectin B4 in the P3 retina.

In addition, when RGCs activity is chronically enhanced using pharmacogenetics, between P1 and P6 (thus during stage II waves and vascularisation), both clusters and blood vessels migration is arrested, barely reaching the middle retina. Moreover, the blood vessels exhibit excessive branching, especially around the clusters, which can denote a stronger hypoxia around the clusters, due to excessive neural activity. This also suggests that neural activity in the RGC layer (including from the clusters)

plays a crucial role for angiogenesis and blood vessel migration. This is in accordance with previous studies, reporting impaired vascularisation in the absence of RGCs in the Math5-/- mouse retina (Edwards et al. 2012).

Thus, we propose that the transient population of the cluster cells described here actively participates in angiogenesis and elaboration of retinal vascularity through activity-induced hypoxia. By consequence, disturbing the normal development of this new population (exclusively, thus without impacting SACs) or inhibiting this cellular population activity should result in abnormal vascularisation.

Our findings are in agreement with the hypothesis of a transient network of cells that are responsible for waves initiation (Zheng, Lee, and Zhou 2006; Ford, Felix, and Feller 2012). However, instead of a transient network of hyper-connected SACs, we propose here that waves are initialised by a transient population of hyper-connected specialised cells in the RGC layer. This transient population is organised in tight clusters, with evidence of hyper-excitability. Once generated, waves travel across the retinal surface via the SAC network, as well documented. In addition, we propose here that this hyper-active population is an essential component for the establishment of retinal vascularity, by driving angiogenesis.

While a transient population of hyper-active cells has never been reported in the retina, developing cortical areas exhibit such a transient population of subplate neurons that are highly active and synaptically connected to other developing neurons (Luhmann, Kirischuk, and Kilb 2018). The presence of transient, electrically active neurons during early development is thus not a new concept, suggesting a universal mechanism mediating hyper-excitability in developing CNS networks during the critical period for brain wiring.

Chapter 3. BioDynaMo

To be able to conduct my simulations, I took an active part in the development of BioDynaMo, an open-source agent based simulation framework (Breitwieser et al., 2020). During this collaboration, I had the chance to join an active development team and to implement, test or correct several mechanisms – such as mechanical interactions and chemical diffusion – but also to build demonstration cases. The BioDynaMo framework has been developed to address the need for a general-purpose and high-performance platform for biological simulations. Thus, it can be used for numerous applications, including tumour growth simulations, bacterial proliferation or neural development. In addition, the BioDynaMo engine was designed with high performances in mind. To this goal, it takes advantage of the latest developments in computing hardware, being fully parallelised and able to offload computation to hardware accelerators. This enables a single server to run large-scale simulations composed of more than one billion simulation objects (cells, for instance). However, as most biologists do not easily have access to high-performance servers, BioDynaMo is also able to run complex simulations on classic desktop computers or laptops. In this case, simulations are limited to using approximatively ten million objects.

This chapter will present the BioDynaMo framework and agent based simulation concepts for readers who are unfamiliar with this approach. Other readers can directly read Chapter 4. A cancer simulation showcase will also be presented in this chapter, illustrating the potential and flexibility of BioDynaMo.

3.1 Simulation Concepts

Each object in BioDynaMo is denoted as a simulation object, and possesses its own characteristics, such as its 3D geometry (sphere or cylinder, diameter), mass, adherence and position in space. Three generic objects are implemented, cell, neuron soma and neurite element. Specific methods are implemented to access objects attributes or modify them (such as diameter and cylinder length changes or object migration in space). Generic objects can be extended by adding custom attributes and methods. During a simulation, new object creation (for example due to cell division) can take place and is denoted in BioDynaMo as an event. Each event is triggered by a single simulation object but can create multiple new objects. Attributes transmission from the object that triggered the event to the newly created object can be defined by the user, as well as attributes value attribution.

A core concept is that biology modules can be attached to simulation objects. A biology module describes a simulation object behaviour at each simulation time step. It can for example be substance secretion, cell migration or axon extension. The user clearly defines the instructions inside a specific method, and can chose if this biology module will be copied in the case of an event. For instance, the user can decide if the daughter created during a cell division event will inherit its mother biology module or not. As previously stated BioDynaMo is agent based, meaning that each simulation object is independent, without a central organisation unit that orchestrates the behaviour of all simulation objects. Thus, for their biology modules simulation objects only have access to their micro-environment, which consists of other simulation objects and chemical substances of the extracellular matrix in their proximity. To create micro-environments, simulation space is divided into uniform voxels, and simulation objects are assigned to a specific voxel depending on their centre of mass location. The micro-environment is then defined as a sphere with a volume of 27 voxels. The voxel size is chosen to be equal to the largest object in simulation, to ensure all mechanical interactions are taken into consideration.

BioDynaMo is able to take into account physical interactions between all simulation objects such that they cannot overlap, but mechanically repulse each other. To do so, the engine examines if two simulation objects collide with each other at every time step. Only the micro-environment is considered for possible collision search in order to minimise calculations and to ensure AB rules are applied. In the case of a collision detection, mechanical forces acting on both objects are calculated based on the approach taken by CX3D (Zubler and Douglas 2009), such that for two spheres

(Equation 1) $$F_{ij} = \frac{1}{m} \times \left(k\,\delta - \gamma \sqrt{\frac{r_i r_j}{r_i + r_j}\,\delta} \right) \hat{e}$$, where m is the sphere mass, k is the repulsion coefficient, γ the attraction coefficient, r_i and r_j the radii of the spheres, δ the overlap, and $\hat{e}$ the unitary vector pointing from the centre of sphere i in direction of sphere j. If the resulting force exceeds the adherence between the two objects, objects are moved accordingly to the calculated repulsion forces. In the case of interaction with a cylinder (neurite), a virtual sphere is created at the location of the overlap, and repulsion forces are calculated accordingly. As a neurite's centre of mass is located exclusively at its distal end, part of the force is transmitted to the other end depending on the mechanical interaction location along the cylinder. Depending on the interaction location, some displacements can be transmitted to the

cylinder mother or daughters as well. I had the opportunity to take part in the implementation of these mechanical interactions.

Diffusion in 3D of chemical substances in the extracellular space has also been implemented, with the discrete central difference method. This diffusion is supported by a grid in the simulation space and can be of variable resolution. The more points a diffusion grid has, the more precise and realistic the diffusion will be, at the counterpart of more calculation. At each time step, the concentration value of each voxel is updated according to the equation (Equation 2)

$$u_{i,j,k}^{n+1} = \left(u_{i,j,k}^{n} + \frac{\nu \Delta t}{\Delta x^2}\left(u_{i+1,j,k}^{n} + u_{i-1,j,k}^{n}\right) + \frac{\nu \Delta t}{\Delta y^2}\left(u_{i,j+1,k}^{n} + u_{i,j-1,k}^{n}\right) + \frac{\nu \Delta t}{\Delta z^2}\left(u_{i,j,k+1}^{n} + u_{i,j,k-1}^{n}\right) * (1-\mu)\right),$$

where $u_{i,j,k}^{n+1}$ is the concentration value on grid point (*i*, *j*, *k*) at time step *n+1*, *v* is the diffusion coefficient, *μ* is the decay constant, *Δt* is the duration of one time step, and *Δx*, *Δy*, *Δz* are the distances between grid points in the x, y, z directions respectively. Substances concentration distribution can be added artificially (with or without diffusion and decay) and following any user-defined function, or predefined functions such as a Gaussian distribution. For performance optimisation, no diffusion is calculated if the diffusion and decay coeficient parameters are set to 0. I also had the chance to take part in this simulation aspect.

At each time step, the simulation engine executes operations for all simulation objects. An operation can either alter the state of a simulation object (for instance diameter increase), create a new object, or remove an object from simulation. Process of different time scales can co-exist by using an execution frequency for each operation. A frequency operation of one means that the corresponding operation will be executed at each time step, while a frequency of ten means that the operation will be executed every ten time steps. At each time step (or depending on the frequency operation), the engine updates objects spatial organisation (mechanical interactions), then runs all biology modules, and finally updates diffusion grids.

The simulation state (objects position and characteristics, chemical substances concentration and gradient) can be exported every desired time step in order to visualise it using the open-source visualisation software ParaView (https://gitlab.kitware.com/paraview/paraview).

By offering pre-built functions (cell division, dendrite extension, etc.), functionalities (simulation export, visualisation, etc.), and by being built using a general purpose

coding language and a hidden implementation of the engine (parallelisation, hardware optimisation, etc.), BioDynaMo is easily programmable and can be used with only basic C++ knowledge. In addition, this minimises the amount of work, and time, needed to build a use case, and thus quickly implement and verify a hypothesis.

The BioDynaMo source code is available at https://github.com/BioDynaMo/biodynamo and is licensed under the open-source Apache License, Version 2.0.

3.2 Simulation Illustrations

Three general examples demonstrate BioDynaMo's applicability: Cell growth and division, soma clustering and pyramidal cell growth. This work has been done in collaboration with other BioDynaMo developers, Lukas Breitwieser and Ahmad Hesam.

Cellular growth and division

In the first example, the simulation starts with a grid of 40×40×40 cells that are programmed, through a biological module, to grow to a certain diameter and subsequently divide into two smaller cells. These daughter cells inherit their mother biological module and hence, will themselves grow and divide. An illustration of this simulation can be found in Figure 23. This simulation is characterised by a high cell density and slow cell movements due to mechanical repulsion, illustrating mechanical interactions between spherical objects as well as cell divisions process.

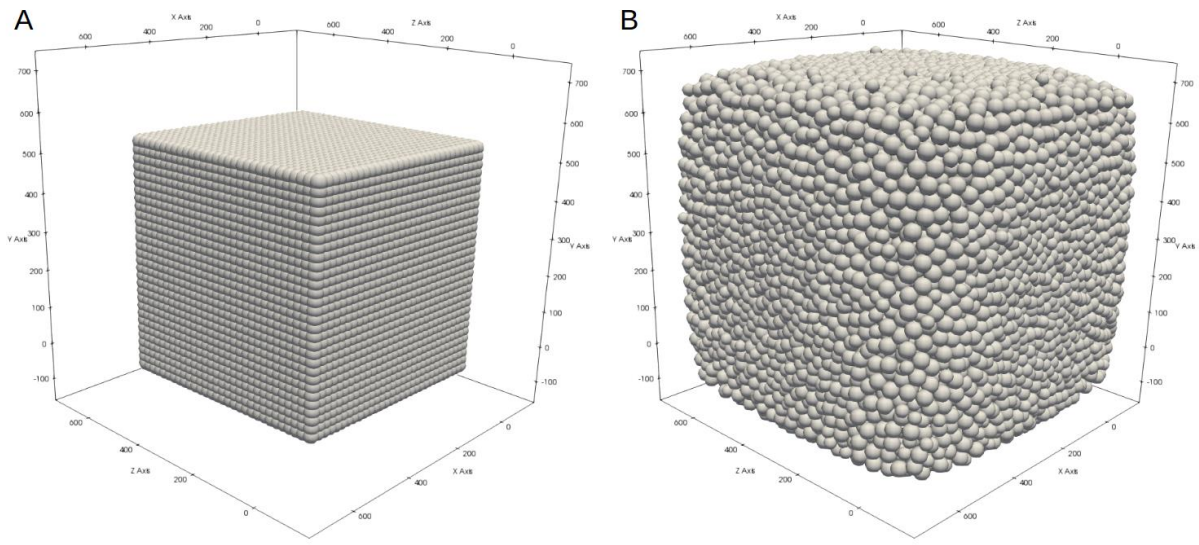

Figure 23: Illustration of grow-divide simulation example. A: Simulation state at the beginning of the simulation (time step 0). **B:** Simulation state at the end of the simulation (time step 100).

Chemical substance secretion and soma clustering

In the second one, cells aggregate depending on external factors and their cell type. The simulation starts as 4000 randomly distributed cells of two different types (A and B) in a cubic space. Each cell secretes a type-specific extracellular substance that will act as an attractant for homotypic cells. Substances diffusion through space follows Equation 2. To allow cells to belong to a specific type and being able to recognise their corresponding substance, we extended the cell object and defined cells as either type A or B. Two biological modules were implemented, one for substance secretion, and one for migration depending on their homotypic substance gradient. During the simulation, clusters of homotypic cells form, as shown by Figure 24. This example illustrates the extracellular substance diffusion mechanism, cell migration depending on a chemical gradient as well as default object extension.

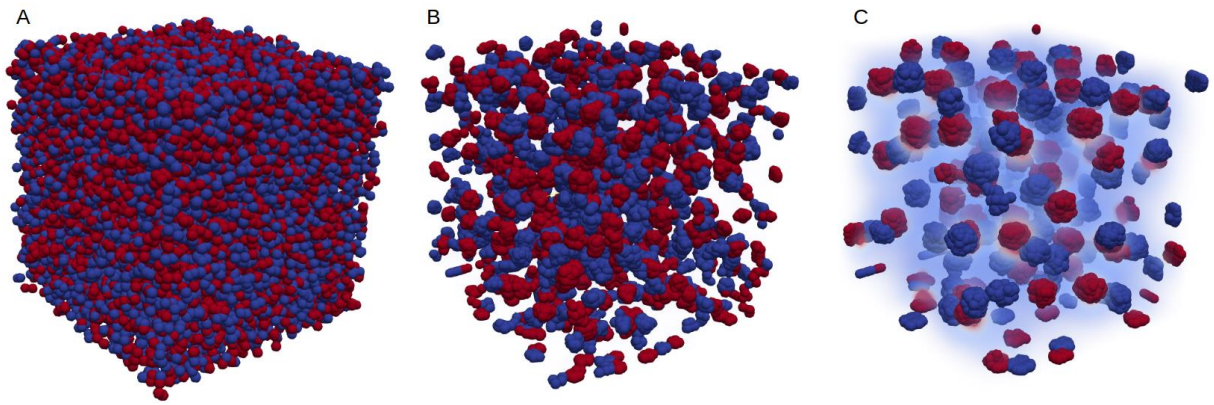

Figure 24: Soma clustering simulation. Each cell of type A (blue) or B(red) secrete a substance A or B and move following its homotypic substance gradient. A: Simulation at t0, cells are randomly distributed. B: Simulation at t18, cells start to form clusters. C: Simulation at t100, cells form clusters. Heat-map of both substances concentration (blue: 0, red: 4000) is overlaid.

Pyramidal cells dendritic arbour growth

Finally, the pyramidal cell growth example illustrates dendritic tree development using chemical clues. The goal here was to demonstrate the capability of BioDynaMo to create neuronal morphologies that are similar to experimentally measured pyramidal neuro morphologies. To do so, a cell body with three initial 0.5 µm long basal dendrites and one initial 0.5µm long apical dendrite are created. Two chemical developmental cues following a Gaussian distribution were initialised along the z axis, acting as attractant for dendrites. Two distinct biological modules describing apical and basal dendrites' growth behaviour were created. Thus, at each time step they define dendrites growth direction, speed and branching behaviour. Apical dendrites’ growth is more driven by the chemical clues and grows twice faster than the basal dendrites. Branching behaviour also differs, apical dendrites having a higher branching rate, but they can branch only on the main branch of the arbour. These simple rules give rise to a straight long apical dendrite with simple branching patterns and more dispersed basal dendrites, as shown in Figure 25A, similarly to what can be observed in real pyramidal cell morphologies. We have been able to tune parameters and compare our simulated neurons using a publicly available database of real pyramidal cells (Mellström et al. 2016). Parameters have been empirically chosen, without fitting method (due to the large number of parameters), but rather using a trial-and-error approach. Two different measures were used to compare our simulated neurons and the 107 neurons composing the real morphologies' database: the average number of branching points, and the average length of dendritic trees. As shown in Figure 25B, C, no significant differences were

observed between the two groups for both measures ($p > 0.05$ with an unpaired T-test), demonstrating the ability of BioDynaMo to model realistic neurons' morphologies.

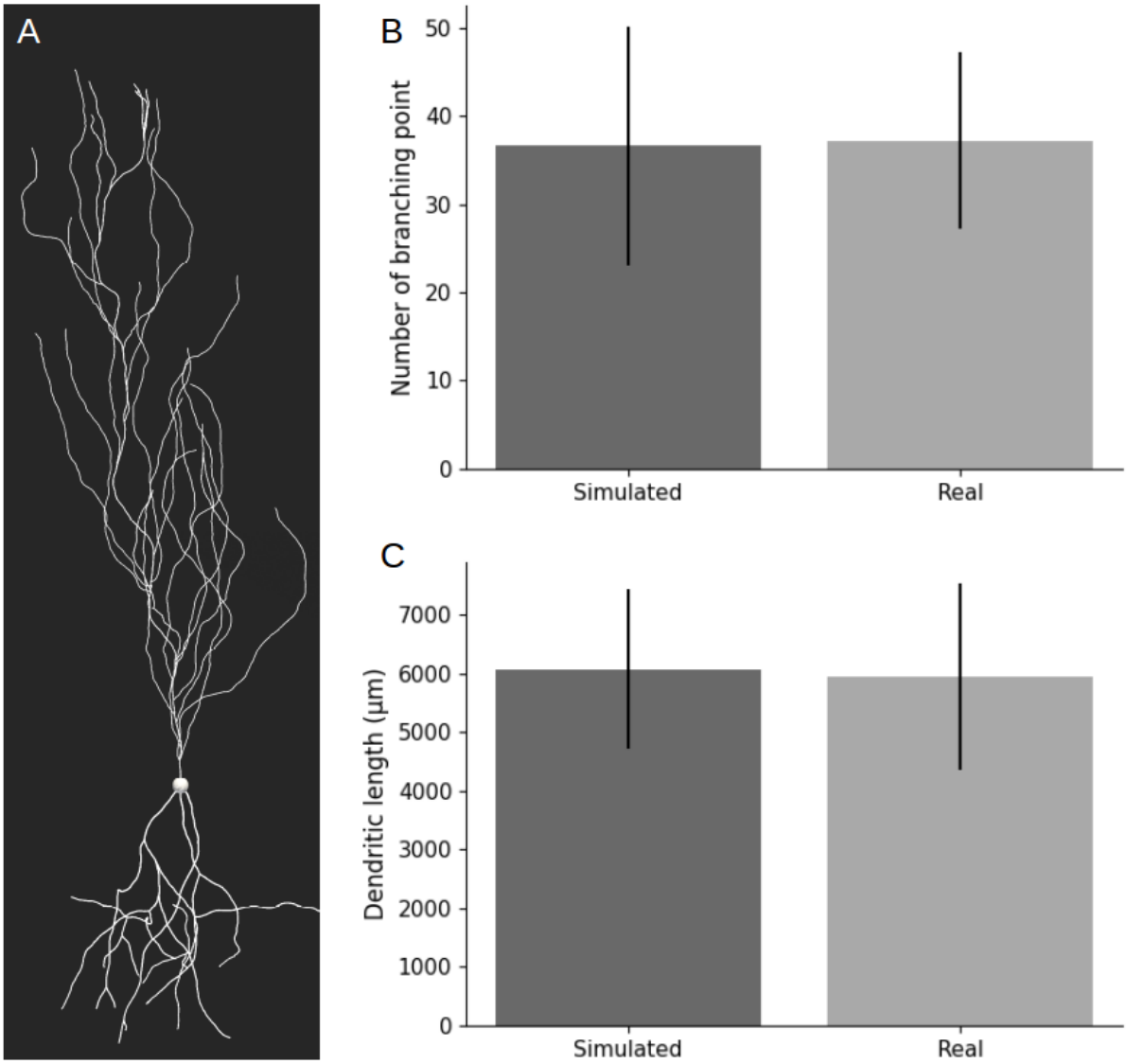

Figure 25: Pyramidal cell growth example. A: Illustration of a simulated pyramidal cell. **B:** Number of branching point comparison between simulated and *in-vitro* cells. **C:** Dendritic length comparison between simulated and *in-vitro* cells. Error bars represent standard deviation.

This simple simulation highlights the differences in growth behaviour needed in order to simulate realistic pyramidal cells dendritic arbours. These results could indicate intrinsic differences between apical and basal dendrites, but also the importance of external developmental cues.

3.3 Performance

These examples also allowed us to measure the performance of BioDynaMo and to analyse its scalability. Scalability refers to the ability of a system to be able to handle more work as the available resources increase as well. A scalable software is more flexible and able to take full advantage of various hardware, from high-performance servers to personal laptop. This provides benefits in both short and long term, as it increases the software performance and the range of hardware it can be run on, but also as it increases software lifespan by being able to take advantage of future hardware advances. One common way to accomplish this goal is to use parallel computing, where several processors execute a process simultaneously. Indeed, a single complex problem (or process) can, in most cases, be divided into smaller ones that can be solved at the same time. By doing so, the process execution time can be drastically reduced. The optimal speed-up offered by parallel computing has been theorised by the Amdahl's law, stating that doubling the number of processors should halve the runtime, and doubling it a second time should halve the runtime again (Amdahl 1967). However, the speed-up is not linear with the number of processors, as it also depends on the percentage of the task that cannot be parallelised. To approach Ahmdahl’s law theoretical maximum speed-up, BioDynaMo has been built such as the number of serial instructions (non-parallelised instructions) has been minimised. Thanks to that, BioDynaMo parallel efficiency is measured between 0.90 and 0.98 depending on the simulation condition.

Graphics processing unit (GPU) acceleration has also been implemented, being however limited to the calculation of mechanical interactions between simulation objects. Nevertheless, a speed-up between 1.1× (cell growth example) and 3.3× (soma clustering example) has been measured when using the GPU acceleration. Of course, the more collision between simulation objects (and so the more mechanical interactions are to be calculated), the more GPU computing offers a benefit.

3.4 BioDynaMo flexibility: a Hybrid Continuum-/Agent-Based Procedure to Model Cancer Development

To illustrate BioDynaMo’s flexibility, we present here its integration with the continuum based simulation framework FEB3 (pronounced Phoebe) (Vavourakis et al. 2017), in order to simulate tumour development. This section presents a simulation showcase and thus can be skipped for readers who directly want to read the RGC development and mosaics formation chapter. During this collaborative work,

I took part in the elaboration of the methodology, the development of the software (agent-based model and interface between FEB3 and BDM), the visualisation procedure and data analysis, but also in the writing and review processes of the published paper (de Montigny et al., 2020).

As previously stated, AB approach allows modelling detailed cellular mechanisms (cellular dynamics, cell-cell interactions, etc.) and can take into account highly heterogeneous system dynamics. Thus, BioDynaMo is particularly well suited for realistic and detailed simulations of small scale (< 10 mm). However, despite its focus on performance, BioDynaMo (similarly to other AB modelling frameworks) is not well suited for larger scale simulation, especially if diffusion grids are implemented. Indeed, schematically, each point of a diffusion grid occupies 8 bytes in computer memory (substance concentration stored as a double floating-point format). Thus, one diffusion grid in a cubic simulation space of 10,000µm and with a resolution of 10,000 (one diffusion point per µm), would require 8,000 Gigabytes of memory ($10{,}000^3 \times 8$ bytes). For comparison, a diffusion grid in a cubic space of 1,000µm (resolution of 1,000) would only require 8 Gigabytes of memory.

On the other hand, continuum models, such as FEB3, allow large-scale simulations. Indeed, these approaches are based on the resolution of differential equations, and are thus more efficient than AB approaches. They are especially efficient to model substance concentration dynamics, such as oxygen consumption and diffusion from blood vessels. However, this efficiency is done at the expense of a concrete representation of objects. Thus, cell populations and environment characteristics are usually abstractly represented. In addition, it is very challenging to model independent cell behaviour with a continuum based approach. This can negatively impact the verisimilitude of these models, especially when discrete cellular dynamics influence the results (such as it is the case in small-scale simulations).

Hence, combining both modelling approaches would greatly benefit simulation efficiency without impacting their verisimilitude. Such models have already emerged in the past decade (Anderson 2005; Gerlee and Anderson 2007; Hunter and Viceconti 2009; Altrock, Liu, and Michor 2015) and are referred as hybrid models. They are usually built by building interfaces across different modelling solutions, a continuum based and an AB one. The resulting hybrid model, and the question it aims to answer, depends directly on the two interfaced modelling solutions. Our approach follows the same principle, using an interface between FEB3 and

BioDynaMo. We have chosen to apply this hybrid solution to model glioma development. Gliomas are a common type of primary CNS tumours (Goodenberger and Jenkins 2012) characterised by a median survival of 6.5 to 8 years for low-grade gliomas, to 1.25 years for glioblastoma multiforme (Maher 2001). While they were believed to be initiated by glia, new evidences point toward an expansion from restricted progenitors, or neural stem cells. They are characterised by their quick progression and highly invasive behaviour, resulting in diffuse tumour, that is, infiltration by cancerous cells of otherwise healthy brain tissue. This, in particular, is responsible for the lack if effective therapeutic approaches and for tumour recurrence after tumour resection. Despite much research on the topic, the invasion dynamics and its underlying mechanisms remain unclear. Mathematical and computational models can play an important role in extrapolating findings from *in-vitro* experiments to in *in-vivo*.

Here, we use FEB3 in a macroscopic scale to model growth factor transport and oxygen while we use BioDynaMo at multiple microscopic scales to model discrete cell dynamics.

3.4.1 Macroscopic scale: continuum model

These simulations consist in a cubic space of $20mm^3$, with sufficient distance from the focal region of interest (tumour location) in order to avoid boundary conditions impacting the simulation. At the macroscopic (length scale) level, the continuum-based model accounts for three compartments, each consisting of various species: the biochemical components' compartment, the cells compartment and the extracellular matrix (ECM). The biochemical compartment encompasses the balance of oxygen and nutrients, growth factors and enzymes. The cells' compartment encompasses the cells involved (both host and non–host tissue), while the ECM compartment collectively accounts for the structural aspects of the stroma. Each component is described at the continuum level through a boundary value problem: the balance of each species is mathematically modelled via coupled differential equations.

Oxygen

Assuming the presence of a microvascular network that supports tissue with a uniform source of oxygen and other nutrients, oxygen diffuses into the tissue and is consumed by the cells. Thus, the balance equation of the oxygen saturation level, denoted as ξ, is calculated by $\frac{d\xi}{dt}=\frac{\partial}{\partial X}.\left(D_{\xi}\frac{\partial \xi}{\partial X}-V\xi\right)+\alpha_{\xi}V-\sum_{i=1}^{N_c}\delta_{\xi i}c_i, \forall X\in\Omega$, where c_i denotes each cell species, D_ξ is the isotropic diffusion coefficient for oxygen (given in m^2day^{-1}, α_ξ is the constant oxygen production rate owing to the supply, from the microvascular network (expressed in day^{-1}), $\delta_{\xi i}$ is the oxygen consumption rate by each of the i-th cell species (in day-1) and Ω is the total volume of the biological tissue. Function $V=\left(1-\xi-\xi-\xi\right)^{\gamma_V}$ (where $\gamma_V \in (0, 1)$) controls the supply of oxygen from the blood vessels to the adjacent tissue and so to the cells.

Growth factors

The present macroscopic model accounts for chemical cues that are responsible for cell activation, growth, mitosis, migration etc. The balance of these growth factors (each species denoted by g_j in dimensions: mg/mm^3) is described by a set of reaction-diffusion equations that account for random spatial diffusion, growth factor secretion and uptake by the various cell species, c_i, and the natural decay. The corresponding partial differential equations (PDEs) are expressed as $\frac{dg_j}{dt}=\frac{\partial}{\partial X}.\left(D_j\frac{\partial g_j}{\partial X}-Vg_j\right)+\alpha_{\xi}V-\sum_{i=1}^{N_c}\alpha_{ji}c_i-\delta_j g_j, \forall X\in\Omega; j=1,\ldots,N_g$, where D_j is the isotropic diffusion coefficient for each of the chemical agents involved, g_j (in m^2day^{-1}), δ_j represents the decay rate of the agent, and α_{ji} is the gross rate of the growth factor g_j due to both secretion and uptake by the cells (given in day^{-1}).

Matrix metalloproteinases (MMPs)

In addition to this, the proposed model accounts for the dynamics of the concentration of MMPs, noted μ in our model. MMPs (also referred as matrix-degrading enzymes) are enzymes that degrade the extracellular matrix. The balance of the MMPs concentration in the extracellular space obeys a PDE identical to the growth factors one, with corresponding model parameters: D_μ, $\alpha_{\mu i}$ and δ_μ.

ECM

This model treats the ECM, e_p, as a porous solid medium of porosity, where the volume fraction occupied by stromal components (collagen, fibronectin, laminin) is:

$\epsilon_f = 1 - \epsilon_p$ .The present model assumes a fixed volume fraction for the interstitial fluid, whereas the structural integrity and composition of the ECM, and hence ϵ_S, is assumed to change with time. We describe structural changes at the stroma using a first-order ordinary differential equation for the ECM volume fraction that accounts for the remodelling of the ECM, and the degradation of the matrix due to the presence of chemical cues (here metalloproteinases are modelled to cleave ECM fibres) at the interstitium such as $\frac{d\epsilon_S}{dt} = \left[\sum_{i=1}^{N_c} \alpha_{\epsilon i} c_i + \alpha_\epsilon\right] H - \delta_\epsilon \mu \epsilon_S, \forall X \in \Omega$, where δ_ϵ is the ECM degradation rate due to the presence of matrix degrading biochemicals μ (given in days^{-1}), α_ϵ is the ECM self-regeneration rate and $\alpha_{\epsilon i}$ is the cell-stimulated ECM remodelling (e.g. deposition of collagen or/and fibronectin as a result of cell activity). Also, $H = (1 - \epsilon_S - \epsilon_c - \epsilon_f)^{\gamma_H}$ with the scalar exponent parameter: $\gamma_H \geqslant 1$.

Cellular populations

Finally, the population of each cell species is controlled by the following PDE:

$\frac{dc_i}{dt} = \frac{\partial}{\partial X} \cdot \left(\frac{\partial c_i}{\partial X}\right) + \alpha_i, \forall X \in \Omega; i = 1, \ldots, N_c$, where α_i is the cell production (if negative-valued, the cell decay) term. The first term of the equation on the right-hand side describes the potential for migration or invasion of the i-th cell phenotype. Both terms are calculated by the solver at the microscopic domain (AB model) and then projected to the macroscopic domain solver, as explained in section 3.4.3. The domain of analysis is discretised here with 3D elements (tetrahedrons, hexahedrons) while time discretisation and numerical solution of the above equations was carried out through an explicit Euler scheme. All parameters used in the macroscopic scale simulations can be found in Table 2.

Symbol	Parameter Description	Value(s) [units]	Adapted from
ϵ_f	volume fraction of interstitial fluid	0.2	[1]
D_ξ	oxygen diffusion coefficient	1.7×10^{-9} [m^2 /s]	[2]
α_ξ	oxygen production rate (from vasculature)	40.555×10^{-5} [s^{-1}]	[3, 4]
Y_V	vascular supply exponent	0.05	this work
D_j	GF diffusion coefficient	1.157×10^{-11} [m^2 /s]	[5]
$\alpha_{j,i}$	GF production rate from CGs	5×10^{-9} [s^{-1}]	[3]
δ_j	GF decay rate	2×10^{-9} [s^{-1}]	[3]
D_μ	MMPs diffusion coefficient	8.64×10^{-11} [m^2 /s]	[6, 7]
$\alpha_{\mu,i}$	MMPs production rate from CGs	4×10^{-8} [s^{-1}]	[8]
δ_μ	MMPs decay rate	3×10^{-8} [s^{-1}]	[6, 9]
$\alpha_{\epsilon,i}$	ECM remodelling rate due to cell type "i"	0	this work
$\alpha_{\epsilon,i}$	ECM self-remodelling rate	1×10^{-7} [s^{-1}]	this work
Y_H	ECM remodelling exponent coefficient	3.5	this work
δ_ϵ	ECM degradation rate due to MMPs	10^{-4} [s^{-1}]	[6]

Table 2: Macroscopic scale model parameters. Adapted from: [1] (Sciumè et al. 2014) [2] (Wang and Li 1998) [3] (Wu et al. 2013) [4] (Valero et al. 2013) [5] (Bray 2001) [6] (Wood et al. 2012) [7] (Karagiannis and Popel 2006) [8] (Vavourakis et al. 2017) [9] (Anderson 2005)

3.4.2 Microscopic scale: agent-based model

At the microscopic scale, simulations consist of 100μm^3 simulation spaces filled with cells explicitly represented as spheres. Cells are present in several types, either host: neurons (Ne), glial cells (G) or cancerous: cancerous glial cells and cancer-associated fibroblasts (CAF). Also, the model distinguishes between normoxic-state cancerous glial cells (CG) and hypoxic-state cancerous glial cells (hCGs). For Ne and G species, the cell densities considered are 5 × 104 per mm^3 and 105 per mm^3 respectively to match observed density in human cortex. The initial population of the CG species has a density of 104 cells per mm^3, which for simplicity are evenly distributed at the centre of the domain of analysis (within radius ~0.5 mm).

Figure 26 illustrates in a flowchart the phenotypic behaviour of host (Ne, G), cancerous (CG, hCG, CAF) and necrotic cells (NC) with respect to the level of oxygen saturation, chemical cues and the extracellular matrix (ECM).

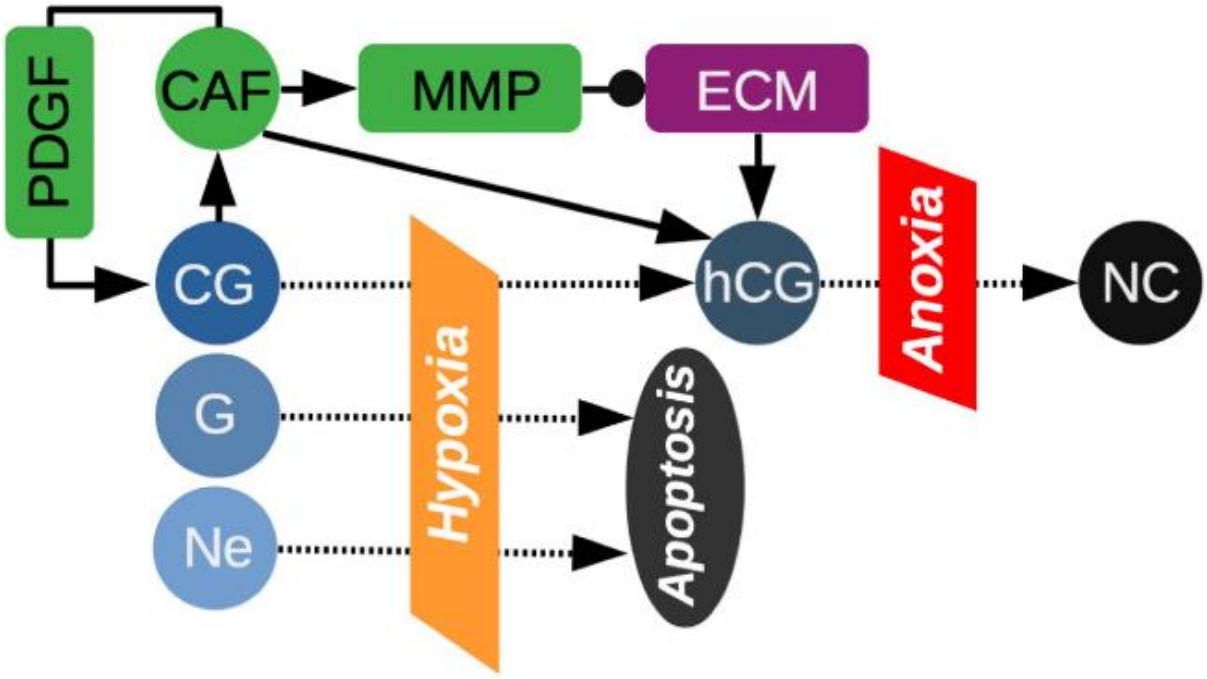

Figure 26: Phenotypic behaviour and cellular interactions. Ne: neurons, G: healthy glial cells, CG: cancerous glial cells, hCG: hypoxic cancerous glial cells, NC: necrotic cells, CAF: cancer-associated fibroblasts, PDGF: platelet-derived growth factor, MMP: matrix metalloproteinases, ECM: extracellular matrix.

The present model assumes a passive role for the host cells unless oxygen drops below a certain level. In this case they die and corresponding cell agents are removed from the simulation. However, host fibroblasts trans-differentiation is implicitly described by explicitly increasing the CAF population (in proportion to the CGs population). CGs are prone to unregulated cell growth and division, as long as the oxygen/nutrients concentration in the matrix doesn't decrease below a certain threshold (oxygen saturation level must be $\geqslant 0.9$). The growth rate of CGs was set by matching simulation results of our *in-silico* hybrid model to *in-vitro* data of cancerous cells' growth rate. However, cancer cell mitosis is modelled as a stochastic event governed by a probability density function having uniform distribution. The increase of the CG population size leads to a decline of oxygen concentration in the medium, resulting in a hypoxic micro-environment, since blood vessels oxygen support is insufficient. The present model assume that only cancerous cells (normoxic or hypoxic) can transform permanently into necrotic cells (NC). CGs under hypoxic conditions (hCG) can express a migratory phenotype dictated by local gradients of the oxygen saturation level (chemotaxis), while ECM microstructural properties become important to the cells' preference to migrate (durotaxis). In this model, tumour cells degrade the ECM locally (as outlined briefly in Section 3.4.1) and hence they prefer moving towards a denser matrix. Through trans-differentiation of native

fibroblasts to CAFs, CGs secrete matrix metalloproteinases (MMP) that in turn degrade the ECM by breaking the structural fibres of the stroma (collagen, fibronectin), thus, resulting in a heterogeneous ECM. Relevant observations have been reported in gliomas *in-vitro* and *in-vivo*. In addition, CGs through CAFs also discharge platelet-derived growth factors (PDGF) for vasculogenesis, which subsequently fuel the unregulated proliferation of CGs. Transition between cell states (normoxia↔hypoxia→necrosis) is modelled as a stochastic event depending on a given cell's internally encoded rules in interaction with the micro-environment. Mechanical interaction between cells are taken into account, as explained in 3.1.

3.4.3 hybrid macro to micro model

The hybrid multiscale model couples the macroscopic scale with the microscopic scale using the representative averaging volume (RAV) technique. Briefly, each quadrature point of a (macroscopic) finite element is associated with a unique representative cubic volume, the RAV, which contains a cloud of randomly distributed cells, as illustrated by Figure 27.

Each cell population, their physiological condition and state (oxygen levels, chemical cues, …), at each representative volume are determined by linear interpolation of the nodal (macroscopic) data to every point within the finite element. In turn, these nodal data are determined by the macroscopic initial conditions imposed at the beginning of the simulation, or obtained from the corresponding nodal data evaluated from the previous time increment of the FEB3 solver. Subsequently, the cells' dynamics within each RAV is simulated by the agent-based modelling solver at each quadrature point. After several internal iterations of the microscopic level simulator (BioDynaMo), cell populations are re-evaluated for each species, and for each representative volume. Subsequently, the average cell rate at each RAV and the average direction vector of the cells escaping the bounds of the representative cubic volume is calculated. These data are evaluated for each species and then up-scaled back to the macroscopic simulator (FEB3). In summary, as illustrated in Figure 28, the simulation procedure of the proposed *in-silico* hybrid procedure is partitioned, with FEM and ABM working alternatively and passing necessary data interchangeably by projection and averaging until all simulation steps have been completed.

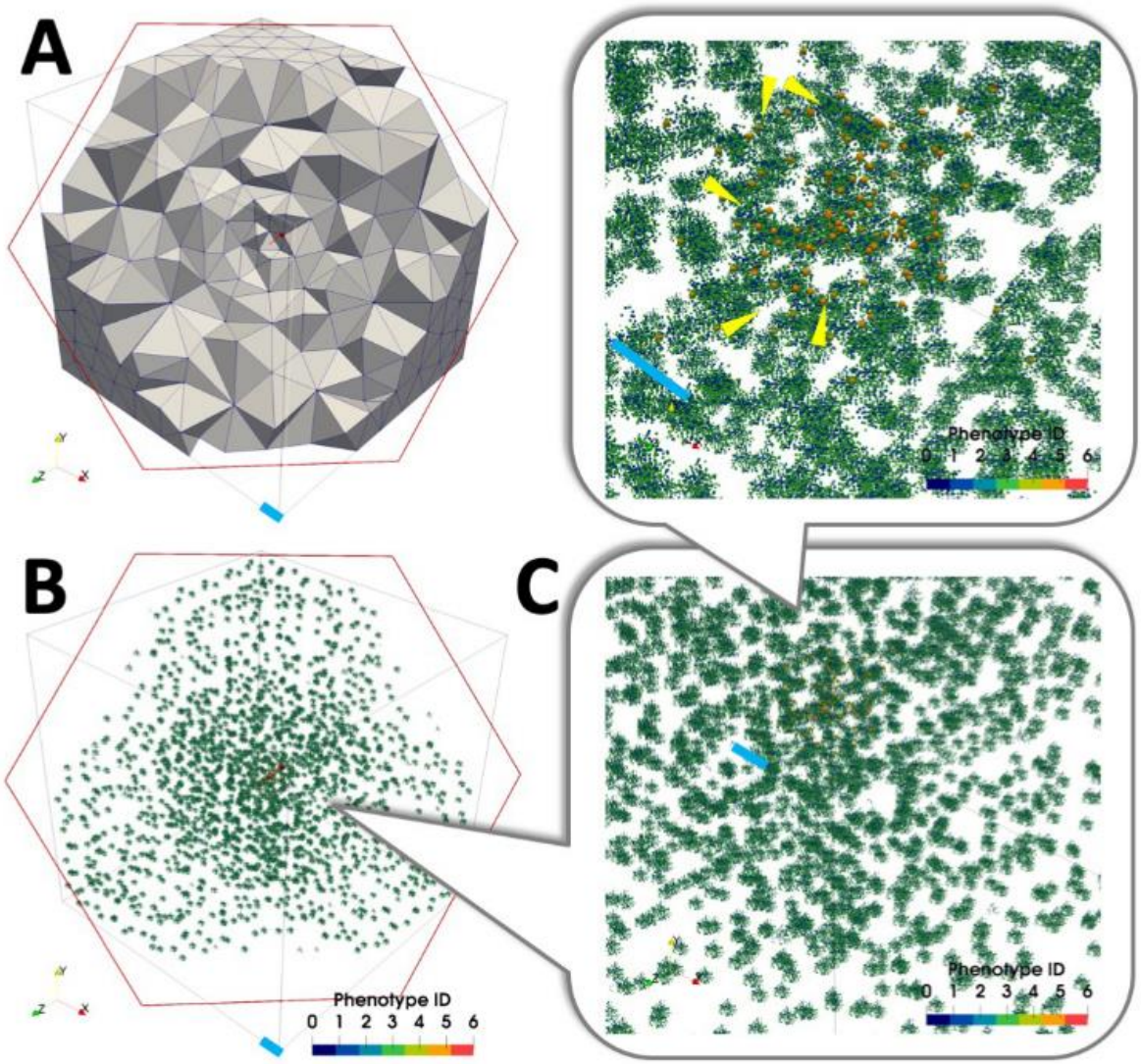

Figure 27: Illustration of a hybrid multi-scale simulation. A: Cut-through illustration of the 3D unstructured finite element mesh (outline surface mesh is shown slightly transparent). **B:** From the same perspective, the representative averaging volumes (RAVs) are illustrated in the 3D domain (scaled up for visualisation purposes) with each agent represented as a small spheroid, coloured with respect to their phenotype (purple for the neurons, green for the healthy glial cells, whereas orange for the normoxic cancerous cells and red for the hypoxic ones). **C:** From bottom to top, consecutive zoom-in pictures (2.5×, 9×) depict the cells, shown as spherical agents and coloured with respect to their phenotype. The yellow arrows point out the scattered cancerous cells, located at adjacent RAVs at the centre of the 3D domain of analysis. Light blue thick line depicts a one millimetre scale, while the cells size in the RAVs is scaled up by a factor of five for illustration purposes.

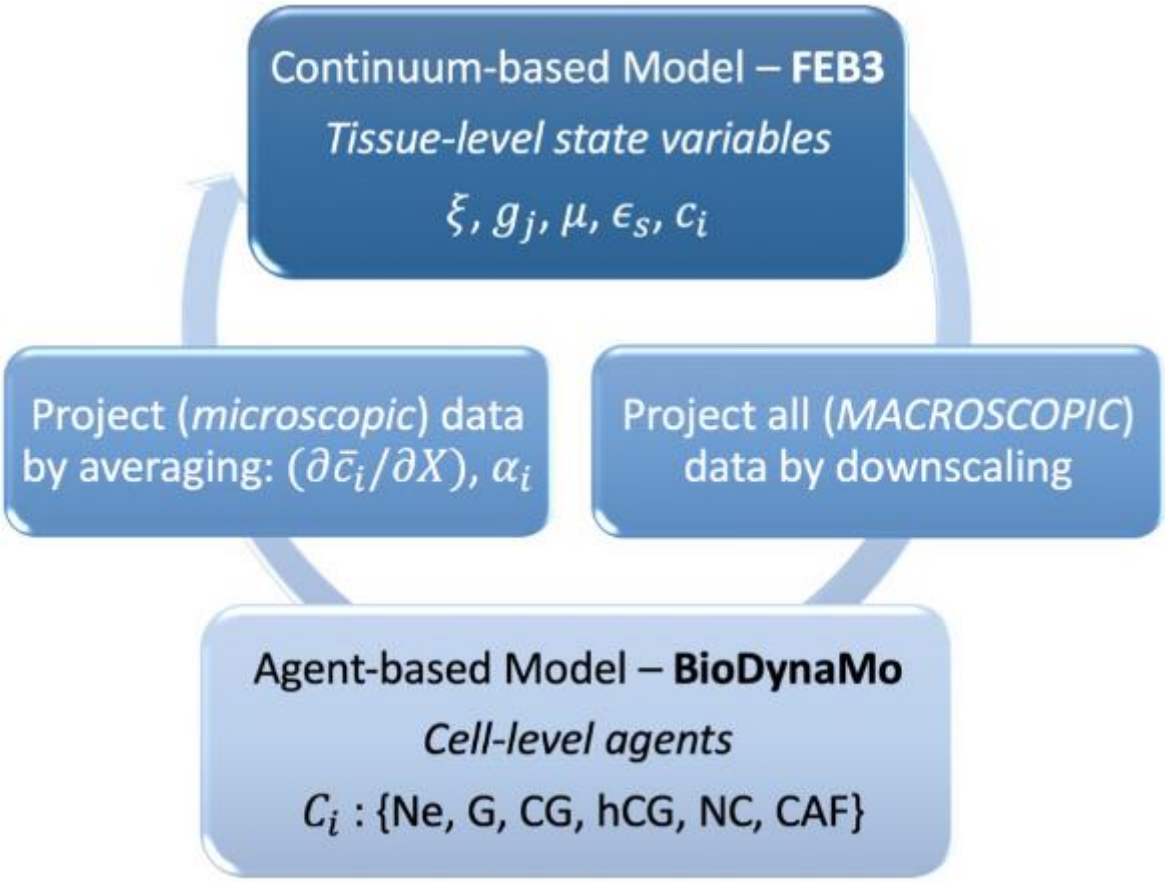

Figure 28: Schematic representation of the hybrid multi-scale modelling communication between the two solvers.

This *in-silico* cancer model distinguishes two layers of implementation that are identified from the two spatial scales involved. The AB modelling method has been implemented using BioDynaMo, and thus in a multi-threaded, object-oriented, C++ code. BioDynaMo employs several open-source libraries: ROOT, ParaView, and OpenMP. Moreover, the continuum-based method has been implemented in a scalable C++ code, and incorporated into the existing numerical analysis framework FEB3. FEB3 is founded on several high-performance, open-source numerical libraries: PETSc, libMesh, GSL, blitz++ and the MPICH library. The tissue domain finite element three-dimensional meshes have been generated using Gmsh, and decomposed and distributed across multiple processors using the ParMETIS library. The coupling and communication between FEB3 and BioDynaMo has been achieved within FEB3. All simulations were carried out on a desktop machine having an Intel i9-7940X CPU (@3.1 GHz ×14) and 128 GB main memory, operating Linux (Ubuntu 18.04, kernel version: 4.15.0–54-generic). Simulations of a 30 days tumour development (44,000 simulation steps) required on average 4 h to be completed while the main memory usage was less than 3 GB. However, it is worth highlighting here that the code of our solvers was not fully optimised.

3.4.4 Results

Low-grade tumour growth

Using our *in-silico* hybrid model, we simulated the development of a low-grade tumour over the period of a month. These low-grade tumours are well-differentiated and characterised by a slower growth rate compared to high-grade tumours. Thus, in this simulation, cancerous cells express a slow growth rate and no migratory behaviour. In the resulting simulation, tumour expansion is observed as shown in Figure 29, where the tumour diameter increases from about 37 mm at day 10 to about 64 mm at day 30. Similarly, the tumour volume increases from 180 mm^3 (±7.1 mm^3) at day 10 of the simulation to 784 mm^3 (±28 mm^3) at day 30, as shown in Figure 29C. This tumour growth is supported by cell divisions in the microscopic domains. Thus, the cumulative number of cells composing the tumour mass in all microscopic domains rises up to 54,800 (±1120 cells/mm^3) at the end of the simulation. This link between macroscopic domain and individual cell elements is represented in Figure 29A. As CGs proliferate, and as we assume a uniform microvascular network providing a uniform source of oxygen, a hypoxic region emerges at the centre of the tumour (Figure 29D), leading to CGs expressing the hCG phenotype. Later on, as oxygen becomes scarcer, hCGs survival becomes impossible thus creating a necrotic centre, as shown in Figure 29G. This oxygen deprivation also impacts healthy hosts (Ne and G), whose densities decrease as they get closer to the tumour centre, even reaching a density of 0 at the centre. These characteristics can be observed at both macroscopic and microscopic scales in Figure 29A, where the tumour centre, composed of NCs (coloured in blue) and hCGs (coloured in red), is surrounded by CGs (cells coloured in orange). The tumour obtained at the end of this simulation is shaped as a spheroid and clearly defined, with no isolated CGs outside of the tumour mass as shown in Figure 29D.

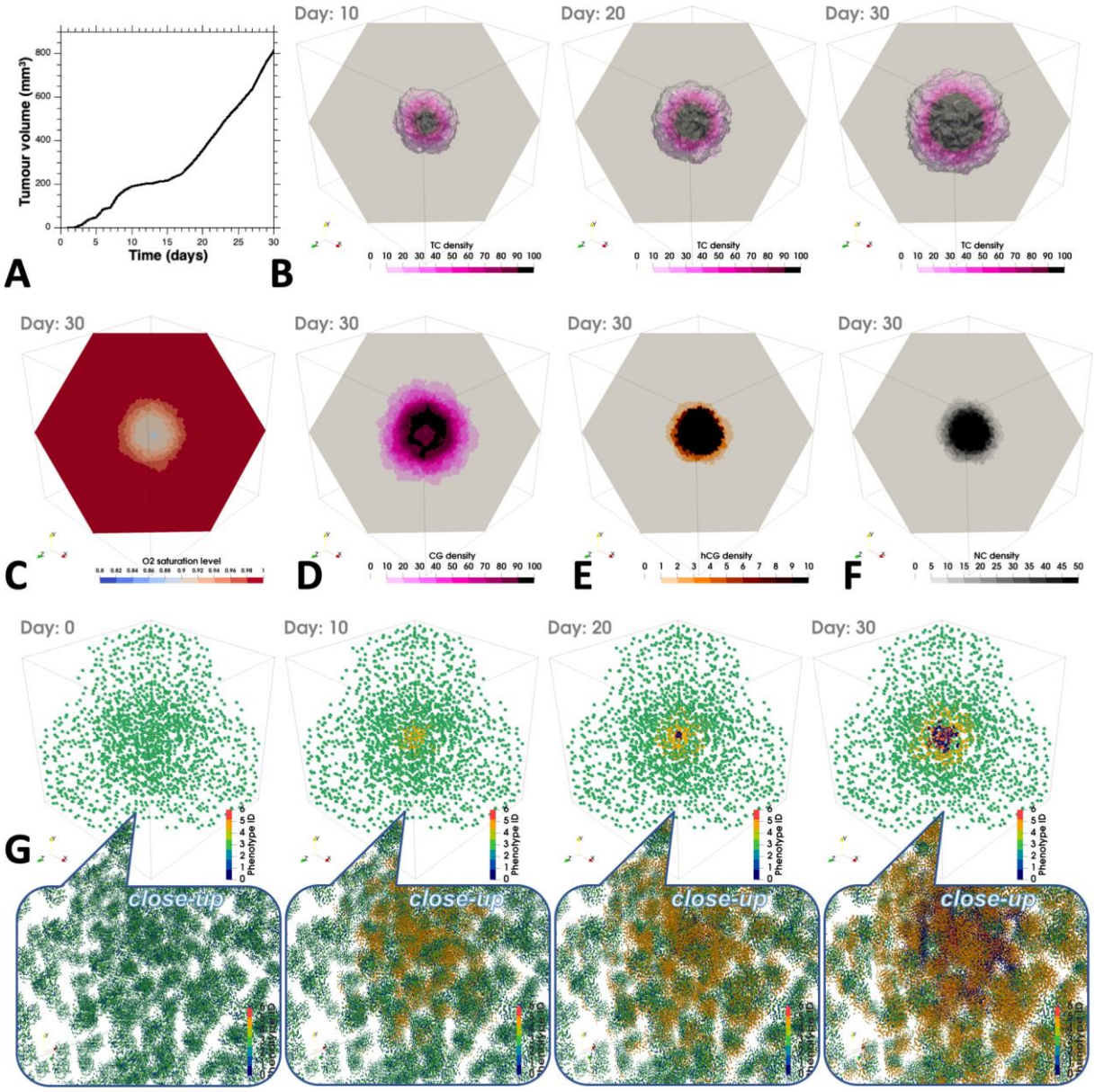

Figure 29: Time snapshots of a growing *in-silico* low-grade brain tumour. A: History plot of the development of the tumour volume. **B:** Cut-through of the macroscopic domain of analysis illustrating the tumour cell density ($\times 10^3$ per mm^3) at different time points, with the semi-opaque surface depicting the outline of the tumour. **C:** Distribution of the oxygen saturation level at day 30 where a poorly oxygenated tissue core is formed. **D,E,F:** Snapshots of the CG, hCG (hypoxic CG) and necrotic cells density (scale is in $\times 10^3$ cells/mm^3) respectively. G: Same perspective cut-through of the macroscopic domain (finite elements are transparent) depicting the microscopic domains in enhanced view and at different time points. The colours correspond to the cell phenotypes involved in the simulation (blue for the neurons, green for the healthy glial cells, orange for the normoxic cancerous cells, red for the hypoxic ones, dark blue for necrotic cells).

High-grade tumour growth

High-grade brain tumours are more malignant tumours and thus have worse prognosis than low-grade tumours. They are known to have a high regrowth behaviour, even after complete surgical removal of the tumour mass, in some cases

due to their more diffused organisation. In order to simulate such more aggressive tumour development, three modifications have been made to our model, the first one being the secretion of MMPs by CAFs. These enzymes, by degrading the ECM, facilitate cell migration and so give rise to more invasive behaviour of cancerous cells. Secretion of a growth factor has also been added, recapitulating the beneficial effect of PDGF on tumour growth. Finally, in this simulation cancerous cells adopt a "go-or-grow" phenotype, where hCGs express a high migratory behaviour without the possibility to grow or divide, while CGs grow and divide, without exhibiting any migratory behaviour. In other words, when cancerous cells are in a hypoxic environment, they express a migratory behaviour. Oxygen supply is assumed to be uniform across all the tissue. Simulation results for this case are illustrated in Figure 30. During tumour development, we can observe that the early growth behaviour, and the resulting shapes, are still similar between low-grade and high-grade tumours, as they have a well-defined spherical shape (Figure 29B day 10 and Figure 30B day 10 respectively). Likewise, their volumes are still in the same range, being 151 mm^3 and 212 mm^3, respectively. This means that under the specified conditions, high-grade tumours exhibit a volume 1.4 times bigger than low-grade ones. However, differences emerge as the development continues, with a bigger volume difference between low and high-grade at day 20 (2.1 times bigger for the high-grade) and day 30 (2.4 times bigger for the high-grade), tumours reaching a final volume of respectively 784 mm^3 and 1890 mm^3 after 30 days of development. Moreover, differences in shape can be observed at day 30, high-grade tumours exhibiting a more diffused phenotype with outgrowth of lower density at the surrounding of the main tumour mass, while low-grade tumours remain well-defined and more spherical (Figure 29B and Figure 30B). In addition, healthy cells (glials and neurons) are significantly affected by the tumour, as cancerous cells spread covering a larger area when compared to the low-grade case (see Figure 29B,D and 30B,D respectively). As evident in Figure 30C, due to the pronounced hypoxia and anoxia, healthy cells within the tumour region are susceptible to abrupt apoptosis. Figure 30G, depict the absence of cells from both healthy populations respectively. Finally, secretion of MMPs by the proliferative CGs at the rim of the tumour leads to degradation of the ECM both at the tumour localisation and surrounding. As a consequence, these changes of the ECM density facilitate migration of cancerous cells, hence, the expansion and spread out of the glioma. All these factors give rise to more aggressive tumours, exhibiting high growth rate and migratory behaviour, with a more

diffused phenotype characterised by outgrowth of low CGs density at the surrounding of the main tumour mass.

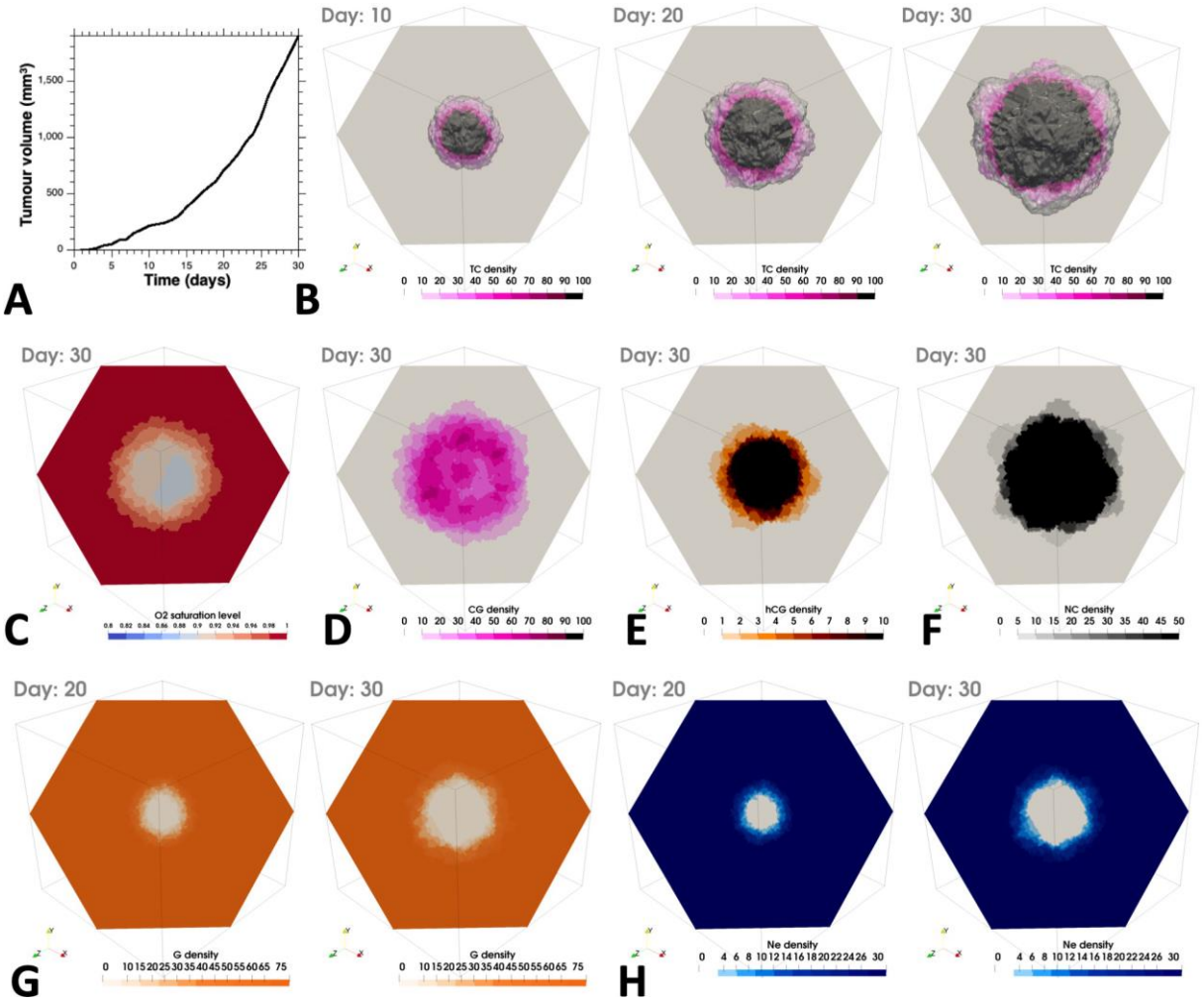

Figure 30: Time snapshots of a growing *in-silico* high-grade brain tumour. A: History plot of the tumour volume in cubic millimetres. **B:** Cut-through of the macroscopic domain of analysis illustrating the tumour cell density ($\times 10^3$ per mm^3) at different time points, with the semi-opaque surface depicting the outline of the tumour. **C:** Distribution of the oxygen saturation level at day 30 where a poorly oxygenated tissue core is formed. **D, E, F:** Snapshots of the cancerous glial cells, the hypoxic ones and the necrotic cells density (scale is in $\times 10^3$ cells/mm^3) respectively. **G,H:** Distribution of the glial cells and the neurons respectively ($\times 10^3$ per mm^3) at two time points. Notice the absence of native cells within the necrotic core of the tumour.

3.4.4 Discussion

The proposed *in-silico* hybrid platform demonstrates potential to simulate the development of brain gliomas in a detailed but computationally cost-effective manner. For the working cases presented in this paper, each simulation took about four hours to finish on a multi-core desktop machine. In particular, the AB solver required the simulation of between 5.5×10^5 to 7×10^5 agents coupled via the RAV technique with a mesh (of 8 cm^3 tissue volume) consisting of ~4×10^3 tetrahedral elements in total. If

AB alone had to be employed to simulate glioma growth in a domain of the same size, it would have required for the solver to simulate approximately ~1.3 billion agents. The scale of data involved in such an analysis is numerically prohibitive even for a moderate sized computer cluster. Furthermore, the proposed *in-silico* hybrid platform was capable to recapitulate the dynamics of a growing tumour in the brain that may exhibit either a low-grade or a high-grade behaviour. In addition to this, the platform recapitulated the main points of brain tumour necrosis and oxygen deprivation, as well as the dynamics of a heterogeneous developing tumour matrix.

The present model could be extended to incorporate more elements (for instance tumour-induced angiogenesis) or used as a platform for the study of the efficacy and delivery of drugs to tumour spheroids in *in-vitro* experiments. This modelling approach could be further employed for a wide range of biomedical problems, other than cancer. In particular, models of healthy biological development, biofilm growth, immune system dynamics, or synthetic tissue growth are based on relevant dynamics. In particular, it could be used to simulate retinal development at the level of the whole organ.

Chapter 4. RGC Development and Mosaics Formation

As presented in Chapter 3, agent-based models are particularly well suited to build realistic simulations of neuronal tissue self-organisation. In order to investigate how the RGC layer and its mosaics develop, we present in this chapter an implementation using BioDynaMo of three theories of mosaic self-organisation, cell-fate, cell death and cell migration. We report here that CM yields the most regular mosaics, while CD can create regular mosaics only if the death rate is kept below 30%. Once this death rate is reached, CD appears to have a negative impact on mosaic regularity. We also present a modelling of realistic RGC dendritic arbour shapes, and discuss the requirements to match the observed morphological diversity of RGCs.

4.1 Methods

4.1.1 RGC mosaics development

All simulations took place in a cubic space of 1300µm^3, with cells of 7 to 8µm diameter randomly distributed (uniform distribution) in a space of 1000µm×1000µm×22µm. The initial cell density has been set to 8600 cells/mm^2, in order to reach the RGC density — around 3000cells/mm^2 reported in literature (Sanes and Masland 2015a) and around 3500cells/mm^2 in our measures — once programmed CD mechanism is over. Mechanical interactions between simulation objects are taken into account, such that they cannot overlap, and mechanically repulse each other. The time step has been set such that 160 steps simulate one day of development. Mosaic formation simulations run for a maximum of 2240 steps, corresponding to 14 days of development.

The global RGC population is subdivided into 43 types. Some have been precisely documented, such as the On or On-Off DSGC, the melanopsin RGCs (M1 to M5), the LED, On or Off Alpha RGCs and the Off J-RGCs, and their population densities and dendritic arbours characteristics are known. However, these precisely documented RGC only represent 19 types, and so only about 60% of the total RGC population (~1700 cells/mm^2 over ~3000cells/mm^2) (Sanes and Masland 2015). RGC types composing the remaining 40% of the population have been estimated using results from Sanes and Masland (2015), Reese and Keeley (2015) and Baden et al. (2016). These authors state that a large number of RGC types are still unknown and these cells are probably sparsely distributed across the retina. Thus, we implemented 24 additional RGC types of various but low densities. All implemented RGC types and their corresponding starting and final densities are summarised in Table 3.

43 diffusion grids of 650×650×650 points, representing voxel edge size of 2µm (volume of 8µm^3), were also created to support the diffusion of 43 chemical substances. Each chemical substance corresponds to a defined RGC type, and is characterised by a diffusion coefficient of 2 (see diffusion equation in section 2.2.1).

Simulation states are exported every sixteen simulation steps, which means that there are a total of ten simulation states per developmental day. These exports encompass all cells characteristics: 3D position, type and diameter. *Using this information, it is possible to measure the mosaic regularity and the cell density of all RGC types, the RGC layer thickness and RGC death rate through development.*

Cells biology modules

Cells are created with no predefined types when simulating the cell-fate (CF) mechanism. Otherwise, cells of each RGC type are created matching their experimentally observed initial density. Four biology modules describing cellular behaviour at each time step have been generated and assigned to each cell created.

Substance secretion

The first biology module implements substance secretion depending on the cell type. This secretion corresponds to an increase of substance concentration by 1 at the cell centre position. Undifferentiated cells do not secrete any substance.

Mosaic formation

The second biology module implements CF, cell death (CD) and cell migration (CM) behaviours.

CF is implemented such that substances act as an inhibitor for cell differentiation, preventing nearby undifferentiated cells to adopt the same type. In this way, neighbouring cells preferentially choose to differentiate into other RGC types. CF is the first event to occur during simulations, because CD and CM mechanisms operate on differentiated cells.

The CD mechanism simply corresponds to the cells removing themselves from simulation if their corresponding substance concentration is higher than a defined threshold. In this way, the clusters of homotypic cells exhibit high death rates and become sparser. As the cell density decreases, the initial multilayer collapses into a RGC monolayer. This is not currently implemented as a mechanical consequence of

pressure from other tissues or cell layers (due to cell growth and multiplication in a constrained physical space), but by having cells moving along the z axis toward the centre of the RGC layer, using their chemical cue. CD is triggered after completion of CF, and continues until a steady-state is reached, around a death rate of 65%. This steady-state is reached without global controllers but depends on the chosen concentration threshold triggering cell death. If this threshold is low the steady-state will be reached with a high death rate, while if this threshold is high the steady-state will be reached with a low death rate. In addition, for an identical threshold value, a low density cell population will exhibit a lower final death rate than a high density population. Therefore, the chosen threshold value depends on the initial cell density of the considered cell type. Each threshold value has been hand-tuned, fallowing a trial and error approach in order to reach a steady state around 65% of death rate. Fitting methods have also been tried for parameter estimation (least squares fit, parameter screening, maximum likelihood estimation), but they have proven unable to be applied or to find parameters values, due to the too important number of parameters.

CM is implemented such that the homotypic substances act as a repulsive factor. Thereby, cells exhibit short distance avoidance, moving tangentially against their substance gradient, distancing themselves from homotypic neighbours. CM is triggered after completion of CF, at the same time as CD, and continues either until a steady state or day 13 is reached. Development conditions incorporating all combinations of these three mechanisms have been investigated. As the mechanisms influence each other, parameters vary depending on the implemented mechanisms. The CD mechanism parameters were chosen for each RGC type such that its final death rate is about 65%. The CM parameters were chosen (hand-tuned, empirical approach) depending on the CD parameter value and such that the interaction is kept to close range distance. Table 3 summarises all the parameters.

Internal clock and dendrites extension

The third biology module implements an internal cell clock used to trigger the subsequent mechanisms. At each time step, this internal clock has a 96% chance to increase by 1. This parameter value has limited influence and only prevents all cells from having the exact same timing. Decreasing chance to increase the internal clock just slows down the transition from one mosaic formation mechanism to the other.

Finally, the fourth biology module is used to create dendrites at the end of mosaic formation and will be explained in section 4.1.2.

All simulation codes are available on github (https://github.com/JeandeMontigny/new_ret).

Cell type	Type name	Start density cells/mm²	Final density cells/mm²	D Death	FD Death	FDM Death	FDM Migration
0	on-off_dsgca	357	125	2.0367	2.0334	2.023	2.02
1	on-off_dsgcb	357	125	2.0367	2.0334	2.023	2.02
2	on-off_dsgcc	357	125	2.0367	2.0334	2.023	2.02
3	on-off_dsgcd	357	125	2.0367	2.0334	2.023	2.02
4	on-off_m3	57	20	1.9872	1.9855	1.9855	1.983
5	on-off_led	714	250	2.116	2.098	2.08	2.065
6	on-off_u	57	20	1.9872	1.9855	1.985	1.983
7	on-off_v	57	20	1.9872	1.9855	1.985	1.983
8	on-off_w	171	60	2.001	1.9978	1.996	1.994
9	on-off_x	143	50	1.9968	1.9945	1.994	1.9925
10	on-off_y	114	40	1.994	1.993	1.993	1.991
11	on-off_z	114	40	1.994	1.993	1.993	1.991
100	on_dsgca	114	40	1.994	1.993	1.993	1.991
101	on_dsgcb	114	40	1.994	1.993	1.993	1.991
102	on_dsgcc	114	40	1.994	1.993	1.993	1.991
103	on_aplha	114	40	1.994	1.993	1.993	1.991
104	on_m2	160	56	2	1.9953	1.994	1.992
105	on_m4	57	20	1.9872	1.9855	1.985	1.983
106	on_m5	57	20	1.9872	1.9855	1.985	1.983
107	on_o	428	150	2.05	2.0425	2.035	2.031
108	on_p	286	100	2.022	2.018	2.012	2.01
109	on_q	286	100	2.022	2.018	2.012	2.01
110	on_r	228	80	2.011	2.0082	2.004	2.002
111	on_s	171	60	2.001	1.9978	1.995	1.993
112	on_t	171	60	2.001	1.9978	1.995	1.993
113	on_u	143	50	1.9968	1.9945	1.994	1.9925
114	on_v	143	50	1.9968	1.9945	1.994	1.9925
115	on_w	97	34	1.993	1.9934	1.989	1.987
116	on_x	57	20	1.9872	1.9855	1.985	1.983
117	on_y	57	20	1.9872	1.9855	1.985	1.983
118	on_z	57	20	1.9872	1.9855	1.985	1.983
200	off_aplhaa	114	40	1.994	1.993	1.993	1.991
201	off_aplhab	114	40	1.994	1.993	1.993	1.991
202	off_m1	180	63	2.006	1.9979	1.998	1.996
203	off_j	571	200	2.078	2.065	2.058	2.049
204	off_mini_j	1000	350	2.179	2.155	2.134	2.098
205	off_midi_j	228	80	2.011	2.0082	2.004	2.002
206	off_u	57	20	1.9872	1.9855	1.985	1.983
207	off_v	57	20	1.9872	1.9855	1.985	1.983
208	off_w	171	60	2.001	1.9978	1.995	1.993
209	off_x	143	50	1.9968	1.9945	1.994	1.9925
210	off_y	114	40	1.994	1.993	1.993	1.991
211	off_z	106	37	1.9935	1.9928	1.989	1.988

Table 3: Implemented RGC types and parameters used for different conditions. D: death mechanism only. **FD:** fate and death mechanisms. **FDM:** fate, death and migration mechanisms. **Death:** concentration threshold for death mechanism. **Migration:** concentration threshold for migration mechanism. Parameters have been empirically chosen.

4.1.2 Dendritic development

RGC dendritic development has been simulated by having two chemical substances (On and Off) normally distributed. These developmental cues could represent the

developmental guidance given from SACs dendrites to RGCs dendrites (Galli-Resta et al., 2008; see section 1.1.2 and 1.4.2). This guidance can be achieved through secreted cues (notably including molecules from the neurotrophins, semaphorins and ephrins families) or through the existence of electric fields (Graves et al., 2011). The two chemical substances concentration varies from 0 to 1, and they are positioned at 43 and 67µm along the z axis, with a variance of 6 and 8µm respectively. The centre of the RGC layer is located at 27µm along the z coordinate, meaning that these two chemical cues are located at a distance of 16µm and 40µm from the RGC layer centre respectively. Position and variance of chemical cues were set such that simulated RGC dendrites location matches observed average peak distance for On (15.9µm ±5.3) and Off (40.4µm ±8.3) dendritic lamination distance from RGC cell bodies (measured from Sümbül et al. 2014). A schematic representation of dendrites chemical guidance initialisation can be found in Figure 31. These two substances act as developmental cues for RGC dendritic growth. Depending on the cell type, dendrites will be attracted to either one or both of these chemical clues.

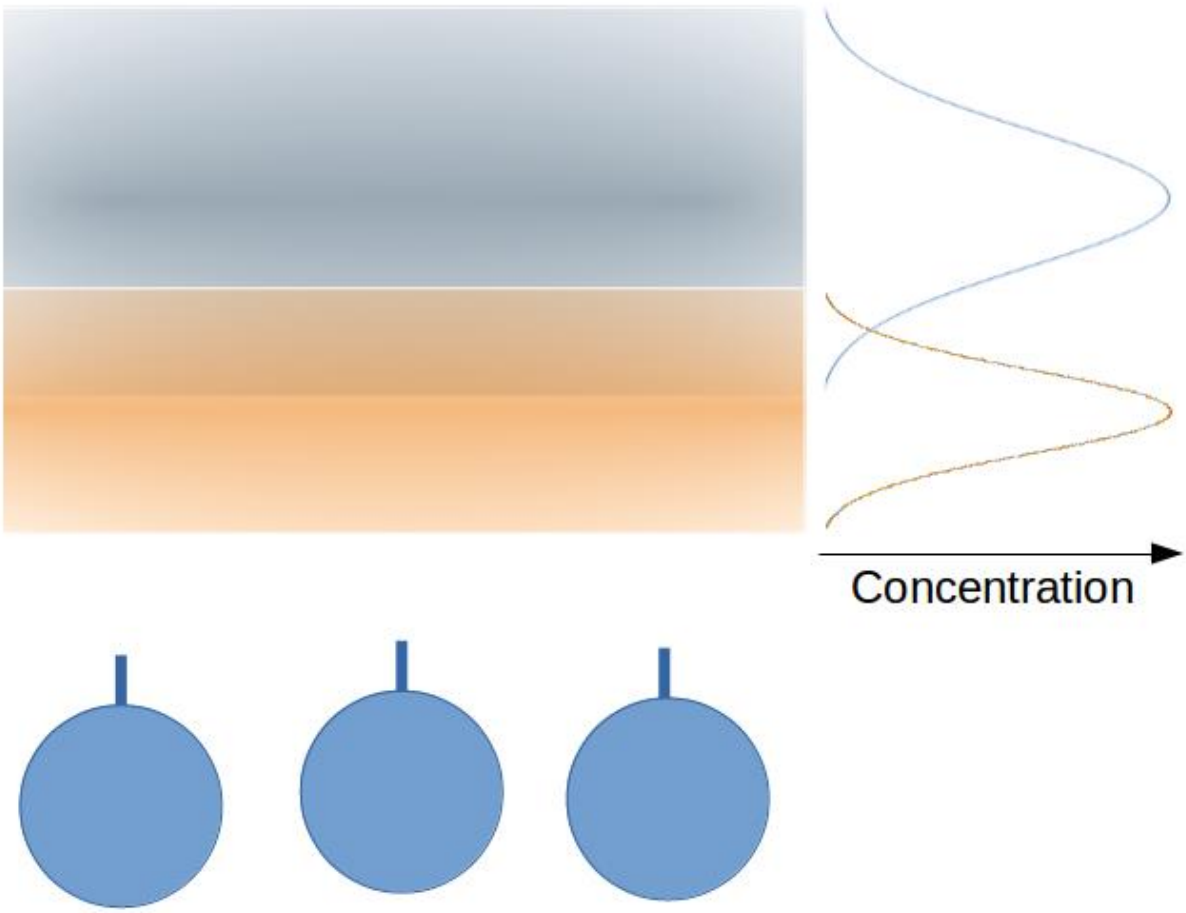

Figure 31: Dendrites chemical guidance initialisation. On and Off chemical cues are represented in orange and blue respectively. They are respectively located at a distance of 16µm and 40µm from the RGC layer centre.

At the end of mosaic formation, cells extend their dendrites with their number depending on the cell type. The range of dendrite numbers per cell type are shown in Table 4. It has been chosen for cells to extend dendrites only at the end of mosaic formation for several reasons: 1. The effects of inter-cellular dendritic interaction on mosaic formation are still unclear and so would lead to a non-precise modelling. 2. RGCs cellular spacing has been reported to take place even in the absence of homotypic dendritic contacts (Galli-Resta 2002; Lin, Wang, and Masland 2004). 3. The current status of the framework does not allow cellular migration once cells have extended dendrites (due to technical limitations). Dendrites are created with a biology module describing their growth behaviour at each time step. In brief, at each time step the growth direction is calculated depending on the chemical cue gradient, the dendrite's direction (current axis) and some randomness. In addition, the dendritic diameter tapers as dendrites grow away from the soma, until it reaches a certain minimal diameter, preventing it from growing any further. A mechanism of dendrite retraction has also been implemented, recapitulating the "searching" behaviour of dendrites. First, a dendrite can retract if it is growing too far from its chemical clue. In particular, retraction is triggered when the chemical guide concentration at the dendrite's growth cone location is below a first threshold of 0.01. The dendrite will keep retracting until a second concentration threshold of 0.02 is reached. Once the dendrite's tip is back at that second threshold concentration, it restarts growing. In this way, dendrites express a more realistic behaviour, being able to search for the correct developmental cues, as commonly observed in developing neurons (Luo and O'Leary 2005; Portera-Cailliau et al. 2005). Such a retraction process has been previously implemented in other simulations (Bauer et al. 2014). Likewise, the retraction mechanism allows simulating homotypic competition for space. Two dendritic arbours of homotypic cells will avoid overlapping and one of them will instead choose to retract a branch surrounded by homotypic dendrites. To avoid a O(n2) time complexity with n being all the objects in simulation (more than 10 million), only dendrites in close neighbourhood (radius ≤ 1.44µm) are considered for homotypic competition.

Two simulation conditions have been investigated, using either three or thirteen behavioural growth rules. In the condition of three growth rules, dendritic growth behaviour for RGC of the same type (On, Off, On-Off) are identical. However, when thirteen growth rules are applied, dendritic growth behaviour depends on the RGC type (for instance DSGC, off Alpha RGC, J-RGC, …). Attribution of a specific growth

rule to a RGC population has been decided depending on the available morphological description of that RGC population in the literature. Thus, some RGC groups that are distinct for the mosaic creation share the same dendritic growth rules. More specifically, the thirteen growth rules consist of: On-Off DSGC (four RGC types), On-Off Melanopsin (one RGC type), On-Off LED (one RGC type), On-Off generic (six RGC types), On DSGC (three RGC types), On Alpha (one RGC type), On Melanopsin (three RGC types), On generic (twelve RGC types), Off Alpha (two RGC types), Off Melanopsin (one RGC type), Off J-RGC (one RGC type), Off mini-J-RGC and Off midi-J-RGC (two RGC type) and Off generic (six RGC types). In this way, a dendritic growth behaviour has been attributed to each of the 43 RGC types used for mosaics formation. RGC groups sharing the same growth behaviour are either known to exhibit the same dendritic morphology (for instance On-Off DSGC) or have not been precisely described in the literature (generic growth rules). All parameters used are recapitulated in Table 4.

Dendritic arbours are exported at the end of the simulation in swc format, a widely used open format for the description of dendritic tree morphologies. Each neuron is composed of points defined by their x, y, z location, a unique id number, the id number of the point they are attached to and the nature of each point (soma, dendrite, branching point, terminal dendrite). Simulated RGCs are then compared to a database of 363 real RGC morphologies from Sümbül et al., 2014, publicly available at http://neuromorpho.org. To do so, key morphology features have been extracted: dendritic arbour diameter, anisometry score and number of branching points. The arbour diameter consists of the disc diameter containing 95% of all dendrite points. The anisometry score is calculated as a ratio between a perfect circular distribution of dendrite points around the soma and a 2D representation of the measured distribution of dendrite points. Thus, the anisometry score increases for more asymmetric dendritic arbours (not evenly distributed around the soma). These features have been selected based on their capability to form coherent groups of cells from the Sümbül database, using a k-means clustering method. The selected morphology measures demonstrate their relevance as the number of clusters in a k-means clustering, determined by an elbow method for optimal value of k, is either four or five for each RGC type (On, Off, On-Off), while three to six defined morphologies have been described for each of these RGC types.

Similarly to parameters used for mosaic formation simulations, dendritic growth simulations parameters have been hand-tuned, following a trial and error approach.

For each measure of a considered population, parameters have been tuned such as it matches the corresponding population's measure from the Sümbül database. Simulations results are particularly sensitive to parameter changes, such as the shrinkage value or the bifurcation probability.

Comparisons between simulated and Sümbül database dendritic arbours have been conducted using the Mann-Whitney U-Test on each morphology feature score distribution, for each RGC population (On, Off, On-Off).

Scripts used for mosaics and dendrites data processing or analysis are available at the address https://github.com/JeandeMontigny/scripts.

Cell type	Dendritic Growth rule	Number Of root	Shrinkage	Bifurcation Probability	Randomness Weight	Gradient Weight	Old direction Weight	Preferred Direction
0 1 2 3	On-Off DSGC	3, 7.5	0.00035	0.0062	0.7	0.2	4.5	0
4	M3	3.4, 5.8	0.00048	0.0052	0.4	0.2	4.5	0
5	LED	3.4, 5.8	0.0007	0.018	0.5	0.2	4.5	0
6 7 8 9 10 11	On-Off generic	3, 7.5	0.004	0.09	0.5	0.2	4.5	0
100 101 102	On DSGC	3.5, 6.8	0.00055	0.0082	0.4	0.2	4.5	0
103	On Alpha	3.2, 6	0.0005	0.006	0.4	0.2	4.5	0
104 105 106	On Melanopsin	3.2, 6	0.00044	0.00489	0.4	0.2	4.5	0
107 108 109 110 111 112 113 114 115 116 117 118	On generic	3.55, 7.6	0.0042	0.09	0.4	0.2	4.5	0
200 201	Off Alpha	3.2, 6	0.00044	0.007	0.4	0.2	4.5	0
202	off Melanopsin	3.2, 6.2	0.00045	0.0058	0.4	0.2	4.5	0
203	Off J-RGC	3, 5.5	0.00036	0.00682	0.6	0.2	4.5	{0.05, 0.05, 0}
204 205	Off mini-J-RGC Off midi-J-RGC	3, 5.5	0.00064	0.011	0.6	0.2	4.5	{0.05, 0.05, 0}
206 207 208 209 210 211	Off generic	3.2, 6.6	0.00038	0.0044	0.5	0.2	4.5	0

Table 4: Implemented parameters for RGC dendritic arbour development.

4.1.3 Measuring mosaic regularity

Before modelling retinal mosaics, and in order to assess the regularity of these mosaics, it is crucial to investigate different methods to measure their regularity, and to select the most appropriate one. For this purpose, we selected five measures: the mosaic Delaunay triangulation segment length (DTS) distribution, the mosaic Voronoi diagrams areas (VDR) distribution, the Voronoi diagram angles (VDA) distribution, the Regularity Index (RI) and the closest neighbour (CN) distribution.

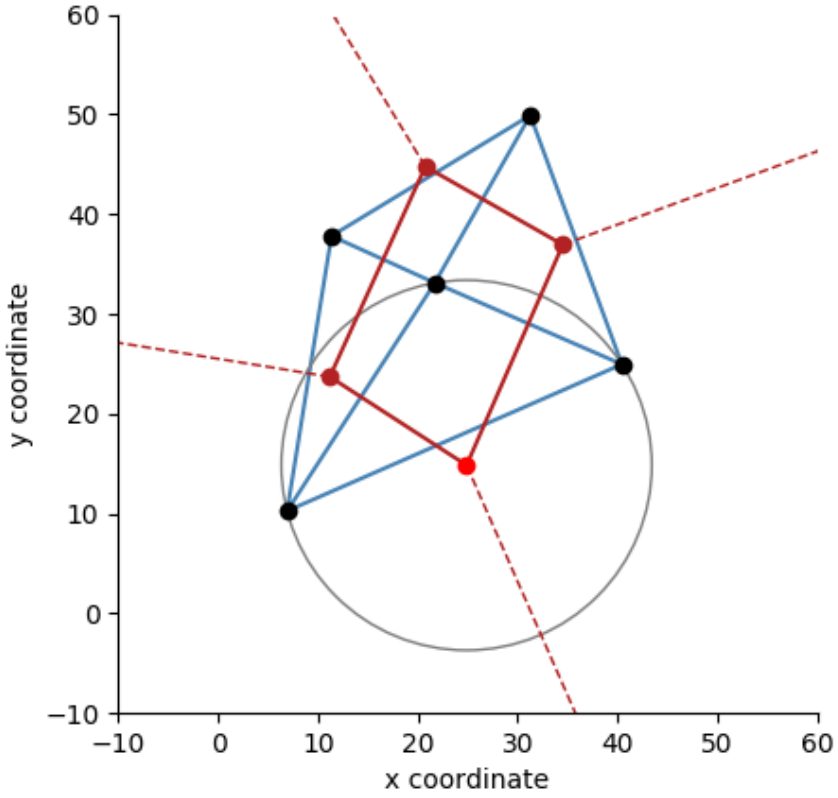

Figure 32: Illustration of Delaunay triangulation and corresponding Voronoi diagrams. Cells are represented as black dots. Delaunay triangulation is displayed as blue lines. One Delaunay triangle circumcicle is displayed in grey, with its centre in bright red. All Delaunay triangles circumcicle centers are displayed in red. Red lines represent Voronoi diagrams. Dashed red lines belong to Voronoi diagrams with a point outside of the region.

Delaunay triangulation is a specific triangulation such that no point of the considered set is inside the circumcircle of any triangle (see blue lines and grey circle of Figure 32). Thus, DTS is the distribution of all triangle vertices length of the mosaic Delaunay triangulation. The Voronoi diagram results directly from the Delaunay triangulation, such that the circumcenters of Delaunay triangles are the vertices of the Voronoi diagram (see red dots and red lines of Figure 32). Thus, VDR is the distribution of all regional areas of the mosaic Voronoi diagram and VDA is the distribution of all regional angles of the mosaic Voronoi diagram. CN is the distribution of the closest neighbour measured for each cell. The RI is computed as the average value of the CN distribution divided by its standard deviation, and exhibits a theoretical value of 1.91 for random distribution (Cook, 1996).

All these methods are tested using the same set of mosaics, each composed of 400 cells. Nine mosaic regularity conditions are generated with a random weight varying from 0.1 to 0.9 – 0.1 being a very regular mosaic and 0.9 a random point distribution. The script used for mosaics creation and methods analysis can be found on github

(https://github.com/JeandeMontigny/scripts/blob/master/mosaic_method.py). It is important to point out that the differences in mosaic regularity decrease as the random weight value used for mosaic generation increases. In order to minimise the effect of randomness, each regularity condition is repeated eight times, resulting in a total testing set of seventy-two mosaics.

From the eight mosaics of the same random weight value, the averaged cumulative density distribution is computed for DTS, VDR, VDA and CN, while the averaged index values is used for RI. This averaging is done for each of the random values used for mosaic creation. Figure 33 illustrates the computed average cumulative density for DTS (Figure 33A) and the average RI (Figure 33B) depending on the random weight value used for mosaic creation.

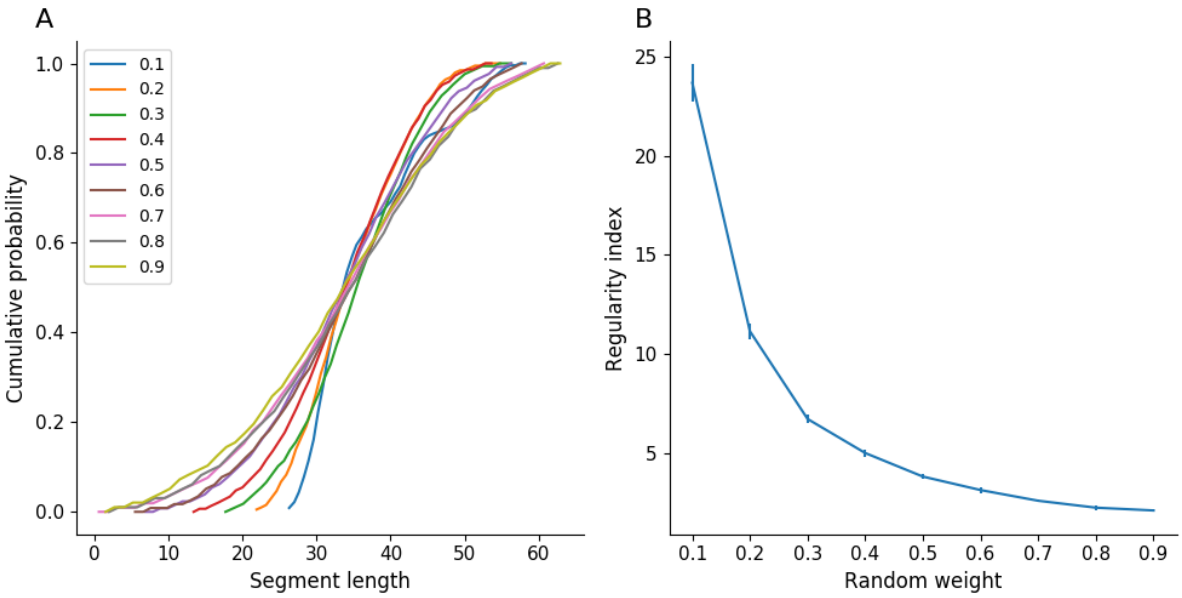

Figure 33: Two mosaic regularity measures, depending on random weight value used for mosaic creation, varying from 0.1 to 0.9. A: Delaunay triangulation segment length (DTS) cumulative density distribution. Each cumulative density is the average of eight different mosaics of the same random weight. **B:** Regularity index. Each point is the averaged RI value of eight mosaics of the same random weight. Error bars represent the standard deviation.

In order to investigate the strength of each method to discriminate differences between mosaics of distinct random weight, and hence, with different regularity, we compared mosaics of adjacent random weight (0.1 vs 0.2, 0.2 vs 0.3, etc.). A two-sample Kolmogorov-Smirnov statistic test is used to compare cumulative density probability for DTS, VDR, VDA and CN, while a T-test for two independent samples scores is used for RI.

All methods are able to discriminate regular mosaics from random distributions. However, few methods are able to discriminate fine differences in medium and low regularities, as shown in table 5. In more detail, the VDA is unable to capture any of the fine mosaic regularity changes, even for highly regular mosaics. The DTS is able to discriminate differences of mosaic regularity, but only for highly regular mosaics (0.1 to 0.4). On the contrary, no significant differences are noted for comparison of mosaics with a random weight higher than 0.4. The VDR and the CN are both able to discriminate between mosaics of high and medium regularities (0.1 to 0.7), but these measures are not sensitive enough to capture differences between mosaics of lower regularities. On the contrary, the RI is able to discriminate changes for all mosaic generation conditions, including fine differences in low regularities (0.8-0.9). RI also presents the benefit of offering a single score, facilitating mosaic comparisons and evolution through development. In addition, and as previously reported by Reese and Keeley (2015), the RI offers a scale-invariant measure of mosaic regularity and thus more direct evidence of any change in the mosaic spatial organisation during development. It is not only the absolute RI value that carries information, but also its evolution across development, related to the contribution of each mosaic developmental mechanism (CF, CD, CM). However, it should be pointed out that RI is sensitive to a low sampling rate (Cook, 1996), leading to important variability in RI score for low sample mosaics. Nonetheless, based on these results we decided to use the RI as the mosaic regularity measure in the following work.

	0.1 - 0.2	0.2 - 0.3	0.3 - 0.4	0.4 - 0.5	0.5 - 0.6	0.6 - 0.7	0.7 - 0.8	0.8 - 0.9
Delaunay segment length	**	**	*	.	.	.	.	.
Voronoi areas	***	***	***	***	***	**	.	.
Voronoi angles	.	.	.	.	.	.	.	.
Regularity index	***	***	***	***	***	***	***	*
Closest neighbour	***	***	***	***	**	**	.	.

Table 5: Comparison of mosaic regularity measure methods sensitivities. n = 8 for each mechanism. Asterisks indicate significant difference between the two considered mosaics (*** for p < 0.001; ** for p < 0.01; * for p < 0.05).

4.2 Results

4.2.1 Prior simulations

Prior simulations have been conducted in order to investigate the effect of tissue stretching on the RI, but also to build control situations of each mosaic formation

mechanism. By doing this, we are able to verify if each mechanism is intrinsically able to create a regular mosaic.

To investigate the impact of retinal stretching on RI, we built a simple prior simulation in which stretching is applied homogeneously from either one corner, or from the centre of the tissue. Unsurprisingly, we found that tissue stretching has no impact on cell regularity (for both conditions: $p < 0.001$, $n=8$ using a T-test for two independent samples).

To determine if each biological process that is potentially involved in mosaic formation (CF, CD and CM) is able to create mosaics by itself, we built non-agent based simulations, implementing optimised but non biologically realistic mechanisms. All mechanisms are ruled by a global supervisor, charged to determine cell differentiation, cell death (population death rate fixed at 65%) and cell migration. Mechanisms' implementation is available on github (https://github.com/JeandeMontigny/scripts/blob/master/non_AB_mechanisms.py).

Mosaics built using only non-agent based mechanisms have a RI of 3.14 (±0.08, n = 8) for CF, 5.83 (±0.4, n = 8) for death mechanism and 15.7 (±1.5, n = 8) for CM (Figure 34). All these RI values are significantly higher than random distribution, and can be considered of mid regularity (in the case of CF mechanism) to extremely regular (for the CM mechanism). These preliminary studies demonstrate that all three mechanisms are able to yield regular mosaics.

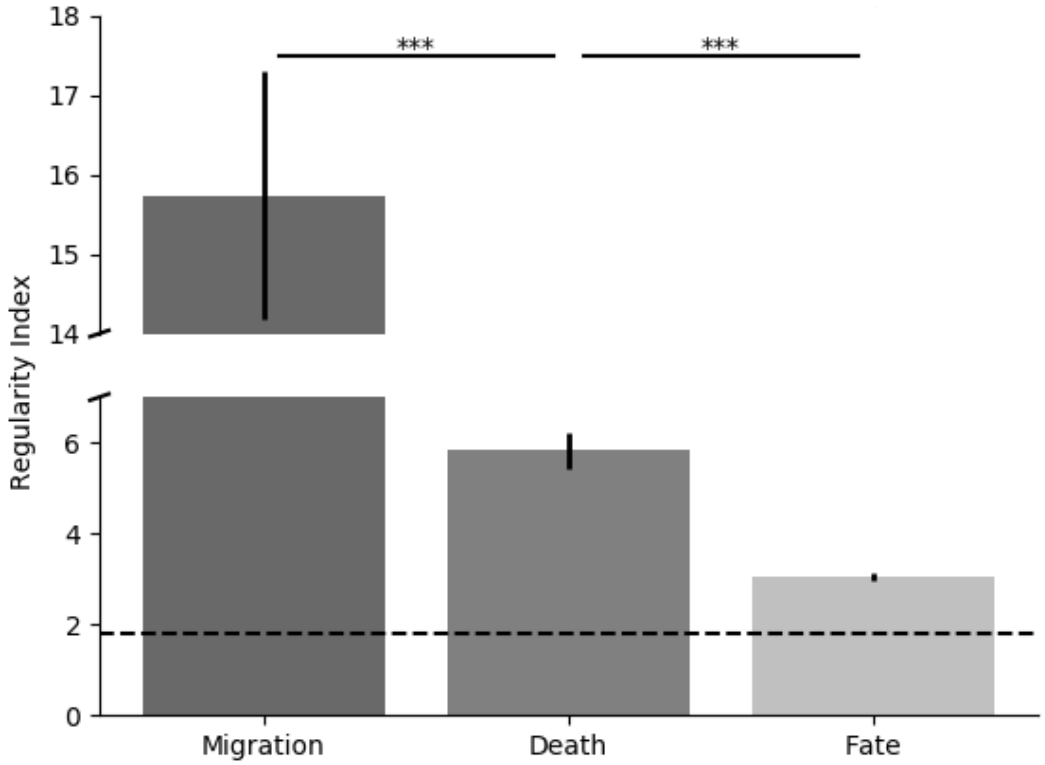

Figure 34: Non AB implementation of CM, CD and CF mosaic formation mechanisms. n = 8 for each mechanism, error bars represent the standard deviation; death rate has been fixed to 65%; y axis is broken to better display lower values; *** for $p < 0.001$ with an independent samples T-test.

4.2.2 Agent based modelling of mosaic development

Using the AB framework BioDynaMo, we investigated the three mechanisms potentially implicated in RGC mosaic formation during retinal development.

Thereby, we demonstrate that a realistic AB implementation of the CF mechanism is able to significantly increase the mosaic regularity compared to a random distribution ($p < 0.001$ with a T-test for two independent samples). Indeed, as shown in Figure 35A, the average RI values rapidly increase from random levels (between 1.8 and 2) until reaching a value of 2.42 (±0.09) at the end of the CF mechanism. However, such RI values cannot be considered as reflecting regular mosaics. Moreover, the CF mechanism alone cannot explain high RI scores observed for some RGC types (> 5). As shown by Figure 35B, no correlation can be established between cell density and RI values (correlation magnitude of 0.31), mosaics of high cell density reaching similar RI as seen in mosaics of low cell density, as illustrated by the blue and orange lines in Figure 35A.

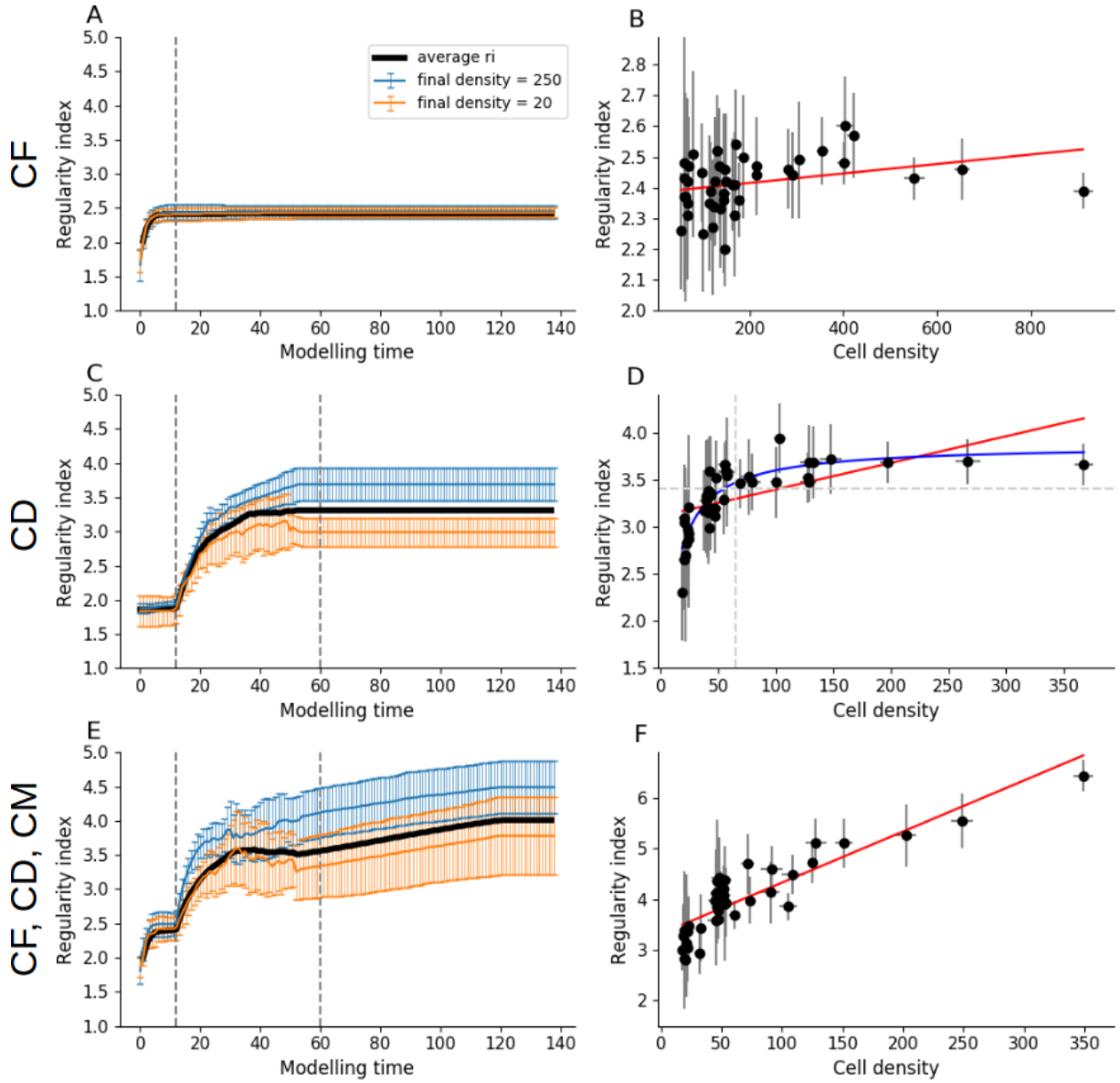

Figure 35: RGC mosaic formation modelling using an ABM approach. A,C,E: RI score evolution during simulation (x axis: 10 visualisation steps correspond to 1 developmental day in mouse). Average RI values for all RGC types are displayed in black while two populations of high and low densities (250 and 20 cells/mm^2 respectively) are displayed in blue and orange. The first vertical grey dashed line on the left indicates, if implemented, the end of the CF mechanism and if implemented, the beginning of the CD mechanism. Second grey dashed line indicates the end of the CD mechanism**. B,D,F:** Final RI score depending on cell density at the final step of the simulation. Error bars represent standard deviations for average RIs and densities. Red lines represent linear regressions (correlation coefficient: r=0.31, r=0.58 and r=0.87 for B, D and F respectively). The blue line in D represents a non-linear regression (a*x / b+x), while the horizontal dashed line represents the RI value under which no cell type of density higher than 125 is observed. **A,B:** CF mechanism only. **C,D:** CD mechanism only. **E,F:** Combination of CF, CD and CM combination.

The CD mechanism is also able to significantly increase RI compared to a random distribution ($p<0.001$ with a T-test for two independent samples). As shown by Figure 35C, the average RI value increases from random to 3.31 (±0.33) at the end of CD.

This death rate amounts to around 65% when it reaches a steady state at the end of the simulation. As shown in Figure 36A, these death rate dynamics are very similar to rates observed *in-vitro*. Moreover, and unlike for the case of the CF mechanism, CD is able to generate mosaics of medium regularities (RI > 3).

Interestingly, and as shown by Figure 36B, the death rate measured *in-vitro* and selected for our simulations (grey vertical dashed line) is not the one generating the highest regularity. Indeed, the highest scores of RI are achieved for death rates between 5 and 30% of the RGC population, regardless of the initial density of the considered population. After 30% of cell death, RI decreases until it reaches a random distribution once 92% of cell death is achieved. This is observed in both high and low density conditions. However, strong differences between populations of high and low initial densities can be noted. As shown by Figure 36B, the high density population is able to generate more regular mosaics than the population of low density, both for their maximum value (RI > 9 and RI > 5, respectively) and at 65% of cell death (RI = 4.49 ±0.36 and RI = 3.61 ±0.59, respectively). In fact, a relation between cell density and the final regularity is observed when the death rate is set to 65%. Mosaics of low density exhibit on average low RI values, while mosaics of cell density higher than 65 cells/mm^2 (vertical dashed line of Figure 35D) exhibit a higher average RI score of 3.35 (horizontal dashed line of Figure 35D). This RI-density correlation does not appear to be linear (correlation magnitude of 0.58, linear regression is displayed as a red line in Figure 35D), but follows a non-linear function (a*x / b+x) that plateaus around a RI value of 3.7 (non-linear regression displayed as a blue line in Figure 35D, standard deviation errors on the parameters use for fitting = 0.045). Final average RI scores for the CD mechanism alone and a combination of the CF and CD mechanisms do not significantly differ (3.31 ±0.33 and 3.48 ±0.44 respectively, p = 0.76 with a T-test for two independent samples). However, coupling the CF and CD mechanisms has a positive impact on dense mosaics' regularity (for cell densities higher than 125 cells/mm^2). Thereby, the shapes of non-linear regression between cell density and RI are similar for these two conditions, except for the higher RI value plateau in the case of the CF and CD combination, which amounts to approximately 4.1 (standard deviation errors on the parameters use for fitting = 0.08).

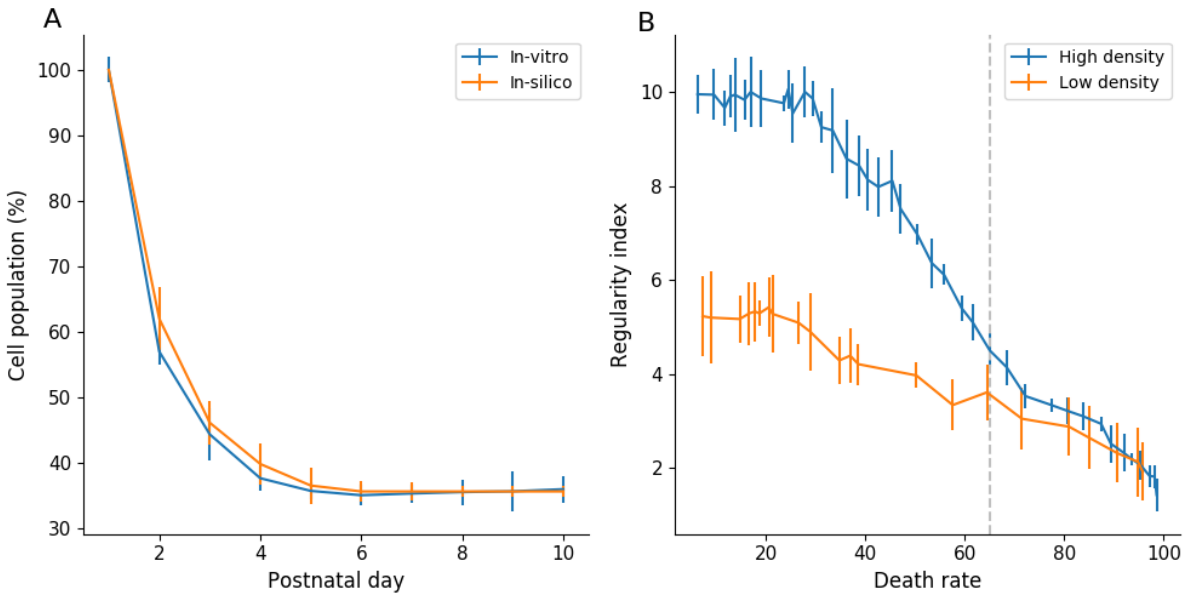

Figure 36: CD mechanism impact on RGC population. A: RGC population measured *in-vitro* (blue) and in simulations (orange). *In-vitro* population at day 1 is an estimation based on a final CD of 65%. Error bars represent standard deviation. **B:** RI score depending on final CD rate in a simulation implementing only the CD mechanism, for selected RGC populations of high density (blue curve, initial density = 571 cells/mm^2) and low density (orange curve, initial density = 114 cells/mm^2). Error bars represent standard deviation.

A combination of all three mechanisms (CF, CD and CM) is also able to generate mosaics significantly more regular than random distributions ($p<0.001$ with a T-test for two independent samples). Different steps of a simulation are illustrated by Figure 37. As shown by Figure 35E, a first RI increase is observed, corresponding to the effect of CF. After the CD and CM mechanisms are triggered (first dashed line), an important second increase is to be noted until the RI value stagnates toward the end of CD (simulation day 4 to 5.5). Finally, a third RI increase is observed after CD is over (second dashed line) due to the CM mechanism, leading to an average RI score of 4.01 (±0.75) at the end of the simulation. Unlike any other mechanism alone, and thanks to tangential migration, this simulation condition is able to generate highly regular mosaics (RI > 5). Moreover, a strong correlation appears between cell density and RI values (linear correlation magnitude of 0.87) as shown by Figure 35F. Thereby, only RGC types exhibiting a cell density higher than 125 cell/mm^2 are able to generate mosaics with a RI value higher than 5. Thus, as illustrated by the blue and orange lines in Figure 35E, significant differences emerge between mosaics of high and low density. No significant differences are seen between simulations of CD and CM combination and simulations of CF, CD and CM combination. Although tangential cell migration alone is able to yield very regular mosaics, it is important to note that the CF and CD mechanism cannot be neglected. Their implementations are

essential to obtain simulations as realistic and exhaustive as possible, as these two mechanisms have been reported to take place during retinal development.

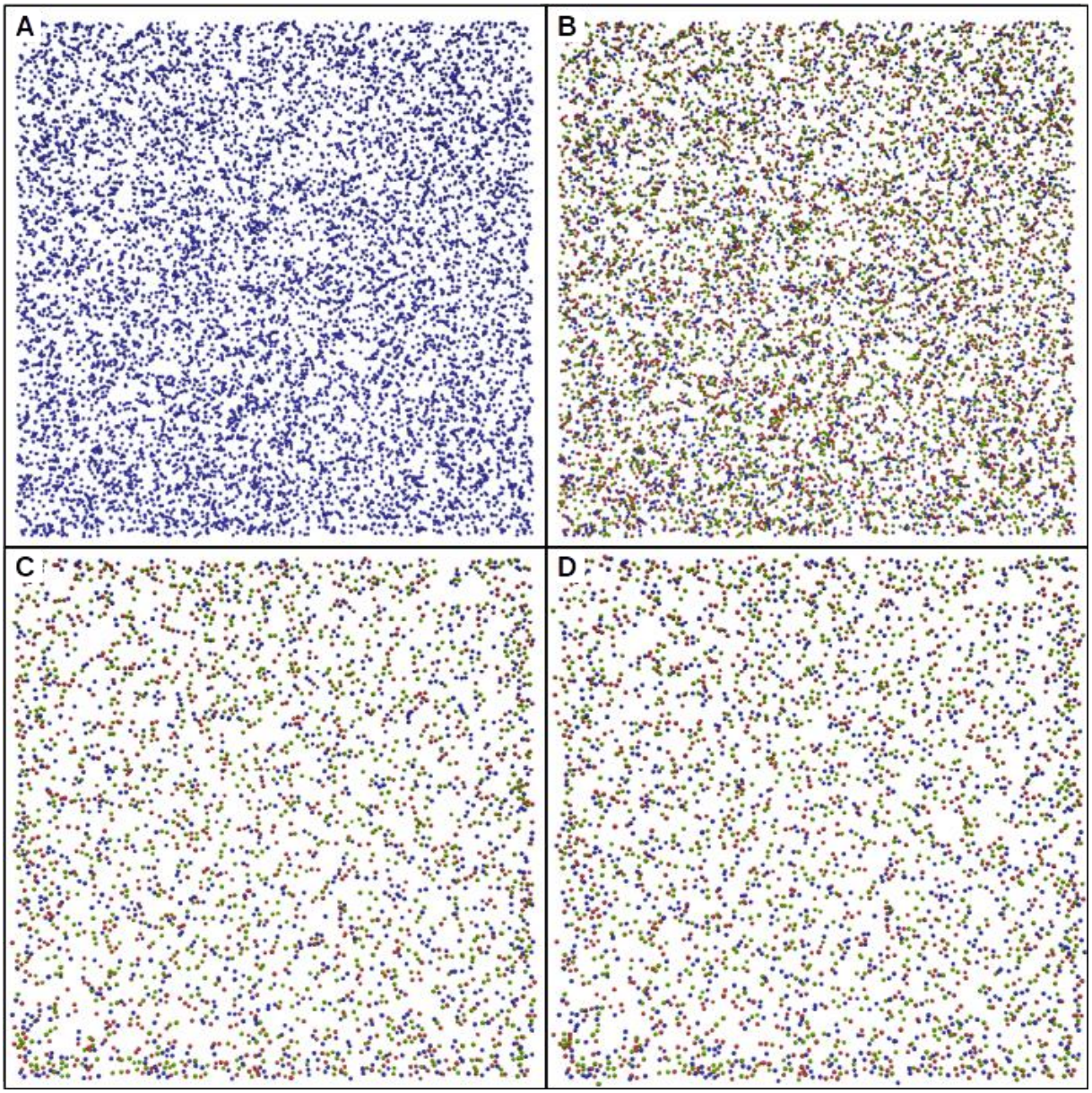

Figure 37: Time laps of mosaic formation, implementing the three mechanisms (CF, CD and CM) using BioDynaMo. A: Simulation at step 0. All cells are undifferentiated and represented in blue. **B,C,D:** On cells are represented in green, Off cells in red and On-Off cells in blue**. B:** Simulation state at the end of cell differentiation, at step 180. Average RI = 2.41. **C:** Simulation state at the end of cell death (65% of death rate), step 1000. Average RI = 3.42. **D:** State at the end of the simulation, step 2240. Average RI = 3.99.

When all mechanisms are implemented, surviving cells migrate tangentially with an average of 8.72 µm (±0.11, n = 8). This average travelled distance is in accordance with *in-vivo* measures, reporting RGCs and SACs tangential migration not beyond 30µm (Nguyen-Ba-Charvet and Chédotal, 2014). Important disparities between cells are to be noted, as shown in Figure 38A, with an average migration distance

standard deviation of 9.44 (±0.18). No correlation between final RI and migration distance can be seen. Likewise, no correlation appears between final density and migration distance if the whole population is considered. However, if only populations with a final density higher than 100 cells/mm^2 are considered, a strong correlation can be observed (correlation coefficient r = 0.92, see Figure 38B red line). Hence, the denser the cell type the larger the distance cells migrate.

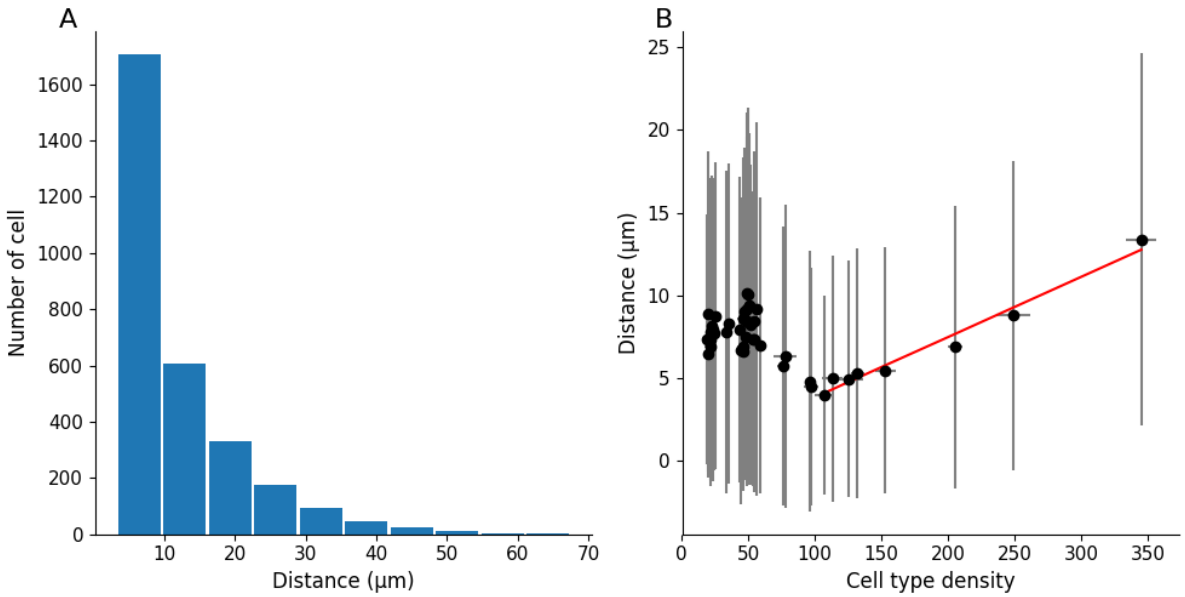

Figure 38: Migration distance measured in simulations implementing CF, CD and CM. A: Migration distance distribution. **B:** Relation between cell type density and migrating distance. The red line represents the correlation between migration distance and cell type density for densities higher than 100 cells/mm^2 (correlation coefficient r=0.92).

4.2.3 Altered RGC development: the Pax6-αCre driven Dicer-1 model

Successfully simulating a single healthy developmental condition is usually not enough to validate a computational model. To support our model validation, we conducted a simulation of an abnormal developmental condition, the Dicer-1 deletion model.

The deletion of Dicer-1 in retinal progenitor cells leads to the death of RGCs. By using a Pax6-αCre line, it is possible to target specifically progenitors cells of distal areas of nasal and temporal retina, inducing RGC death for all cells in these areas (Maiorano and Hindges 2013). In order to reproduce this model, cells are created similarly to previous simulations (section 4.2.3), and implement CF and CM mechanisms. To recreate the retinal degeneration pattern induced by the Dicer-1 deletion (ellipsoid), cells are removed from the simulation if their coordinates (x, y)

follow the inequation $\frac{(x-c_x)^2}{(L\times 0.3)^2}+\frac{(y-c_y)^2}{L^2}>0.5$, where c_x and c_y are the x and y coordinates of the simulation space centre and where L is the length of the square formed by the initial population creation. This cell death represents on average 61.8% (±0.3, n=8) of the initial population, and the resulting surviving cells follow an ellipse pattern (see Figure 38A). This amount and pattern of cell death is similar to what is observed in the biological model, where around 40% of cells remain alive (Georgi and Reh 2010) and form an ellipse at the centre of the retina. Because of this initial cell death, and in order to follow the Dicer-1 deletion model, CD mechanism is not implemented here. The model is then simulated similarly to previous simulations (section 4.2.3).

At the end of the simulation, an expansion toward the periphery of the ellipse formed by surviving cells is observed, increasing its width from 421.98µm (±1.0, n = 8) to 540.45µm (±8.74, n = 8). This represents an expansion of 28.1% (±1.87, n = 8) as show by Figure 39. Moreover, a significant difference of average migratory distance ($p < 0.001$ with a T-test for two independent samples) is observed, with an increase from 8.72µm (±0.11, n = 8) for previous simulations (section 4.2.3), to 39.0µm (±0.77, n = 8) for simulation implementing the Dicer-1 deletion model. In addition, and contrary to previous simulations (see Figure 38B), no significant correlation is found between migration distance and cell type density. No significant impact of cell-fate on the average migratory distance is to be noted ($p > 0.05$ with a T-test for two independent samples). Nonetheless, the expansion observed in our simulations is less pronounced to what is observed in the biological *in-vivo* model. Indeed, in the Dicer-1 deletion driven by the Pax6-αCre model, the expansion of the remaining cells results in a RGC retinal coverage of 8.6mm^2 (±0.2, n = 8) versus 12.1mm^2 (±0.3, n = 8) for wild-type animals (Maiorano and Hindges 2013). This represents a final coverage of 71% of the total retinal surface while this final coverage represents only about 54% in our simulation.

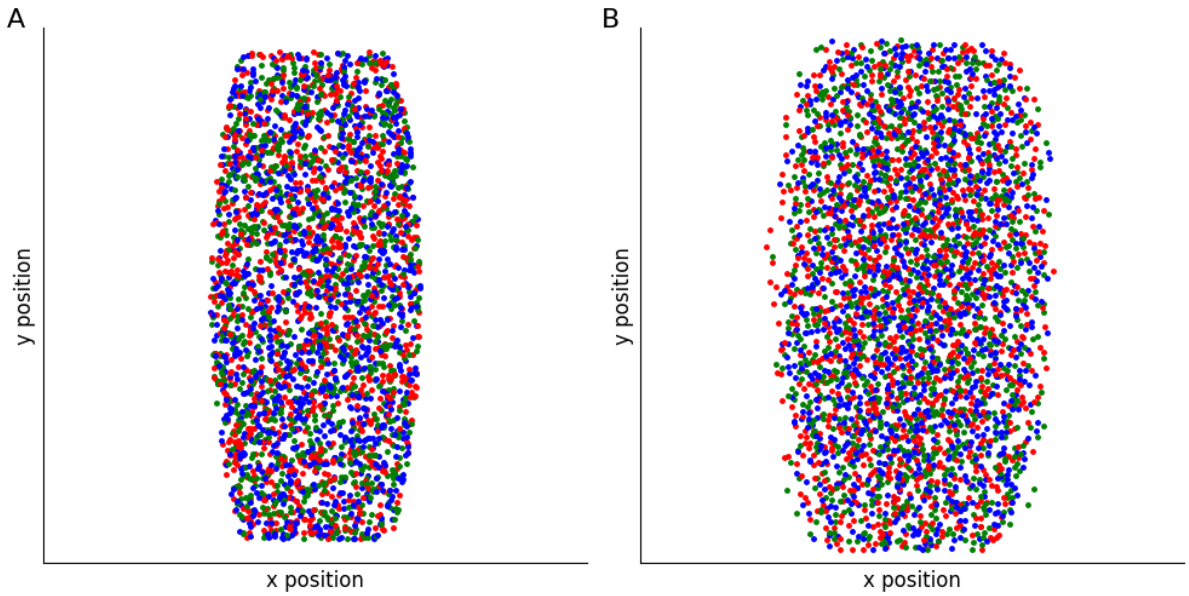

Figure 39: Simulation of Dicer-1 deletion Model. A: Simulation at step 0, after cell death following the Dicer-1 deletion driven by Pax6-αCre model and before the beginning of mosaic formation. **B:** Simulation at the end of mosaic development. On cells are represented in green, Off cells in red and On-Off cells in blue.

Differences in mosaic formation also appear, with very high regularity being achieved (RI > 7), due to the high cell density that results from the absence of cell death. For this reason, and contrary to previous simulations (see Figure 35F), no significant linear correlation between RI and cell density develops. Indeed, RI value plateaus around 7 when cell density is higher than 100 cells/mm^2 thus following a covariance similar to the one observed for mosaic formation without CM (see Figure 35D).

It is important to point out that these results were obtained without changing any simulation parameters (chemical substance sensibility, migration speed, etc.). This is an important condition to use this abnormal developmental condition as a step toward the validation of our mosaic formation model. In principle, modifying some cell parameters could increase the expansion of the ellipse formed by surviving cells, and so improve the agreement with experimental results. This however, can only be done based on biological evidence, in order to preserve the model realism.

4.2.4 SAC mosaics formation

Our simulations for RGC mosaics development can also be applied to simulate SAC mosaics formation. In addition of SAC mosaics formation study, successfully applying our mosaic creation model to another cell type would strengthen our model validation.

The SAC population is divided between two different cellular layers, the GCL and the INL, forming two separated populations. These two SACs populations exhibit regular pattern organisation (see Figure 9B in section 2.2.1), and the two mosaics formed by the GCL and INL populations tend not to overlap (see Figure 10 in section 2.2.1). Thus, a SAC in the GCL has few chances to be at the same location as a SAC in the INL.

In the simulations implemented here, SAC mosaics are formed before GCL/INL separation. Indeed, the SAC mosaics RIs measured in mouse pup do not vary between P3-4 (shortly after GCL and INL separation) and the end of retinal development (see Figure 9 in section 2.2.1). This could indicate that mosaics are already formed and do not improve their regularity once SACs have migrated to their respective cellular layer. Mosaic formation is achieved using locally diffused chemical cues triggering homotypic avoidance (tangential migration mechanism). Once mosaics are formed, the two populations migrate to their respective layers. Two different developmental conditions have been implemented, using either one common or two separated (one for GCL population, one for INL population) chemical substances for mosaics formation. Concentration thresholds triggering cellular migration have been set to 3.18 and 2.66 respectively. Importantly, this concentration threshold is identical for the GCL and INL populations. Parameters have been set such that the mosaic RIs match the measured RIs in mouse SACs mosaics.

Interestingly, using an identical concentration threshold for CM, the GCL population exhibits less regular mosaics than the INL population at the end of the simulation, in both developmental conditions (RI of 3.57±0.12 and 4.11±0.12 respectively when one substance is used, RI of 3.36±0.07 and 4.37±0.15 respectively when two substances are used, n=8 for each group, $p<0.0001$ with T-tests for two independent samples). This mosaic regularity disparity is in accordance with observations in mouse (see Figure 9B in section 2.2.1) and can be explained in our simulations by the cell density difference between these two layers.

However, an important difference emerges between the two conditions concerning the exclusion factor of the two SACs populations. Indeed, if one common developmental cue is used, GCL and INL mosaics exclude each other with a calculated exclusion factor of 0.71 (±0.01, n=8), similar to what has been measured *in-vitro* (0.74±0.09, n=5, see Figure 10 in section 2.2.1). This indicates that the GCL and INL populations' mosaics tend not to overlap. However, if two distinct

developmental cues are used, the exclusion factor is measured to a lower value of 0.31 (±0.1, n=8), denoting independent mosaics that tend to overlap more. In this second condition, the measured exclusion factor is significantly lower than the one observed in mouse ($p<0.0001$ using a T-test for two independent samples, n=8 and 5 respectively). Thus, only the first condition, where one common developmental cue is used for the two SAC populations, is able to reproduce the exclusion factor observed *in-vitro*.

4.2.5 Dendritic development

Using BioDynaMo, we investigated the requirement to grow realistic dendritic arbours. We demonstrate here that AB growth rules based on simple chemical developmental cues are enough to obtain complex, varied and realistic morphologies. Simulated dendritic arbours are illustrated in Figure 40A. Only six cells (two On, two Off and two On-Off) are displayed to increase the figure readability. As shown in Figure 40B, two dendritic lamination levels are formed. Off cell dendrites (red) laminate only in the upper layer while On cells dendrites (white) laminate exclusively in the lower layer. On-Off cells for their part (blue) extend dendrites in both lamination levels of the IPL. This recapitulates the main morphological difference between these three distinct RGC types.

Number of dendritic roots

The attribution of dendritic root number has been determined in accordance with the observed number of dendritic roots for On, Off and On-Off cells of the Sümbül database (Sümbül et al., 2014). Indeed, while the whole RGC population exhibits an average number of dendritic roots of 4.02 (± 1.14) some disparities emerge if sub-populations are considered. Indeed, the On population exhibits a significantly higher number of roots (4.99 ± 1.41), similar to the On-Off population (4.56 ± 1.14) while the Off population exhibits a number of roots close to the average value (4.08 ± 0.93). Thus, simulated RGCs adopt root numbers in accordance with these measured values, more precisely 4.91 (± 1.21) for the On population, 4.51 (± 1.12) for the On-Off population and 3.99 (± 0.88) for the Off population. No significant differences appear between simulated and real values for each RGC population ($p>0.1$ with a T-test for two independent samples).

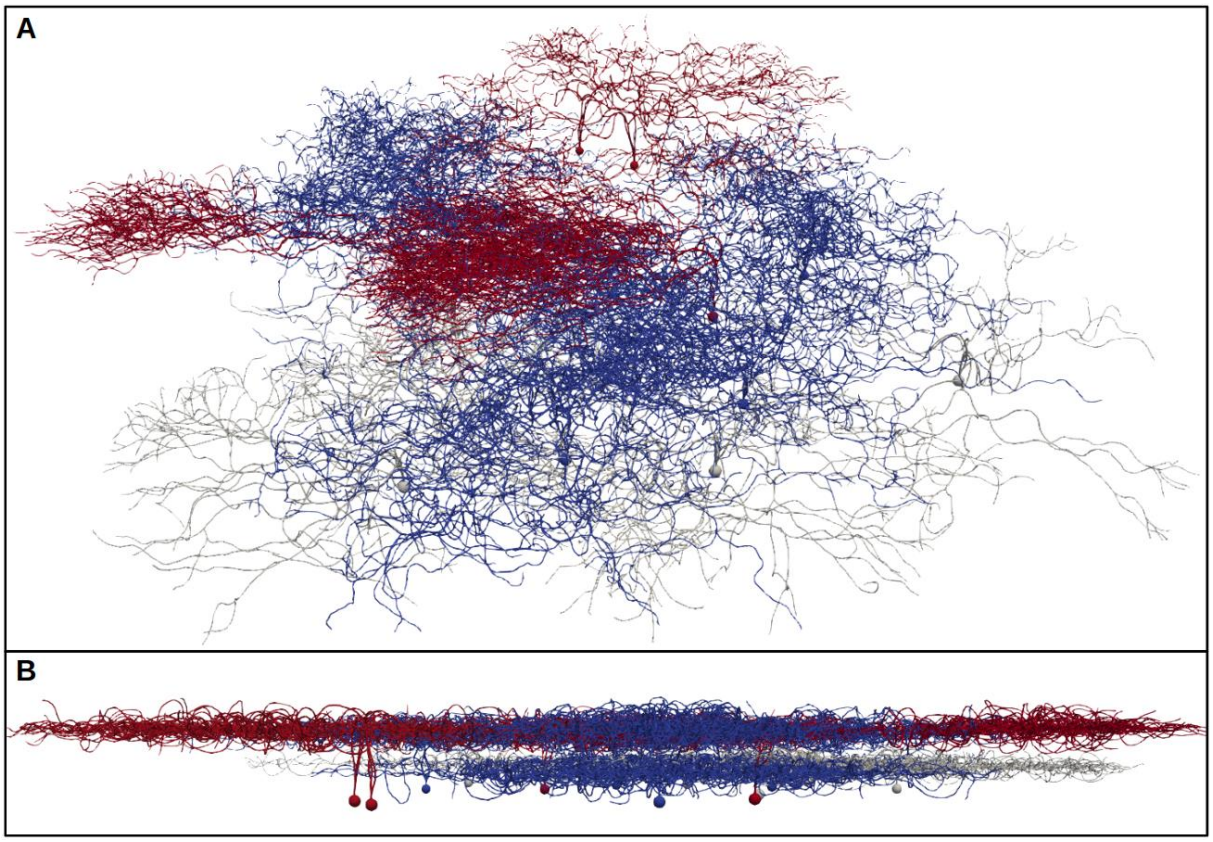

Figure 40: Illustration of simulated dendritic arbours. For clarity purpose, only six cells are displayed, two On, two Off and two On-Off. On cells are represented in grey, Off cells in red and On-Off cells in blue. **A:** Three quarter view from the top. **B:** view from the side.

Two simulation conditions have been studied, using either three generic growth rules (On, Off, On-Off) or using thirteen growth rules.

In the first condition, growth rules have been defined such as the morphologies are as close as possible to the measured morphologies of the Sümbül database. It is important to point out that despite the limited number of growth rules, dendritic competition for space depends on the considered cell type and not on the implemented growth behaviour (On, Off, On-Off). Thus, these dendritic interactions depend on the 43 types used to form RGC mosaics, not the 3 dendritic groups formed by the Implemented growth rules. For example, two On cells will only compete for dendritic space if they are of the same RGC type (for instance M2), and not because they both follow an On growth behaviour. This also applies to the second condition, where thirteen different growth rules are used.

In the second condition, the attribution of specific growth rules to sub-populations (for instance On-Off DSGC or J-RGC) has been decided based on the available morphological description of that RGC population in the literature, and morphological

measures of specific populations within the Sümbül database. For instance, J-RGC are described as cells with a strongly asymmetric dendritic arbour but a large diameter. Using these information, and by looking at the classification established in Sümbül et al., 2014, it has been possible to extract the J-RGC population from the Sümbül database and thus, to extract key morphological features of this population. These key features have then been used to determine the growth rule for the simulated J-RGC population, using a heuristic methodology to find parameter values. Likewise, mini-J-RGC and midi-J-RGC are described as strongly non symmetric, similarly to J-RGC, but of smaller diameter to J-RGC (Sanes and Masland 2015a). This principle applies for RGC sub-populations when morphological descriptions are available. Otherwise, a generic growth rule has been established for each On, Off and On-Off RGC population, in accordance the distributions of their morphological measures. In particular, these generic growth rules have been used to simulate dendritic growth of populations accounting for small RGC populations that remain to be discovered and characterised. Parameters have also been tuned using a heuristic approach.

Modelling dendritic arbour growth using only three different rules cannot recapitulate the morphological diversity observed in real RGC dendritic arbours. Indeed, no RGC group of morphological characteristics far from the average are represented (see Figure 41). In more detail, significant differences in arbour diameter distribution are observed between simulated RGC and empirical RGC. That is true for the whole population ($p=0.008$) or if On, Off and On-Off populations are considered separately ($p=0.0023$, $p=0.012$, $p=0.026$ respectively, using a Mann–Whitney U test for two independent samples). Similarly, significant differences are noted concerning the anisometry score distribution, for both the whole population ($p<0.001$), or if On, Off and On-Off populations are considered separately ($p<0.001$, $p=0.021$, $p=0.048$ respectively, using a Mann–Whitney U test for two independent samples). Finally, concerning the branching point number, significant differences emerge but only for the whole population ($p=0.011$) and the Off population ($p < 0.001$ using a Mann–Whitney U test for two independent samples).

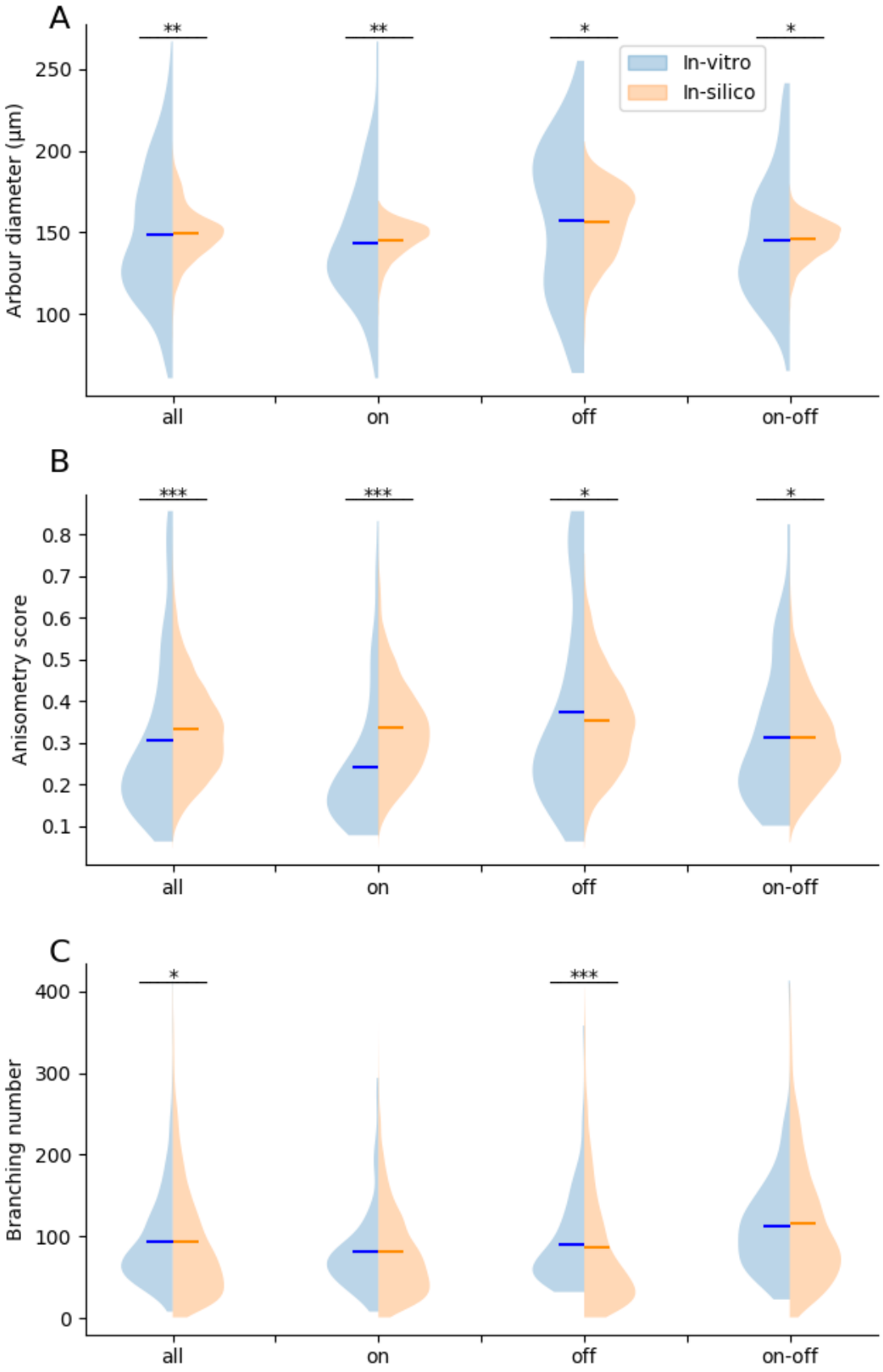

Figure 41: Dendritic arbour characteristics comparison when three growth rules are implemented. A: arbour diameter. **B:** anisometry score. **C:** number of branching point. (*** for p < 0.001; ** for p < 0.01; * for p < 0.05). n=364 for *in-vitro*, n=12000 for simulations.

Dendritic arbours simulated following only three different growth rules exhibit highly homogeneous diameters, compared with arbours diameters measured in Sümbül. Indeed, few to none simulated cells exhibit small (smaller than 120) or large (higher than 200) dendritic arbours (see Figure 41A). In addition, the anisometry score distribution of simulated cells does not reflect the variability observed in anisometry score of the Sümbül database. This is particularly true for the high anisometry observed in Off cells (anisometry score higher than 0.6, see Figure 41B). Some cells with abnormal dendritic arbour characteristics are still generated when using only three growth rules, but their number is negligible, and they do not present homogeneity in their phenotype. For these reasons, they cannot be considered a group or a population.

On the contrary, modelling dendritic development using numerous growth rules, especially for RGC known to exhibit a specific dendritic arbour (such as J-RGC or LED), allows the emergence of populations with morphological properties far from the average RGC population, as it is observed in real RGC populations (see Figure 42).

Increasing the number of developmental rules (thirteen instead of three) increased the morphological diversity of our simulated neurons. By consequence, no significant differences are seen concerning dendritic arbour size (diameter) distributions (see Figure 42A), both for the total population and for On, Off and On-Off populations separately ($p > 0.1$ using a Mann–Whitney U test for two independent samples). However, there are significant differences concerning the anisometry score distribution and branching points number distributions between our simulated RGC and the Sümbül database. In the case of the Off population, the implemented number of J-RGC, mini-J-RGC and midi-J-RGC and their very high asymmetry explains this observed anisometry score difference with the *in-vitro* RGC population ($p<0.001$ using a Mann–Whitney U test for two independent samples). Indeed, we have chosen here to follow the cell densities observed and documented by (Sanes and Masland 2015), reporting cell densities of approximatively 200, 350 and 80 cells per mm^2 for J-RGC, mini-J-RGC and midi-J-RGC respectively. Such high densities of non-symmetric cells are not found in the Sümbül database. Moreover, only few cells of small diameter and very high anisometry score (mini-J-RGC and midi-J-RGC) are represented in the experimental RGC population. Of course, this anisometry difference for the Off population (see Figure 42B) is transcribed in the overall

population, explaining the observed significant difference between our simulated cells and the Sümbül database ($p < 0.001$ using a Mann–Whitney U test for two independent samples) as shown in Figure 42B (whole population). This under-sampling of specific RGC types also explains the significant difference in branching number for Off cells between the empirical and simulated populations ($p < 0.001$ using a Mann–Whitney U test for two independent samples) as shown in Figure 42C (Off population). Indeed, as mini-J-RGC and midi-J-RGC exhibit small arbour trees, their branching number is mechanically small as well. As we follow the cell density reported in the literature for these cell types (see sections 1.4.2, 4.1.1 and 4.1.2), it increases the number of cells with few branching points in our simulations, thus diverging from the RGC dataset of Sümbül. Likewise, this Off population branching number difference is found in the global RGC population and explains the significant difference from the Sümbül database ($p < 0.001$ using a Mann–Whitney U test for two independent samples) as shown in Figure 41C (whole population). The significant difference of anisometry score distribution for the On population ($p < 0.001$ using a Mann–Whitney U test for two independent samples, see figure 42B) results from an inability in our simulations to reproduce the very low anisometry score of this population.

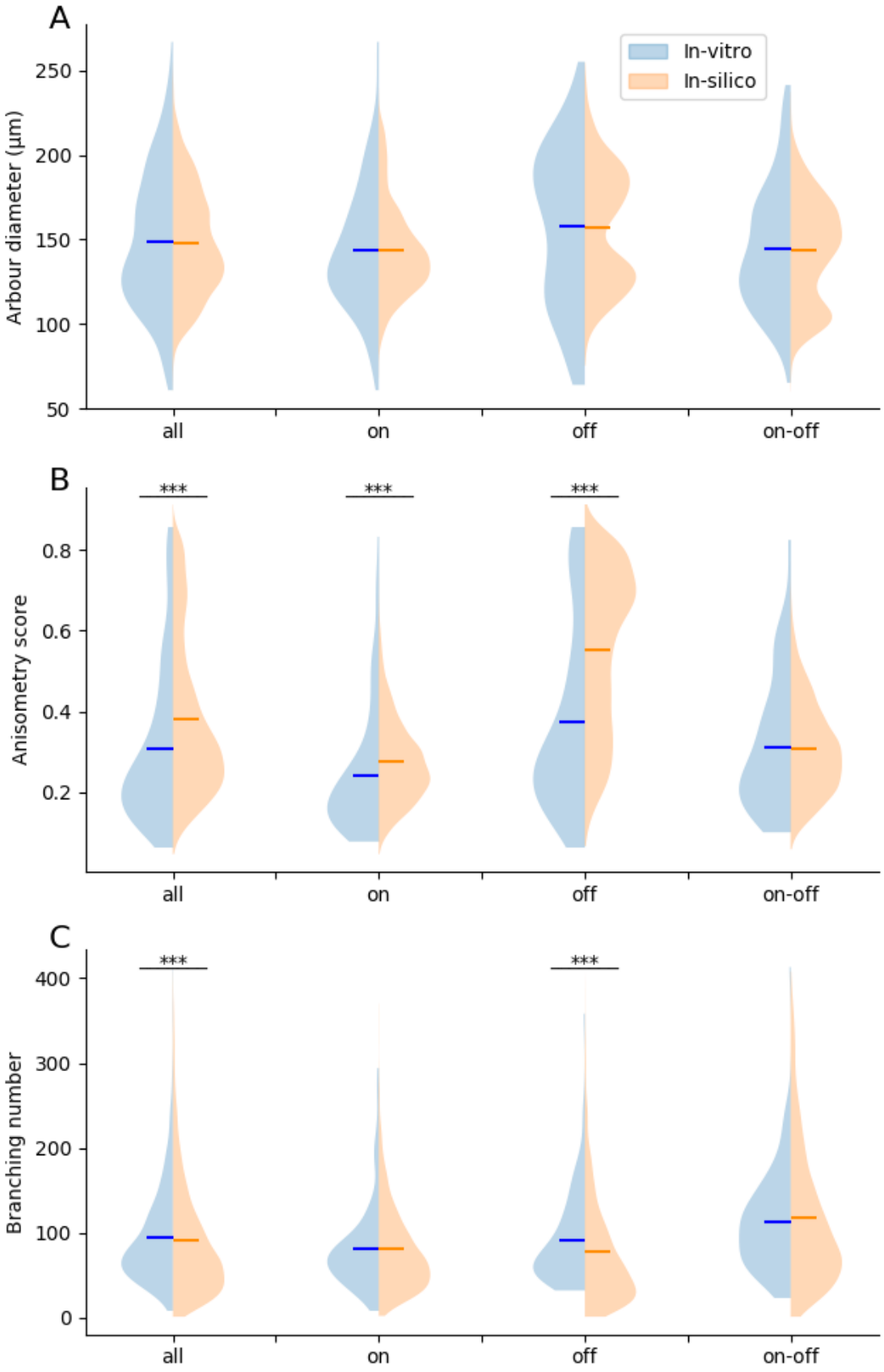

Figure 42: Dendritic arbour characteristics comparison when thirteen growth rules are implemented. A: arbour diameter. **B:** anisometry score. **C:** number of branching point. (*** for $p < 0.001$; ** for $p < 0.01$; * for $p < 0.05$). n=364 for *in-vitro*, n=12000 for simulations.

Chapter 5. Discussion

All computational simulations have to be built upon biological data in order to offer relevant insight of a scientific problem. For this reason, information about retinal development has been gathered using *in-vitro* experimental observations. Thus, we followed RGCs characteristics through development using RBPMS staining in neonatal mouse retinas. This notably allowed us to measure death dynamic from P2 to P11, and to confirm that our measures are in agreement with the literature, reporting RGC death during the first 11 days of life with a peak between P2-4 (Braunger, Demmer, and Tamm 2014). By taking into account retinal surface expansion during normal development, our measured total RGC death rate is low compared to the study considering simply RGCs density over time.

Biological information gathered from our *in-vitro* experiment and from the literature have been used to build realistic simulations of retinal cells self-organisation. This notably includes the number of RGCs types incorporated in our simulations. Indeed, the numerical distribution of On, Off and On-Off RGCs is known to vary depending on species. For instance, midget cells are numerous in primates and cats (representing the main vehicle for acute vision), but not in mouse where these cells (βRGC) are almost not represented. Thus, for our simulations, we chose the number of RGCs types and their numerical distribution based on a review from the literature (Sanes and Masland 2015a; Reese and Keeley 2015; Baden et al. 2016). Notably, Sanes and Masland 2015 speculated that classified and well-described RGC types represent only about 60% of the total RGC population, corresponding to around 1740 cells/mm^2 from the total 3000 cells/mm^2 observed in the mouse retina. In addition, it is important to note that from these known and classified RGC populations, only 12.4% are On type (216 cells/mm^2 out of 1740 cells/mm^2, divided in 7 types) while 44.4% are Off types (773 cells/mm^2 out of 1740 cells/mm^2, divided in 6 types) and 43.1% are On-Off (750 cells/mm^2 out of 1740 cells/mm^2, divided in 6 types) types. As On, Off and On-Off are evenly represented (30% to 35% each), a great number of On cells still needs to be discovered in order to reach the theoretical percentage of On RGC in the total RGC population (30% to 35%). Thus, we can hypothesize that either: 1. A couple of numerous and high density On types have not been discovered and characterised yet. 2. There are more On than Off or On-Off types.

The first hypothesis appears unlikely as RGCs are widely studied, especially with the emergence of large-scale and high density MEA recordings, but also using morphological and molecular characterisations. Thus, there is only a low probability

that the existence of several dense On RGC types (representing the majority of the On population, and so being the most common On type) has not been captured by at least one of these techniques. The second hypothesis for its part appears to be coherent as mouse, similarly to other nocturnal animals, have rod-dominated vision. Indeed, rods are known to project their dendrites and to establish synaptic connections only to On bipolar cells, that in turn establish synaptic connections to On RGCs. In order to extract as many features as possible from a visual scene using mainly rod vision, a great diversity of specialized RGCs can be justified. The hypothesis of a great diversity of low density On types is also in agreement with Masland et al., 2015, speculating that around 30 low density RGC types exist — representing about 1% of the population each but about 95% of the total population in total — and are yet to be discovered. Baden et al., 2016 also estimate the total number of RGC types to be over 40, supporting the hypothesis of numerous low density RGC types, including On types.

As it is still possible that one On type of mid density has not been discovered, we chose to allow the possibility for this hypothesis, in addition to adding multiple low density On RGC. Thus, one On RGC type with the density of 150cells/mm^2 has been integrated. Choice and implementation of these speculated On RGC types has been done using a Poisson law (high probability of low density population, low probability of high density population). As respectively 25.7% and 25% of Off and On-Off RGCs from the total RGC population have been characterised (with some types exhibiting high density, rising up to 350 cell/mm^2), we assumed that only low density Off and On-Off RGC are still to be discovered. For these reasons, only 6 types are added for Off and On-Off populations, while 16 On types are added. The chosen numbers (6, 6 and 12 respectively) allow the average densities of the added supplementary types to be similar for On, Off and On-Off RGC, with the exception to one mid density On added type. Thereby, a total of 43 RGC types are implemented in our mosaic development model.

Resulting simulations allowed us to investigate the requirements for RGCs mosaics' formation through development, and the specific impact of each mosaic formation mechanism (CF, CD and CM).

5.1 Mosaic formation

CF implication on RGC mosaics’ regularity is particularly difficult to study *in-vitro* or *in-vivo*. Yet, thanks to RGCs progenitors' studies, no evidence has been found for

RGC type-specific progenitors (Sweeney et al. 2017). This means that types of RGCs are probably not pre-determined early on and so are likely to depend on extrinsic factors, such as the presence of chemical cues (Livesey and Cepko 2001). Thereby, it allows for the contribution of a mechanism such as CF for RGC type differentiation, and its potential implication on mosaic formation. However, the first result arising from our simulations is the impossibility to create highly regular mosaics by using only the CF mechanism (RI > 2.5). Likewise, CF mechanism does not significantly increase the potentiality of other mechanisms (CD and CM) neither. This suggests that RGC types are unlikely to be dictated by cell body mosaics but instead may be dictated by intrinsic factors (that are still to be discovered), functional determination (dictated by the input it receives from other cells, or in order to establish a functional visual pathway), or a combination of intrinsic factors interacting with extrinsic factors.

In our simulations, the CD mechanism (alone, or in combination with the CF mechanism) is able to create regular mosaics (RI > 3.5) with a death rate of 65%. As this mechanism is based on a locally diffused chemical substance, homotypic cellular spacing (and therefore cell type initial density) has an important impact on CD mechanism. For this reason, only populations with an initial cell density higher than 180 cells/mm^2 exhibit regular mosaics. Importantly, our CD implementation is able to match measured RGC death dynamic during development, thus strengthening its plausibility. It should be pointed out that with the implemented CD mechanism, the concentration threshold triggering CD varies depending on the RGC type initial density. Indeed, a dense sub-population exhibits higher chemical cue concentration compared to a low density one, due to the higher number of cells secreting the chemical substance, but also by their closer proximity. With an identical threshold triggering CD, a high density sub-population would exhibit higher death rate than a low density sub-population. Thus, this CD threshold has to be set depending on the RGC type initial density in order to reach around 65% of death rate for each RGC population. Another mechanism allowing the triggering of CD by an identical concentration threshold value for all RGC types is also possible, but mechanically leads to RGC populations of low density to express only a negligible death rate. Indeed, a strong correlation between the initial cell density and the final death rate emerges, almost all the dying cells belonging to RGC types of high cell density. This also implies that at the time of cell birth, and after cell differentiation, a couple of RGC types represent almost the entire RGC population. To this date, it is unknown if the RGC death rate observed during development occurs asymmetrically between RGC

types, meaning that a few (very dense) RGC types die massively while the population of most (low density) RGC types do not undergo apoptosis. Experimental investigation could elucidate this possibility. It does, however, seem unlikely that only a minor portion of RGC types account for the majority of all the measured cell death. In both cases, it is important to point out that CD probably serves additional purposes in the retinal maturation process, and is not only geared towards mosaic creation. Indeed, some cell types which do exhibit mosaic regularity do not undergo any significant levels of CD (such as horizontal cells or photoreceptors). In fact, as demonstrated here, the maximum positive impact of CD upon RI is reached for a death rate between 5 and 30%. Beyond this death rate, cell death appears to have a negative impact on mosaic regularity, with RI decreasing to lower values when more cells disappear. This implies that even if CD can be involved in mosaic formation at early stages, cell death at levels above 30% is likely to be driven by other mechanisms and for another purpose than mosaic regularity. By removing cells that have established non-coherent connections, CD could be implicated in refining retinal functional connectivity and activity. Axonal miss targeting could be a potential mechanism triggering RGC death during normal development.

Finally, CM appears to be the only mechanism able to explain the formation of highly regular mosaics (RI > 5). As for the CD mechanism, the efficacy of the CM mechanism is dependent on cell density as it is based on local interactions. The shorter homotypic cellular distances are, the more they can sense and repulse each other. Thereby, a strong correlation emerges between RGC type populations densities and the regularity of their mosaics. Therefore, we propose here that all RGC types do not form mosaics. Only high density RGC types can form mosaics of high regularity, while low density RGC types can not form regular mosaics. It would be technically complex but very informative to verify this assumption *in-vitro*. To this date, no experimental studies tried to answer this question.

We show here that high mosaic regularity can be achieved with limited migration distance (8.72µm ±0.11 in average, n = 8). This average migration distance is in accordance with *in-vivo* measures, reporting RGCs and SACs tangential migration not beyond 30µm (Nguyen-Ba-Charvet and Chédotal, 2014). It is however notably lower than the average migration distance, measured at around 20µm (Galli-Resta et al. 1997), and could be partially explained by the absence of retinal surface expansion implementation in our simulations. The CM mechanism implemented here is based only on local cues and short-distance interaction, and thereby follows the

description of tangential dispersion in mouse, reported as a local, short-distance, phenomenon (Reese and Galli-Resta 2002). More importantly, our results are consistent with previous studies showing that a cell tangential dispersion does not appear to be directly related to its time of birth, but rather to its cell type (Reese and Galli-Resta 2002).

The cellular organisation and RI dynamics resulting from the CM mechanism are in agreement with the literature, where it is reported that RI increases mostly between P1 and P5, while distance between cells still increasing after that period, from P1 to P10 (Reese and Keeley, 2015). After reaching the correct cell layer, a slower fine tangential positioning phase of RGC within the GCL has been reported (Galli-Resta et al. 1997; Amini, Rocha-Martins, and Norden 2017). Cellular movement during this period has been described as random but important for exact cellular positioning (Amini, Rocha-Martins, and Norden 2017). However, with regard to our results and as stated by other studies (Chow et al., 2005), they are likely to be related to mosaic formation and refinement. Indeed, these movements appear random as the whole RGC population (On, Off, On-Off population) is considered, while RGC populations should themselves be divided into types in order to meaningfully investigate RGCs lateral migration. If it would be possible to examine each type independently, it is likely that these movements, reported as random, would appear as coherent.

To further elaborate on our computational study, we created a model of pathological retinal development. Indeed, a single modelling condition of healthy development is insufficient to validate a computational model. For this reason, a simulation of the Dicer-1 deletion driven by the Pax6-αCre model has been carried out. The positive results and the reproduction of this abnormal development by our simulation support our model validation. Indeed, without modifying any cellular properties of simulation parameters, we reproduced the observed cellular dispersion, limited only in the distal directions where cell death occurred.

Some differences are to be noted between the biological model and our computational model of Dicer-1 deletion, notably the inferior migration distance observed in our simulations. This difference could partially be explained by retinal surface stretching during development, facilitating cellular dispersion. In addition, surviving cells could also express more sensitivity to chemical clues, and so respond more strongly, with higher cell-cell repulsion. Moreover, some cellular properties or migration characteristics could be changed due to the massive and localised cell

death resulting from Dicer-1 deletion. For instance, disappearance of all RGCs in some retinal regions could modify some ECM properties of these regions due to dislocation of tissue integrity. This, in turn, could facilitate cellular mobility and thus increase cell migration speed and distance.

Further testing of our simulation procedure was done by applying this mosaic formation mechanism to a different cell type, the SAC population. As discussed in the section 2.3, *in-vitro* investigations are particularly complex due to the early developmental stage of the retinas. Thus, a simulation of SACs mosaics development has been built. In particular, the interaction between the GCL and INL populations during mosaics formation has been investigated using this model. First, these simulations clearly show that our modelling procedure can successfully be applied to another cell population, without changing any simulation parameters. Indeed, we have been able to explain differences in GCL and INL mosaic regularities (RI of INL population being higher than the GCL population, see Figure 9 in section 2.2.1) by using only local interactions between SACs. This is the case if SACs constitute a unique population, or if GCL and INL populations are distinct (in other words, if one common or two distinct chemical cues are used). In the first case (if just one chemical cue is used), this RI difference can be explained by the higher number of cells migrating to the INL compared to the GCL. Indeed, the INL population represents a larger part of the initial regular SACs population than the GCL one. Precisely, the proportion of a population characterised by a highly regular mosaic dictates the regularity of the resulting sub-population. In other words, the bigger the sub-population, the closer the obtained RI will be from the initial population, if cells constituting this sub-population are chosen randomly. For instance, a sub-population representing 75% of an initial (highly regular) population will have a higher RI than a sub-population representing 25% of this initial population. In the second case (if two distinct chemical cues are used), this RI difference between GCL and INL populations can simply be explained by the higher cell density of SACs in the INL. This higher cell density in the INL allows more interactions and homotypic repulsion and thus the emergence of a higher RI than cells located in the GCL.

However, and surprisingly, only the simulation condition using a common chemical cue for mosaic formation is able to reproduce the exclusion factor observed between the GCL and INL populations. Indeed, if two mosaics (GCL and INL) are formed independently, they overlap frequently, thus exhibiting an exclusion factor lower than the one observed *in-vitro*. As no changes of RI or the exclusion factor are observed

once SACs have migrated to GCL and INL, this is an argument toward the hypothesis that SAC mosaics are formed at an early developmental stage, before SACs differentiation and migration to the GCL and INL. Again, it would be experimentally complex but informative to verify this assumption directly *in-vitro* or *in-vivo*. Finally, as the link between cell density and RI is observed for both RGCs and SACs populations, it strengthens the hypothesis of mosaic formation based only on close-range, locally available developmental cues, like molecular guidance. It could also suggest a common mosaic formation mechanism for all cell types in the retina.

It is important to point out that our simulations are in part based on an intrinsic clock, to regulate the transition between major phases of cellular development. The existence of such intrinsic cellular clocks has been previously demonstrated in mammals (Elliott et al. 2008; Alsio et al. 2013; La Torre, Georgi, and Reh 2013; Saurat et al. 2013), thus corroborating the verisimilitude of this modelling choice. The other major basis of our simulations is the presence of chemical cues supporting cells self-organisation mechanisms. Likewise, evidences of such chemical cues have been previously reported (Tissir and Goffinet 2003; Edwards et al. 2010; Kay, Chu, and Sanes 2012). The importance of chemical cues is particularly crucial in our simulations of dendritic development, where the targeted level of dendritic lamination directly depend on a chemical substance. Evidence supporting the existence of molecular guidance in dendrite proper lamination have been largely reported as well (Kay et al. 2004; Huberman, Clandinin, and Baier 2010; Matsuoka et al. 2011).

5.2 Dendritic growth

Despite several computational studies of dendritic growth in the cortex (Nowakowski, Hayes, and Egger 1992; van Pelt and Schierwagen 2004; Cuntz et al. 2010; van Ooyen 2011; Torben-Nielsen and De Schutter 2014), few to none realistic dendritic growth modelling has been conducted in the retina, and more specifically concerning RGCs.

As already reported here, we decided to simulate dendritic growth after mosaic completion (see section 4.1.2), using two normally distributed chemical guidance. These chemical substances represent the developmental cues given from SACs dendrites during development, allowing RGCs dendrites to laminate at the correct level (see section 1.1.2). This developmental guidance is a mandatory feature in our simulations.

Our results indicate that separating the RGC population into only the three major morphological categories (On, Off, On-Off) is too reductive. Indeed, building simulations using only three growth rules (On, Off, On-Off) cannot explain the observed heterogeneity of RGCs. In addition, it cannot explain the reported homogeneity inside each RGCs type, as observed for atypical arbours that are specific of a particular cell type. This shows that external cues driven growth rules are not enough to recapitulate the observed morphological diversity of RGCs dendritic arbours and the coherence inside each sub-group. This assumption is confirmed by adding more type specific internal growth rules that interact with the external developmental cues. Indeed, when thirteen distinct growth rules are created, the verisimilitude of obtained dendritic morphologies increases, allowing important morphological disparities but also similar dendritic shape within each RGC types. In other words, more internally driven developmental rules allow the emergence of specific morphologies that cannot be obtained with a single rule focusing on environmental interactions. This is particularly true for the J-RGCs family that exhibit very strong asymmetry in their dendritic arbour, that cannot be obtained without a specific, more internally driven, growth rule. Thus, we propose here that genetic factor might be an important component of RGCs dendritic shape determination. However, it should be pointed out that the impossibility in our simulations to reproduce the very low anisometry score for On RGCs may denote the existence of a specific mechanism during dendritic growth to increase the arbour symmetry. This may be an evolutionary mechanism that appeared to increase the dendritic coverage and homogeneous retinal coverage of On cells. Indeed, as mouse present a rod-dominated vision, a correct On RGCs dendritic coverage is particularly important for their survival as preys. Such a mechanism of dendrites self-avoidance has been previously described for RGCs (Dacey and Petersen 1992; Dacey 1993), and is believed to participate in yielding a uniform spatial coverage. Interestingly, this mechanism does not seem to be universal, with many RGCs exhibiting self-crossing dendrites (Reese and Keeley 2015), thus being in accordance with our hypothesis of a genetic factor for very low anisometric morphologies.

It is also important to point out that dendritic growth should be simulated with multiple cells simultaneously. This is mandatory in order to account for cell-cell dendritic interactions that occur during normal development. Indeed, such interactions have been demonstrated in the retina, and more particularly for RGCs. More precisely, RGCs of dissimilar types exhibit overlap of their dendritic arbours (Gauthier et al.

2009), while RGCs of the same type do not overlap, but instead they tile. This phenomenon has been shown for various RGCs (Dacey 1993; Vaney 1994), and can only be simulated when several cells are developing their dendritic arbours together. However, several simulations of dendritic development (Cuntz et al. 2010) are modelling cells independently (either one cell at a time, or without any cell-cell interactions). Hence, they do not take these dendritic interactions into account, which can potentially lead to misinterpretations.

The precision of the extracted RGCs morphologies from Sümbül et al., 2014 represents a rare opportunity to compare simulated RGCs with a database of experimentally obtained RGCs morphologies. Indeed, the high resolution of the z axis (in depth of the tissue) is still rare feature in 3D reconstructed neurons' morphology. Unfortunately, despite the large number of cells extracted by Sümbül et al., 2014, it is likely that several RGC types are under-sampled, especially J-RGC, mini-J-RGC and midi-J-RGC. Indeed, only 26 cells corresponding to these populations (so with an anisometry score higher than 0.70) are found in the Sümbül database while cells of the J-RGC family are believed to represent more than 20% of the whole RGC population. Around 74 cells should be found in the Sümbül database, to match theoretical values. 363 cells appear not to be enough to constitute an exhaustive and reliable representation of RGC morphological diversity. This under-sampling leads to incompatibilities between reported RGC type densities (Sanes and Masland, 2015), their described morphologies and characteristics measured on the Sümbül database. This is especially true for the anisometry score as J-RGC, mini-J-RGC and midi-J-RGC are known to express a very particular non symmetric arbour, but also branching number and arbour diameter as midi-J-RGC and mini-J-RGC are known to be of small size with fewer branching numbers. However, no exhaustive and fully reliable data base of RGC dendritic arbours' description exist, stressing the need for an open data and collaborative science. The lack of description of real morphologies also prevents us to finely tune all RGC types. Increasing the number of specific growth rules (probably to the point of having one specific growth behaviour per RGC type) would increase the realism of simulated RGC dendritic arbours.

Previous biological experiments showed the importance of intrinsic factors in the development of RGC dendritic tree morphologies (Montague and Friedlander 1989; 1991; Lin et al. 2004), while other point out the importance of environmental cues (Kay et al., 2004; Huberman et al., 2010; Matsuoka et al., 2011; Hoon et al. 2014). Using our simulations, we demonstrate here the importance of both mechanisms.

Indeed, only the interaction of two chemical cues (thus extrinsic factors representing the AC developmental guidance), with multiple distinct internally driven growth rules (intrinsic factors) can explain both the diversity of RGCs dendritic morphologies and the RGCs types homogeneity.

5.3 Limits and future work

In this thesis, we used a combination of experimental and computational approaches to investigate different mechanisms that could be required to give rise to a coherent and functional retina.

Using immunocytochemistry and large-scale electrophysiological recordings, we investigated potential mechanisms underlying hyperactivity generating stage II retinal waves. To our surprise, we discovered a population of auto-fluorescent cells in the RGC layer, organised as tight clusters forming an annulus. This annulus appears at the proximity of the optic disc at P2, then expands during development, reaching the retinal periphery around P6-P7. Finally, it starts to disintegrate and completely disappears by P10, coinciding with the switch to Stage-3 waves. Our results suggest that these cells may be hyper-active and generate strong neural activity during the period of Stage-2 waves. The presence of a transient population of hyper-active neurons during early development has been previously reported in cortical areas, suggesting a universal mechanism mediating hyper-excitability in developing CNS networks during the critical period for brain wiring. Interestingly, new observations obtained from E. Sernagor's lab show a collocation of clusters and the vascularisation edge during the development, as well as a collocation of clusters and expression of HIF-1, a transcription factor activated in hypoxic condition. These results suggest that this transient population could actively participate in angiogenesis and elaboration of retinal vascularity through activity-induced hypoxia.

However, as previously stated, the precise nature of this transient population remains to be fully elucidated. Several experiments could be considered to investigate further these cluster cells. Functional imaging and patch clamping experiments could bring more information about the precise implication of this population in the initialisation of Stage-2 waves, and about their hyper-active nature. More precisely, these experiments could elucidate if the clusters are acting as pacemaker by triggering the Stage II waves, but also bring more information about the cell types they are connected to. The link between the clusters and the vascularity could also be further investigated using several approaches. The first one could be achieved by

modulating the activity of the cluster cells (both increase and decrease of activity) and to investigate the resulting impact on the vascularity. A second complementary approach could be to influence the angiogenesis (both by impairing and promoting the neoangiogenesis) and measure the changes of the cluster cells' development. Finally, single cell RNA sequencing represents a particularly promising technique for cell characterisation. In addition of providing the precise genetic profile of an individual cell, this technique is especially useful to better understand a cell function in its environment. This technique could be used to better characterise and understand the cluster cells, but also to distinguish different cell types in the mature retina. By doing so, it would be possible to precisely determine the number and density of every RGC types. Interestingly, it could be used at various stages of development to investigate the emergence of cell types and the mechanisms dictating cell type determination. More, by combining imaging and single cell RNA sequencing, it could be possible to obtain the spatial position of every cell of interest, in addition with their genetic profile. Thus, it would be possible to investigate retinal development and mosaic creation at very early stages of the development. This could for instance allow us to determine if some genetic differences exist between RGCs at early developmental stages, before the emergence of mosaics, or the respective influence of intrinsic and extrinsic factors upon cellular differentiation and mosaic creation. Likewise, it would be possible to investigate if genetic differences exist between the GCL and INL SAC populations. If some differences are to be noted, it would also be possible to determine at which developmental stage these differences emerge, and which factor (intrinsic and extrinsic) influence the cell layer each cell will migrate to.

Using information gathered from our *in-vitro* experiments and from the literature, we built agent-based computational simulations to investigate mechanisms underlying retinal mosaics formation and dendritic development. In particular, we investigated the requirements for mosaics' formation through development, and the specific impact of each mosaic formation mechanism. Our simulations clearly showed that mosaic formation can be explained using only simple rules, based on locally available information and short-range cell-cell interactions. In additions, they indicate that cellular migration is the only mechanism able to give rise to regular mosaics. This high regularity can be achieved using only limited migration distance. We also found that cell death can create regular mosaics only if the death rate is kept below 30%, thus indicating that programmed cell death is implicated in another mechanism

than mosaic formation. Interestingly, we also showed that all RGC types do not form mosaics, thus agreeing with recent studies. Indeed, in our simulations, only RGC populations of high to mid-density can self-organise as regular mosaics.

Using the agent-based approach, we also built simulations to investigate the requirements for realistic RGCs dendritic development. We showed that realistic dendritic arbour morphologies can be obtained using only simple rules, based on locally available information. Importantly, we demonstrated that only the interaction of extrinsic factors (developmental cue), with multiple distinct intrinsic factors (internally driven growth rules) can explain both the diversity of RGCs dendritic morphologies and the RGCs types homogeneity.

As mentioned in the Introduction Chapter, computational simulations can pursue four goals: 1. to provide a reasoning aid. 2. to remove ambiguity from biological theories. 3. to explain large systems by small simple elements. 4. to replace or minimise the use of animal experimentation. The simulations presented in this thesis fulfilled all these four aims.

Indeed, in order to model mosaics formation, it has first been mandatory to determine the number of RGC types in the retina and their respective densities. By doing so, we discovered that less On than Off and ON-Off RGC have been reported and characterised in the literature, thus leading to the hypothesis that the On RGC population might be composed of more type than the Off or On-Off RGC populations. The implementation of each mosaic formation mechanism (CF, CD, CM) also helped to clarify how they could form mosaics, defining the biological requirements and mechanisms that could underlie mosaic formation. Likewise, the implementation of dendritic development brought clarifications about the precise mechanisms and information needed in order to grow realistic dendritic arbours. The modelling approach used in this work is particularly well suited to explain large system formation by simpler elements as agent-based simulations are precisely built on the principle of agents. Agents are simple, independent and explicitly represented objects that can only have access to close range information, without any central simulation control. Thus, in our modelling, mosaic formation and dendritic arbour growth are achieved using only simple independent agents (cells and dendrites) that interact with their local environment to self-organise in more complex structures. Finally, our results and predictions could be used as preliminary results by experimentalists, thus helping them to reduce the number of plausible outcomes and

select possible experiments for further investigations. In turn, this could minimise the number of experiments and animals used.

Nonetheless, our simulations are built upon some assumptions and would need experimental verifications of these assumptions and of our predictions in order to further validate our model. It would for instance be informative to verify if low density populations of RGCs are not forming regular mosaics, accordingly to our prediction. Furthermore, every parameter of our simulations has been hand-tuned. An automatic procedure for parameter tuning could validate the chosen parameters values but could also benefit the simulations with more finely tuned values. More, an automatic procedure could be used to determine the theoretical ideal number of RGC types for mosaic formation and dendritic growth rules, in addition of their characteristics (cell density, behaviour, etc.). Other investigations could also be considered to elaborate further either our model or its results analysis. I would for instance be interesting to calculate the distance recovery profile to assess mosaics' regularity and investigate if significant differences are to be noted compared to analysis using the RI. Our model could also be further elaborated, by integrating additional cell types and the corresponding interactions between and inside each cell populations. The first step would consist in the incorporation of the amacrine cell population alongside the RGC population. This would be particularly interesting as amacrine cells are believed to provide strong developmental cue to RGCs dendrites, while RGCs are believed to give developmental cue to some amacrine cells for the precise positioning of their stratification level. Investigating the interactions between amacrine cells and RGCs, in addition of the interactions within each population, could greatly benefit our understanding of retinal development.

References

Abbott, L. F. 2008. ‘Theoretical Neuroscience Rising’. *Neuron* 60 (3): 489–95. https://doi.org/10.1016/j.neuron.2008.10.019.

Aguilar, Edith, Michael I. Dorrell, David Friedlander, Ruth A. Jacobson, Audra Johnson, Valentina Marchetti, Stacey K. Moreno, Matthew R. Ritter, and Martin Friedlander. 2008. ‘Chapter 6 Ocular Models of Angiogenesis’. In *Methods in Enzymology*, 444:115–58. Elsevier. https://doi.org/10.1016/S0076-6879(08)02806-1.

Alsio, J. M., B. Tarchini, M. Cayouette, and F. J. Livesey. 2013. ‘Ikaros Promotes Early-Born Neuronal Fates in the Cerebral Cortex’. *Proceedings of the National Academy of Sciences* 110 (8): E716–25. https://doi.org/10.1073/pnas.1215707110.

Altrock, Philipp M., Lin L. Liu, and Franziska Michor. 2015. ‘The Mathematics of Cancer: Integrating Quantitative Models’. *Nature Reviews Cancer* 15 (12): 730–45. https://doi.org/10.1038/nrc4029.

Amdahl, Gene M. 1967. ‘Validity of the Single Processor Approach to Achieving Large Scale Computing Capabilities’. In *Proceedings of the April 18-20, 1967, Spring Joint Computer Conference on - AFIPS ’67 (Spring)*, 483. Atlantic City, New Jersey: ACM Press. https://doi.org/10.1145/1465482.1465560.

Amini, Rana, Mauricio Rocha-Martins, and Caren Norden. 2017. ‘Neuronal Migration and Lamination in the Vertebrate Retina’. *Frontiers in Neuroscience* 11: 742. https://doi.org/10.3389/fnins.2017.00742.

Anderson, Alexander R. A. 2005. ‘A Hybrid Mathematical Model of Solid Tumour Invasion: The Importance of Cell Adhesion’. *Mathematical Medicine and Biology: A Journal of the IMA* 22 (2): 163–86. https://doi.org/10.1093/imammb/dqi005.

Assali, Ahlem, Patricia Gaspar, and Alexandra Rebsam. 2014. ‘Activity Dependent Mechanisms of Visual Map Formation - From Retinal Waves to Molecular Regulators’. *Seminars in Cell & Developmental Biology* 35 (November): 136–46. https://doi.org/10.1016/j.semcdb.2014.08.008.

Atick, Joseph J., and A. Norman Redlich. 1990. ‘Towards a Theory of Early Visual Processing’. *Neural Computation* 2 (3): 308–20. https://doi.org/10.1162/neco.1990.2.3.308.

Baden, Tom, Philipp Berens, Katrin Franke, Miroslav Román Rosón, Matthias Bethge, and Thomas Euler. 2016. ‘The Functional Diversity of Retinal Ganglion Cells in the Mouse’. *Nature* 529 (7586): 345–50. https://doi.org/10.1038/nature16468.

Baker, Monya. 2013. ‘Neuroscience: Through the Eyes of a Mouse’. *Nature* 502 (7470): 156–58. https://doi.org/10.1038/502156a.

Bauer, Roman, Frédéric Zubler, Sabina Pfister, Andreas Hauri, Michael Pfeiffer, Dylan R. Muir, and Rodney J. Douglas. 2014. ‘Developmental Self-Construction and -Configuration of Functional Neocortical Neuronal Networks’. *PLoS Computational Biology* 10 (12): e1003994. https://doi.org/10.1371/journal.pcbi.1003994.

Berson, David M., Ana Maria Castrucci, and Ignacio Provencio. 2010. ‘Morphology and Mosaics of Melanopsin-Expressing Retinal Ganglion Cell Types in Mice’. *The Journal of Comparative Neurology* 518 (13): 2405–22. https://doi.org/10.1002/cne.22381.

Blinova, K., Carroll, S., Bose, S., Smirnov, A. V., Harvey, J. J., Knutson, J. R. and Balaban, R. S. 2005. ‘Distribution of Mitochondrial NADH Fluorescence Lifetimes: Steady-State Kinetics of Matrix NADH Interactions’. *Biochemistry* 2005 44 (7), 2585-2594. https://doi.org/10.1021%2Fbi0485124

Blankenship, Aaron G., Kevin J. Ford, Juliette Johnson, Rebecca P. Seal, Robert H. Edwards, David R. Copenhagen, and Marla B. Feller. 2009. ‘Synaptic and Extrasynaptic Factors Governing Glutamatergic Retinal Waves’. *Neuron* 62 (2): 230–41. https://doi.org/10.1016/j.neuron.2009.03.015.

Bodnarenko SR and Chalupa LM. 1993. 'Stratification of ON and OFF ganglion cell dendrites depends on glutamate-mediated afferent activity in the developing retina'. *Nature* 8;364(6433):144-6.

Boije, Henrik, Shahrzad Shirazi Fard, Per-Henrik Edqvist, and Finn Hallböök. 2016. 'Horizontal Cells, the Odd Ones Out in the Retina, Give Insights into Development and Disease'. *Frontiers in Neuroanatomy* 10: 77. https://doi.org/10.3389/fnana.2016.00077.

Braunger, Barbara M., Cora Demmer, and Ernst R. Tamm. 2014. 'Programmed Cell Death during Retinal Development of the Mouse Eye'. *Advances in Experimental Medicine and Biology* 801: 9–13. https://doi.org/10.1007/978-1-4614-3209-8_2.

Bray, Dennis. 2001. *Cell Movements: From Molecules to Motility*. 2nd ed. New York: Garland Pub.

Breitwieser, L., A. Hesam, J. de Montigny, V. Vavourakis, A. Iosif, J. Jennings, M. Kaiser, M. Manca, A. Di Meglio, Z. Al-Ars, F. Rademakers, O. Mutlu and R. Bauer. *bioRxiv* 2020.06.08.139949. https://doi.org/10.1101/2020.06.08.139949

Burbridge, Timothy J., Hong-Ping Xu, James B. Ackman, Xinxin Ge, Yueyi Zhang, Mei-Jun Ye, Z. Jimmy Zhou, Jian Xu, Anis Contractor, and Michael C. Crair. 2014. 'Visual Circuit Development Requires Patterned Activity Mediated by Retinal Acetylcholine Receptors'. *Neuron* 84 (5): 1049–64. https://doi.org/10.1016/j.neuron.2014.10.051.

Butts, D. A., M. B. Feller, C. J. Shatz, and D. S. Rokhsar. 1999. 'Retinal Waves Are Governed by Collective Network Properties'. *The Journal of Neuroscience: The Official Journal of the Society for Neuroscience* 19 (9): 3580–93.

Byerly, Mardi S., and Seth Blackshaw. 2009. 'Vertebrate Retina and Hypothalamus Development'. *Wiley Interdisciplinary Reviews. Systems Biology and Medicine* 1 (3): 380–89. https://doi.org/10.1002/wsbm.22.

Catsicas, Marina, Viola Bonness, David Becker, and Peter Mobbs. 1998. 'Spontaneous Ca2+ Transients and Their Transmission in the Developing Chick Retina'. *Current Biology* 8 (5): 283–88. https://doi.org/10.1016/S0960-9822(98)70110-1.

Chen, Shan, and Wei Li. 2012. ‘A Color-Coding Amacrine Cell May Provide a Blue-off Signal in a Mammalian Retina’. *Nature Neuroscience* 15 (7): 954–56. https://doi.org/10.1038/nn.3128.

Choi, Jung-Hwan, Mei-Yee Law, Chi-Bin Chien, Brian A Link, and Rachel OL Wong. 2010. ‘In Vivo Development of Dendritic Orientation in Wild-Type and Mislocalized Retinal Ganglion Cells’. *Neural Development* 5 (1): 29. https://doi.org/10.1186/1749-8104-5-29.

Chow, Renee W., Alexandra D. Almeida, Owen Randlett, Caren Norden, and William A. Harris. 2015. ‘Inhibitory Neuron Migration and IPL Formation in the Developing Zebrafish Retina’. *Development* 142 (15): 2665–77. https://doi.org/10.1242/dev.122473.

Clifford, Meredith A., Wardah Athar, Carrie E. Leonard, Alexandra Russo, Paul J. Sampognaro, Marie-Sophie Van der Goes, Denver A. Burton, et al. 2014. ‘EphA7 Signaling Guides Cortical Dendritic Development and Spine Maturation’. *Proceedings of the National Academy of Sciences* 111 (13): 4994–99. https://doi.org/10.1073/pnas.1323793111.

Cohen-Cory, Susana, and Barbara Lom. 2004. ‘Neurotrophic Regulation of Retinal Ganglion Cell Synaptic Connectivity: From Axons and Dendrites to Synapses’. *The International Journal of Developmental Biology* 48 (8–9): 947–56. https://doi.org/10.1387/ijdb.041883sc.

Cook, J. E. 1996. ‘Spatial Properties of Retinal Mosaics: An Empirical Evaluation of Some Existing Measures’. *Visual Neuroscience* 13 (1): 15–30. https://doi.org/10.1017/S0952523800007094.

Cuntz, Hermann, Friedrich Forstner, Alexander Borst, and Michael Häusser. 2010. ‘One Rule to Grow Them All: A General Theory of Neuronal Branching and Its Practical Application’. *PLoS Computational Biology* 6 (8). https://doi.org/10.1371/journal.pcbi.1000877.

Dacey, D. M. 1993. ‘The Mosaic of Midget Ganglion Cells in the Human Retina’. *The Journal of Neuroscience: The Official Journal of the Society for Neuroscience* 13 (12): 5334–55.

Dacey, D. M., and M. R. Petersen. 1992. ‘Dendritic Field Size and Morphology of Midget and Parasol Ganglion Cells of the Human Retina.’ *Proceedings of the National Academy of Sciences* 89 (20): 9666–70. https://doi.org/10.1073/pnas.89.20.9666.

Devries, Steven H., and Denis A. Baylor. 1997. ‘Mosaic Arrangement of Ganglion Cell Receptive Fields in Rabbit Retina’. *Journal of Neurophysiology* 78 (4): 2048–60. https://doi.org/10.1152/jn.1997.78.4.2048.

Dorrell, Michael I., and Martin Friedlander. 2006. ‘Mechanisms of Endothelial Cell Guidance and Vascular Patterning in the Developing Mouse Retina’. *Progress in Retinal and Eye Research* 25 (3): 277–95. https://doi.org/10.1016/j.preteyeres.2006.01.001.

Duan, Xin, Mu Qiao, Fengfeng Bei, In-Jung Kim, Zhigang He, and Joshua R. Sanes. 2015. ‘Subtype-Specific Regeneration of Retinal Ganglion Cells Following Axotomy: Effects of Osteopontin and MTOR Signaling’. *Neuron* 85 (6): 1244–56. https://doi.org/10.1016/j.neuron.2015.02.017.

Edwards, Malia M., Elmina Mammadova-Bach, Fabien Alpy, Annick Klein, Wanda L. Hicks, Michel Roux, Patricia Simon-Assmann, et al. 2010. ‘Mutations in *Lama1* Disrupt Retinal Vascular Development and Inner Limiting Membrane Formation’. *Journal of Biological Chemistry* 285 (10): 7697–7711. https://doi.org/10.1074/jbc.M109.069575.

Edwards, Malia M., D. Scott McLeod, Renzhong Li, Rhonda Grebe, Imran Bhutto, Xiuqian Mu, and Gerard A. Lutty. 2012. ‘The Deletion of Math5 Disrupts Retinal Blood Vessel and Glial Development in Mice’. *Experimental Eye Research* 96 (1): 147–56. https://doi.org/10.1016/j.exer.2011.12.005.

Eglen, Stephen J. 2006. ‘Development of Regular Cellular Spacing in the Retina: Theoretical Models’. *Mathematical Medicine and Biology: A Journal of the IMA* 23 (2): 79–99. https://doi.org/10.1093/imammb/dql003.

Eglen, Stephen J., and David J. Willshaw. 2002. ‘Influence of Cell Fate Mechanisms upon Retinal Mosaic Formation: A Modelling Study’. *Development* 129 (23): 5399–5408.

Elliott, Jimmy, Christine Jolicoeur, Vasanth Ramamurthy, and Michel Cayouette. 2008. ‘Ikaros Confers Early Temporal Competence to Mouse Retinal Progenitor Cells’. *Neuron* 60 (1): 26–39. https://doi.org/10.1016/j.neuron.2008.08.008.

Elstrott, Justin, Anastasia Anishchenko, Martin Greschner, Alexander Sher, Alan M. Litke, E.J. Chichilnisky, and Marla B. Feller. 2008. ‘Direction Selectivity in the Retina Is Established Independent of Visual Experience and Cholinergic Retinal Waves’. *Neuron* 58 (4): 499–506. https://doi.org/10.1016/j.neuron.2008.03.013.

Erskine, Lynda, and Eloisa Herrera. 2007. ‘The Retinal Ganglion Cell Axon’s Journey: Insights into Molecular Mechanisms of Axon Guidance’. *Developmental Biology* 308 (1): 1–14. https://doi.org/10.1016/j.ydbio.2007.05.013.

———. 2014. ‘Connecting the Retina to the Brain’. *ASN Neuro* 6 (6): 175909141456210. https://doi.org/10.1177/1759091414562107.

Estevez, M. E., P. M. Fogerson, M. C. Ilardi, B. G. Borghuis, E. Chan, S. Weng, O. N. Auferkorte, J. B. Demb, and D. M. Berson. 2012. ‘Form and Function of the M4 Cell, an Intrinsically Photosensitive Retinal Ganglion Cell Type Contributing to Geniculocortical Vision’. *Journal of Neuroscience* 32 (39): 13608–20. https://doi.org/10.1523/JNEUROSCI.1422-12.2012.

Farah, Mohamed H. 2006. ‘Neurogenesis and Cell Death in the Ganglion Cell Layer of Vertebrate Retina’. *Brain Research Reviews* 52 (2): 264–74. https://doi.org/10.1016/j.brainresrev.2006.04.002.

Farrow, Karl, and Richard H. Masland. 2011. ‘Physiological Clustering of Visual Channels in the Mouse Retina’. *Journal of Neurophysiology* 105 (4): 1516–30. https://doi.org/10.1152/jn.00331.2010.

Finlay, B, and S Pallas. 1989. ‘Control of Cell Number in the Developing Mammalian Visual System’. *Progress in Neurobiology* 32 (3): 207–34. https://doi.org/10.1016/0301-0082(89)90017-8.

Ford, K. J., A. L. Felix, and M. B. Feller. 2012. ‘Cellular Mechanisms Underlying spatiotemporal Features of Cholinergic Retinal Waves’. *Journal of Neuroscience* 32 (3): 850–63. https://doi.org/10.1523/JNEUROSCI.5309-12.2012.

Fu, Yingbin, and King-Wai Yau. 2007. ‘Phototransduction in Mouse Rods and Cones’. *Pflugers Archiv: European Journal of Physiology* 454 (5): 805–19. https://doi.org/10.1007/s00424-006-0194-y.

Galli-Resta, L., G. Resta, S. S. Tan, and B. E. Reese. 1997. ‘Mosaics of Islet-1-Expressing Amacrine Cells Assembled by Short-Range Cellular Interactions’. *The Journal of Neuroscience: The Official Journal of the Society for Neuroscience* 17 (20): 7831–38.

Galli-Resta, Lucia. 2002. ‘Putting Neurons in the Right Places: Local Interactions in the Genesis of Retinal Architecture’. *Trends in Neurosciences* 25 (12): 638–43.

Galli-Resta, Lucia, Paola Leone, David Bottari, Monica Ensini, Elisa Rigosi, and Elena Novelli. 2008. ‘The Genesis of Retinal Architecture: An Emerging Role for Mechanical Interactions?’ *Progress in Retinal and Eye Research* 27 (3): 260–83. https://doi.org/10.1016/j.preteyeres.2008.02.001.

Gauthier, Jeffrey L., Greg D. Field, Alexander Sher, Martin Greschner, Jonathon Shlens, Alan M. Litke, and E. J. Chichilnisky. 2009. ‘Receptive Fields in Primate Retina Are Coordinated to Sample Visual Space More Uniformly’. *PLoS Biology* 7 (4): e1000063. https://doi.org/10.1371/journal.pbio.1000063.

Georgi, S. A., and T. A. Reh. 2010. ‘Dicer Is Required for the Transition from Early to Late Progenitor State in the Developing Mouse Retina’. *Journal of Neuroscience* 30 (11): 4048–61. https://doi.org/10.1523/JNEUROSCI.4982-09.2010.

Gerlee, P., and A.R.A. Anderson. 2007. ‘An Evolutionary Hybrid Cellular Automaton Model of Solid Tumour Growth’. *Journal of Theoretical Biology* 246 (4): 583–603. https://doi.org/10.1016/j.jtbi.2007.01.027.

Godinho, Leanne, Jeff S. Mumm, Philip R. Williams, Eric H. Schroeter, Amy Koerber, Seung W. Park, Steven D. Leach, and Rachel O. L. Wong. 2005. 'Targeting of Amacrine Cell Neurites to Appropriate Synaptic Laminae in the Developing Zebrafish Retina'. *Development* 132 (22): 5069–79. https://doi.org/10.1242/dev.02075.

Gollisch, Tim, and Markus Meister. 2010. 'Eye Smarter than Scientists Believed: Neural Computations in Circuits of the Retina'. *Neuron* 65 (2): 150–64. https://doi.org/10.1016/j.neuron.2009.12.009.

Goodenberger, McKinsey L., and Robert B. Jenkins. 2012. 'Genetics of Adult Glioma'. *Cancer Genetics* 205 (12): 613–21. https://doi.org/10.1016/j.cancergen.2012.10.009.

Graves MS, Hassell T, Beier BL, Albors GO, Irazoqui PP. 'Electrically mediated neuronal guidance with applied alternating current electric fields'. *Ann Biomed Eng*. 2011;39(6):1759-1767. doi:10.1007/s10439-011-0259-8

Greschner, Martin, Alexander K. Heitman, Greg D. Field, Peter H. Li, Daniel Ahn, Alexander Sher, Alan M. Litke, and E.J. Chichilnisky. 2016. 'Identification of a Retinal Circuit for Recurrent Suppression Using Indirect Electrical Imaging'. *Current Biology* 26 (15): 1935–42. https://doi.org/10.1016/j.cub.2016.05.051.

Günhan-Agar, E., D. Kahn, and L. M. Chalupa. 2000. 'Segregation of on and off Bipolar Cell Axonal Arbors in the Absence of Retinal Ganglion Cells'. *The Journal of Neuroscience: The Official Journal of the Society for Neuroscience* 20 (1): 306–14.

Hafler, B. P., N. Surzenko, K. T. Beier, C. Punzo, J. M. Trimarchi, J. H. Kong, and C. L. Cepko. 2012. 'Transcription Factor Olig2 Defines Subpopulations of Retinal Progenitor Cells Biased toward Specific Cell Fates'. *Proceedings of the National Academy of Sciences* 109 (20): 7882–87. https://doi.org/10.1073/pnas.1203138109.

He, Jie, Gen Zhang, Alexandra D. Almeida, Michel Cayouette, Benjamin D. Simons, and William A. Harris. 2012. 'How Variable Clones Build an Invariant Retina'. *Neuron* 75 (5): 786–98. https://doi.org/10.1016/j.neuron.2012.06.033.

Hennig, M. H., J. Grady, J. van Coppenhagen, and E. Sernagor. 2011. 'Age-Dependent Homeostatic Plasticity of GABAergic Signaling in Developing Retinal Networks'. *Journal of Neuroscience* 31 (34): 12159–64. https://doi.org/10.1523/JNEUROSCI.3112-11.2011.

Hennig, Matthias H., Christopher Adams, David Willshaw, and Evelyne Sernagor. 2009. 'Early-Stage Waves in the Retinal Network Emerge Close to a Critical State Transition between Local and Global Functional Connectivity'. *The Journal of Neuroscience: The Official Journal of the Society for Neuroscience* 29 (4): 1077–86. https://doi.org/10.1523/JNEUROSCI.4880-08.2009.

Hilgen, Gerrit, Sahar Pirmoradian, Daniela Pamplona, Pierre Kornprobst, Bruno Cessac, Matthias H. Hennig, and Evelyne Sernagor. 2017. 'Pan-Retinal Characterisation of Light Responses from Ganglion Cells in the Developing Mouse Retina'. *Scientific Reports* 7 (1). https://doi.org/10.1038/srep42330.

Hoon, Mrinalini, Haruhisa Okawa, Luca Della Santina, and Rachel O. L. Wong. 2014. 'Functional Architecture of the Retina: Development and Disease'. *Progress in Retinal and Eye Research* 42 (September): 44–84. https://doi.org/10.1016/j.preteyeres.2014.06.003.

Hu, Caiping, DiJon D. Hill, and Kwoon Y. Wong. 2013. 'Intrinsic Physiological Properties of the Five Types of Mouse Ganglion-Cell Photoreceptors'. *Journal of Neurophysiology* 109 (7): 1876–89. https://doi.org/10.1152/jn.00579.2012.

Huang, Eric J., and Louis F. Reichardt. 2003. 'Trk Receptors: Roles in Neuronal Signal Transduction'. *Annual Review of Biochemistry* 72 (1): 609–42. https://doi.org/10.1146/annurev.biochem.72.121801.161629.

Huberman, A. D., T. R. Clandinin, and H. Baier. 2010. 'Molecular and Cellular Mechanisms of Lamina-Specific Axon Targeting'. *Cold Spring Harbor Perspectives in Biology* 2 (3): a001743–a001743. https://doi.org/10.1101/cshperspect.a001743.

Huberman, Andrew D., Mihai Manu, Selina M. Koch, Michael W. Susman, Amanda Brosius Lutz, Erik M. Ullian, Stephen A. Baccus, and Ben A. Barres. 2008. 'Architecture and Activity-Mediated Refinement of Axonal Projections from a

Mosaic of Genetically Identified Retinal Ganglion Cells'. *Neuron* 59 (3): 425–38. https://doi.org/10.1016/j.neuron.2008.07.018.

Huckfeldt, Rachel M, Timm Schubert, Josh L Morgan, Leanne Godinho, Graziella Di Cristo, Z Josh Huang, and Rachel O L Wong. 2009. 'Transient Neurites of Retinal Horizontal Cells Exhibit Columnar Tiling via Homotypic Interactions'. *Nature Neuroscience* 12 (1): 35–43. https://doi.org/10.1038/nn.2236.

Hunter, Peter J., and Marco Viceconti. 2009. 'The VPH-Physiome Project: Standards and Tools for Multiscale Modeling in Clinical Applications'. *IEEE Reviews in Biomedical Engineering* 2: 40–53. https://doi.org/10.1109/RBME.2009.2036204.

Jacoby, Jason, Yongling Zhu, Steven H. DeVries, and Gregory W. Schwartz. 2015. 'An Amacrine Cell Circuit for Signaling Steady Illumination in the Retina'. *Cell Reports* 13 (12): 2663–70. https://doi.org/10.1016/j.celrep.2015.11.062.

Jeffery G., 1984. 'Retinal ganglion cell death and terminal field retraction in the developing rodent visual system'. *Developmental Brain Research*, 13 (1984), pp. 81-97

Jeon, Chang-Jin, Enrica Strettoi, and Richard H. Masland. 'The Major Cell Populations of the Mouse Retina.' *Journal of Neuroscience* 18.21 (1998): 8936-8946.

Jeyarasasingam, G., C. J. Snider, G. M. Ratto, and L. M. Chalupa. 1998. 'Activity-Regulated Cell Death Contributes to the Formation of ON and OFF Alpha Ganglion Cell Mosaics'. *The Journal of Comparative Neurology* 394 (3): 335–43.

Karagiannis, Emmanouil D., and Aleksander S. Popel. 2006. 'Distinct Modes of Collagen Type I Proteolysis by Matrix Metalloproteinase (MMP) 2 and Membrane Type I MMP during the Migration of a Tip Endothelial Cell: Insights from a Computational Model'. *Journal of Theoretical Biology* 238 (1): 124–45. https://doi.org/10.1016/j.jtbi.2005.05.020.

Kassraian-Fard, Pegah, Michael Pfeiffer, and Roman Bauer. 2020. 'A Generative Growth Model for Thalamocortical Axonal Branching in Primary Visual Cortex'.

Edited by Geoffrey J Goodhill. *PLOS Computational Biology* 16 (2): e1007315. https://doi.org/10.1371/journal.pcbi.1007315.

Kay, J. N., I. De la Huerta, I.-J. Kim, Y. Zhang, M. Yamagata, M. W. Chu, M. Meister, and J. R. Sanes. 2011. 'Retinal Ganglion Cells with Distinct Directional Preferences Differ in Molecular Identity, Structure, and Central Projections'. *Journal of Neuroscience* 31 (21): 7753–62. https://doi.org/10.1523/JNEUROSCI.0907-11.2011.

Kay, Jeremy N., Monica W. Chu, and Joshua R. Sanes. 2012. 'MEGF10 and MEGF11 Mediate Homotypic Interactions Required for Mosaic Spacing of Retinal Neurons'. *Nature* 483 (7390): 465–69. https://doi.org/10.1038/nature10877.

Kay, Jeremy N., Tobias Roeser, Jeff S. Mumm, Leanne Godinho, Ana Mrejeru, Rachel O. L. Wong, and Herwig Baier. 2004. 'Transient Requirement for Ganglion Cells during Assembly of Retinal Synaptic Layers'. *Development* 131 (6): 1331–42. https://doi.org/10.1242/dev.01040.

Keeley PW, Eglen SJ, Reese BE. From random to regular: Variation in the patterning of retinal mosaics [published online ahead of print, 2020 Feb 5]. J Comp Neurol. 2020;10.1002/cne.24880. doi:10.1002/cne.24880

Kim, I.-J., Y. Zhang, M. Meister, and J. R. Sanes. 2010. 'Laminar Restriction of Retinal Ganglion Cell Dendrites and Axons: Subtype-Specific Developmental Patterns Revealed with Transgenic Markers'. *Journal of Neuroscience* 30 (4): 1452–62. https://doi.org/10.1523/JNEUROSCI.4779-09.2010.

Kirby, Michael A., and Leo M. Chalupa. 1986. 'Retinal Crowding Alters the Morphology of Alpha Ganglion Cells'. *The Journal of Comparative Neurology* 251 (4): 532–41. https://doi.org/10.1002/cne.902510408.

Koeppen, Bruce M, and Bruce A Stanton. 2014. *Berne & Levy Physiology, Updated Edition.* Saintt Louis: Elsevier Health Sciences. http://public.eblib.com/choice/publicfullrecord.aspx?p=4718645.

Kohwi, Minoree, and Chris Q. Doe. 2013. ‘Temporal Fate Specification and Neural Progenitor Competence during Development’. *Nature Reviews Neuroscience* 14 (12): 823–38. https://doi.org/10.1038/nrn3618.

Kolb, Helga. 1995. ‘Simple Anatomy of the Retina’. In *Webvision: The Organisation of the Retina and Visual System*, edited by Helga Kolb, Eduardo Fernandez, and Ralph Nelson. Salt Lake City (UT): University of Utah Health Sciences Center. http://www.ncbi.nlm.nih.gov/books/NBK11533/.

Kolb, Helga, Eduardo Fernandez, and Ralph Nelson. 2016. *Webvision - The Organisation of the Retina and Visual System*. University of Utah Health Sciences Center Salt Lake City (UT). http://webvision.med.utah.edu/.

Komiyama, Takaki, Lora B. Sweeney, Oren Schuldiner, K. Christopher Garcia, and Liqun Luo. 2007. ‘Graded Expression of Semaphorin-1a Cell-Autonomously Directs Dendritic Targeting of Olfactory Projection Neurons’. *Cell* 128 (2): 399–410. https://doi.org/10.1016/j.cell.2006.12.028.

Kunzevitzky, Noelia J., Kevin T. Willeford, William J. Feuer, Monica V. Almeida, and Jeffrey L. Goldberg. 2013. ‘Amacrine Cell Subtypes Differ in Their Intrinsic Neurite Growth Capacity’. *Investigative Ophthalmology & Visual Science* 54 (12): 7603–13. https://doi.org/10.1167/iovs.13-12691.

La Torre, A., S. Georgi, and T. A. Reh. 2013. ‘Conserved MicroRNA Pathway Regulates Developmental Timing of Retinal Neurogenesis’. *Proceedings of the National Academy of Sciences* 110 (26): E2362–70. https://doi.org/10.1073/pnas.1301837110.

Landi, Silvia, Maria Cristina Cenni, Lamberto Maffei, and Nicoletta Berardi. 2007. ‘Environmental Enrichment Effects on Development of Retinal Ganglion Cell Dendritic Stratification Require Retinal BDNF’. *PloS One* 2 (4): e346. https://doi.org/10.1371/journal.pone.0000346.

Lettvin, J. Y., H. R. Maturana, W. S. McCulloch and W. H. Pitts, ‘What the Frog's Eye Tells the Frog's Brain’. Proceedings of the IRE, vol. 47, no. 11, pp. 1940-1951, Nov. 1959.

Lin, Bin, Steven W. Wang, and Richard H. Masland. 2004. ‘Retinal Ganglion Cell Type, Size, and Spacing Can Be Specified Independent of Homotypic Dendritic Contacts’. *Neuron* 43 (4): 475–85. https://doi.org/10.1016/j.neuron.2004.08.002.

Litke, A.M., N. Bezayiff, E.J. Chichilnisky, W. Cunningham, W. Dabrowski, A.A. Grillo, M. Grivich, et al. 2004. ‘What Does the Eye Tell the Brain?: Development of a System for the Large-Scale Recording of Retinal Output Activity’. *IEEE Transactions on Nuclear Science* 51 (4): 1434–40. https://doi.org/10.1109/TNS.2004.832706.

Livesey, F. J., and C. L. Cepko. 2001. ‘Vertebrate Neural Cell-Fate Determination: Lessons from the Retina’. *Nature Reviews Neuroscience* 2 (2): 109–18. https://doi.org/10.1038/35053522.

Luhmann, Heiko J., Sergei Kirischuk, and Werner Kilb. 2018. ‘The Superior Function of the Subplate in Early Neocortical Development’. *Frontiers in Neuroanatomy* 12 (November). https://doi.org/10.3389/fnana.2018.00097.

Luhmann, Heiko J., Anne Sinning, Jenq-Wei Yang, Vicente Reyes-Puerta, Maik C. Stüttgen, Sergei Kirischuk, and Werner Kilb. 2016. ‘Spontaneous Neuronal Activity in Developing Neocortical Networks: From Single Cells to Large-Scale Interactions’. *Frontiers in Neural Circuits* 10 (May). https://doi.org/10.3389/fncir.2016.00040.

Luo, Liqun, and Dennis D. M. O’Leary. 2005. ‘Axon Retraction and Degeneration in Development and Disease’. *Annual Review of Neuroscience* 28: 127–56. https://doi.org/10.1146/annurev.neuro.28.061604.135632.

Maccione, Alessandro, Matthias H. Hennig, Mauro Gandolfo, Oliver Muthmann, James van Coppenhagen, Stephen J. Eglen, Luca Berdondini, and Evelyne Sernagor. 2014. ‘Following the Ontogeny of Retinal Waves: Pan-Retinal Recordings of Population Dynamics in the Neonatal Mouse’. *The Journal of Physiology* 592 (7): 1545–63. https://doi.org/10.1113/jphysiol.2013.262840.

Maher, E. A. 2001. ‘Malignant Glioma: Genetics and Biology of a Grave Matter’. *Genes & Development* 15 (11): 1311–33. https://doi.org/10.1101/gad.891601.

Maiorano, Nicola A., and Robert Hindges. 2013. ‘Restricted Perinatal Retinal Degeneration Induces Retina Reshaping and Correlated Structural Rearrangement of the Retinotopic Map’. *Nature Communications* 4 (1). https://doi.org/10.1038/ncomms2926.

Masland, R. H. 2001. ‘Neuronal Diversity in the Retina’. *Current Opinion in Neurobiology* 11 (4): 431–36.

Masland, Richard H. 2012a. ‘The Tasks of Amacrine Cells’. *Visual Neuroscience* 29 (1): 3–9.

———. 2012b. ‘The Neuronal Organisation of the Retina’. *Neuron* 76 (2): 266–80. https://doi.org/10.1016/j.neuron.2012.10.002.

Matsuoka, Ryota L., Kim T. Nguyen-Ba-Charvet, Aijaz Parray, Tudor C. Badea, Alain Chédotal, and Alex L. Kolodkin. 2011. ‘Transmembrane Semaphorin Signalling Controls Laminar Stratification in the Mammalian Retina’. *Nature* 470 (7333): 259–63. https://doi.org/10.1038/nature09675.

Matzakos-Karvouniari, Dora, Lionel Gil, Elaine Orendorff, Olivier Marre, Serge Picaud, and Bruno Cessac. 2019. ‘A Biophysical Model Explains the Spontaneous Bursting Behavior in the Developing Retina’. *Scientific Reports* 9 (1). https://doi.org/10.1038/s41598-018-38299-4.

McAllister, A.Kimberley, Donald C. Lo, and Lawrence C. Katz. 1995. ‘Neurotrophins Regulate Dendritic Growth in Developing Visual Cortex’. *Neuron* 15 (4): 791–803. https://doi.org/10.1016/0896-6273(95)90171-X.

McCabe, K. L., E. C. Gunther, and T. A. Reh. 1999. ‘The Development of the Pattern of Retinal Ganglion Cells in the Chick Retina: Mechanisms That Control Differentiation’. *Development* 126 (24): 5713–24.

Mehta, Vandana, and Evelyne Sernagor. 2006. ‘Early Neural Activity and Dendritic Growth in Turtle Retinal Ganglion Cells’. *The European Journal of Neuroscience* 24 (3): 773–86. https://doi.org/10.1111/j.1460-9568.2006.04933.x.

Meister, M., R. O. Wong, D. A. Baylor, and C. J. Shatz. 1991. ‘Synchronous Bursts of Action Potentials in Ganglion Cells of the Developing Mammalian Retina’. *Science (New York, N.Y.)* 252 (5008): 939–43.

Mellström, Britt, Asta Kastanauskaite, Shira Knafo, Paz Gonzalez, Xose M. Dopazo, Ana Ruiz-Nuño, John G. R. Jefferys, et al. 2016. ‘Specific Cytoarchitectureal Changes in Hippocampal Subareas in DaDREAM Mice’. *Molecular Brain* 9 (1). https://doi.org/10.1186/s13041-016-0204-8.

Montague, P. R., and M. J. Friedlander. 1989. ‘Expression of an Intrinsic Growth Strategy by Mammalian Retinal Neurons’. *Proceedings of the National Academy of Sciences of the United States of America* 86 (18): 7223–27.

———. 1991. ‘Morphogenesis and Territorial Coverage by Isolated Mammalian Retinal Ganglion Cells’. *The Journal of Neuroscience: The Official Journal of the Society for Neuroscience* 11 (5): 1440–57.

de Montigny, Jean, Alexandros Iosif, Lukas Breitwieser, Marco Manca, Roman Bauer, and Vasileios Vavourakis. 2020. ‘An in Silico Hybrid Continuum-/Agent-Based Procedure to Modelling Cancer Development: Interrogating the Interplay amongst Glioma Invasion, Vascularity and Necrosis’. *Methods*, January. https://doi.org/10.1016/j.ymeth.2020.01.006.

Morgan, Josh, and Rachel Wong. 2005. ‘Development of Cell Types and Synaptic Connections in the Retina’. In *Webvision: The Organisation of the Retina and Visual System*, edited by Helga Kolb, Eduardo Fernandez, and Ralph Nelson. Salt Lake City (UT): University of Utah Health Sciences Center. http://www.ncbi.nlm.nih.gov/books/NBK11558/.

Mrsic-Flogel, T. D. 2005. ‘Altered Map of Visual Space in the Superior Colliculus of Mice Lacking Early Retinal Waves’. *Journal of Neuroscience* 25 (29): 6921–28. https://doi.org/10.1523/JNEUROSCI.1555-05.2005.

Mumm, Jeff S., Philip R. Williams, Leanne Godinho, Amy Koerber, Andrew J. Pittman, Tobias Roeser, Chi-Bin Chien, Herwig Baier, and Rachel O. L. Wong. 2006. ‘In Vivo Imaging Reveals Dendritic Targeting of Laminated Afferents by Zebrafish Retinal Ganglion Cells’. *Neuron* 52 (4): 609–21. https://doi.org/10.1016/j.neuron.2006.10.004.

Nakamura, Fumio, Kozue Ugajin, Naoya Yamashita, Takako Okada, Yutaka Uchida, Masahiko Taniguchi, Toshio Ohshima, and Yoshio Goshima. 2009. 'Increased Proximal Bifurcation of CA1 Pyramidal Apical Dendrites in *Sema3A* Mutant Mice'. *The Journal of Comparative Neurology* 516 (5): 360–75. https://doi.org/10.1002/cne.22125.

Nakamura, Kazuaki, Chikako Harada, Kazuhiko Namekata, and Takayuki Harada. 2006. 'Expression of Olig2 in Retinal Progenitor Cells'. *Neuroreport* 17 (4): 345–49. https://doi.org/10.1097/01.wnr.0000203352.44998.6b.

Nguyen-Ba-Charvet, Kim Tuyen, and Alain Chédotal. 2014. 'Development of Retinal Layers'. *Comptes Rendus Biologies* 337 (3): 153–59. https://doi.org/10.1016/j.crvi.2013.11.010.

Nicholson, Dw. 1999. 'Caspase Structure, Proteolytic Substrates, and Function during Apoptotic Cell Death'. *Cell Death & Differentiation* 6 (11): 1028–42. https://doi.org/10.1038/sj.cdd.4400598.

Nowakowski, Richard S., Nancy L. Hayes, and M. David Egger. 1992. 'Competitive Interactions during Dendritic Growth: A Simple Stochastic Growth Algorithm'. *Brain Research* 576 (1): 152–56. https://doi.org/10.1016/0006-8993(92)90622-G.

Oda, Yoshio. 1999. 'Choline Acetyltransferase: The Structure, Distribution and Pathologic Changes in the Central Nervous System'. *Pathology International* 49 (11): 921–37. https://doi.org/10.1046/j.1440-1827.1999.00977.x.

Ooyen, Arjen van. 2011. 'Using Theoretical Models to Analyse Neural Development'. *Nature Reviews Neuroscience* 12 (6): 311–26. https://doi.org/10.1038/nrn3031.

Pelt, Jaap van, and Andreas Schierwagen. 2004. 'Morphological Analysis and Modeling of Neuronal Dendrites'. *Mathematical Biosciences* 188 (1–2): 147–55. https://doi.org/10.1016/j.mbs.2003.08.006.

Perry, V. H., and R. Linden. 1982. 'Evidence for Dendritic Competition in the Developing Retina'. *Nature* 297 (5868): 683–85. https://doi.org/10.1038/297683a0.

Petrusca, D., M. I. Grivich, A. Sher, G. D. Field, J. L. Gauthier, M. Greschner, J. Shlens, E. J. Chichilnisky, and A. M. Litke. 2007. 'Identification and Characterization of a Y-Like Primate Retinal Ganglion Cell Type'. *Journal of Neuroscience* 27 (41): 11019–27. https://doi.org/10.1523/JNEUROSCI.2836-07.2007.

Pinzón-Duarte, Germán, Gerard Daly, Yong N. Li, Manuel Koch, and William J. Brunken. 2010. 'Defective Formation of the Inner Limiting Membrane in Laminin B2- and Γ3-Null Mice Produces Retinal Dysplasia'. *Investigative Opthalmology & Visual Science* 51 (3): 1773. https://doi.org/10.1167/iovs.09-4645.

Portera-Cailliau, Carlos, Robby M. Weimer, Vincenzo De Paola, Pico Caroni, and Karel Svoboda. 2005. 'Diverse Modes of Axon Elaboration in the Developing Neocortex'. *PLoS Biology* 3 (8): e272. https://doi.org/10.1371/journal.pbio.0030272.

Puñal, Vanessa M., Caitlin E. Paisley, Federica S. Brecha, Monica A. Lee, Robin M. Perelli, Jingjing Wang, Emily G. O'Koren, et al. 2019. 'Large-Scale Death of Retinal Astrocytes during Normal Development Is Non-Apoptotic and Implemented by Microglia'. Edited by Peter Scheiffele. *PLOS Biology* 17 (10): e3000492. https://doi.org/10.1371/journal.pbio.3000492.

Purves, Dale, Augustine, George J, Fitzpatrick, David, Katz, Lawrence C, LaMantia, Anthony-Samuel, McNamara, James O, and Williams, S Mark. 2008. *Neuroscience*. 4th ed. Sunderland, Mass: Sinauer.

Randlett, Owen, Ryan B. MacDonald, Takeshi Yoshimatsu, Alexandra D. Almeida, Sachihiro C. Suzuki, Rachel O. Wong, and William A. Harris. 2013. 'Cellular Requirements for Building a Retinal Neuropil'. *Cell Reports* 3 (2): 282–90. https://doi.org/10.1016/j.celrep.2013.01.020.

Rapaport, David H., Lily L. Wong, Eric D. Wood, Douglas Yasumura, and Matthew M. LaVail. 2004. 'Timing and Topography of Cell Genesis in the Rat Retina'. *The Journal of Comparative Neurology* 474 (2): 304–24. https://doi.org/10.1002/cne.20134.

Reese, B. E., A. R. Harvey, and S. S. Tan. 1995. ‘Radial and Tangential Dispersion Patterns in the Mouse Retina Are Cell-Class Specific.’ *Proceedings of the National Academy of Sciences* 92 (7): 2494–98. https://doi.org/10.1073/pnas.92.7.2494.

Reese, B. E., B. D. Necessary, P. P. Tam, B. Faulkner-Jones, and S. S. Tan. 1999. ‘Clonal Expansion and Cell Dispersion in the Developing Mouse Retina’. *The European Journal of Neuroscience* 11 (8): 2965–78.

Reese, Benjamin E, and Lucia Galli-Resta. 2002. ‘The Role of Tangential Dispersion in Retinal Mosaic Formation’. *Progress in Retinal and Eye Research* 21 (2): 153–68. https://doi.org/10.1016/S1350-9462(01)00024-6.

Reese, Benjamin E., and Patrick W. Keeley. 2015. ‘Design Principles and Developmental Mechanisms Underlying Retinal Mosaics’. *Biological Reviews of the Cambridge Philosophical Society* 90 (3): 854–76. https://doi.org/10.1111/brv.12139.

Riccomagno, Martin M., Lu O. Sun, Colleen M. Brady, Konstantina Alexandropoulos, Sachiko Seo, Mineo Kurokawa, and Alex L. Kolodkin. 2014. ‘Cas Adaptor Proteins Organize the Retinal Ganglion Cell Layer Downstream of Integrin Signaling’. *Neuron* 81 (4): 779–86. https://doi.org/10.1016/j.neuron.2014.01.036.

Rodriguez, M., J. Choi, S. Park, and S. Sockanathan. 2012. ‘Gde2 Regulates Cortical Neuronal Identity by Controlling the Timing of Cortical Progenitor Differentiation’. *Development* 139 (20): 3870–79. https://doi.org/10.1242/dev.081083.

Rockhill RL, Euler T, Masland RH. Spatial order within but not between types of retinal neurons. Proc Natl Acad Sci U S A. 2000;97(5):2303-2307. doi:10.1073/pnas.030413497

Russell, Thomas L., and Frank S. Werblin. 2010. ‘Retinal Synaptic Pathways Underlying the Response of the Rabbit Local Edge Detector’. *Journal of Neurophysiology* 103 (5): 2757–69. https://doi.org/10.1152/jn.00987.2009.

Sanes, Joshua R., and Richard H. Masland. 2015. ‘The Types of Retinal Ganglion Cells: Current Status and Implications for Neuronal Classification’. *Annual Review of Neuroscience* 38 (July): 221–46. https://doi.org/10.1146/annurev-neuro-071714-034120.

Saurat, Nathalie, Therese Andersson, Navneet A Vasistha, Zoltán Molnár, and Frederick J Livesey. 2013. ‘Dicer Is Required for Neural Stem Cell Multipotency and Lineage Progression during Cerebral Cortex Development’. *Neural Development* 8 (1): 14. https://doi.org/10.1186/1749-8104-8-14.

Scholzen, Thomas, and Johannes Gerdes. 2000. ‘The Ki-67 Protein: From the Known and the Unknown’. *Journal of Cellular Physiology* 182 (3): 311–22. https://doi.org/10.1002/(SICI)1097-4652(200003)182:3<311::AID-JCP1>3.0.CO;2-9.

Sciumè, G., W. G. Gray, F. Hussain, M. Ferrari, P. Decuzzi, and B. A. Schrefler. 2014. ‘Three Phase Flow Dynamics in Tumor Growth’. *Computational Mechanics* 53 (3): 465–84. https://doi.org/10.1007/s00466-013-0956-2.

Sernagor, E., S. J. Eglen, and M. J. O’Donovan. 2000. ‘Differential Effects of Acetylcholine and Glutamate Blockade on the Spatiotemporal Dynamics of Retinal Waves’. *The Journal of Neuroscience: The Official Journal of the Society for Neuroscience* 20 (2): RC56.

Sernagor, E., S. J. Eglen, and R. O. Wong. 2001. ‘Development of Retinal Ganglion Cell Structure and Function’. *Progress in Retinal and Eye Research* 20 (2): 139–74.

Sernagor, Evelyne, Carol Young, and Stephen J. Eglen. 2003. ‘Developmental Modulation of Retinal Wave Dynamics: Shedding Light on the GABA Saga’. *The Journal of Neuroscience: The Official Journal of the Society for Neuroscience* 23 (20): 7621–29.

Shekhar K, Lapan SW, Whitney IE, et al. Comprehensive Classification of Retinal Bipolar Neurons by Single-Cell Transcriptomics. *Cell*. 2016;166(5):1308-1323.e30. doi:10.1016/j.cell.2016.07.054

Shelly, Maya, Laura Cancedda, Byung Kook Lim, Andrei T. Popescu, Pei-lin Cheng, Hongfeng Gao, and Mu-ming Poo. 2011. ‘Semaphorin3A Regulates Neuronal Polarization by Suppressing Axon Formation and Promoting Dendrite Growth’. *Neuron* 71 (3): 433–46. https://doi.org/10.1016/j.neuron.2011.06.041.

Stahl, Andreas, Kip M. Connor, Przemyslaw Sapieha, Jing Chen, Roberta J. Dennison, Nathan M. Krah, Molly R. Seaward, et al. 2010. ‘The Mouse Retina as an Angiogenesis Model’. *Investigative Opthalmology & Visual Science* 51 (6): 2813. https://doi.org/10.1167/iovs.10-5176.

Stone, J., A. Itin, T. Alon, J. Pe’er, H. Gnessin, T. Chan-Ling, and E. Keshet. 1995. ‘Development of Retinal Vasculature Is Mediated by Hypoxia-Induced Vascular Endothelial Growth Factor (VEGF) Expression by Neuroglia’. *The Journal of Neuroscience: The Official Journal of the Society for Neuroscience* 15 (7 Pt 1): 4738–47.

Sümbül, Uygar, Sen Song, Kyle McCulloch, Michael Becker, Bin Lin, Joshua R. Sanes, Richard H. Masland, and H. Sebastian Seung. 2014. ‘A Genetic and Computational Approach to Structurally Classify Neuronal Types’. *Nature Communications* 5 (March): 3512. https://doi.org/10.1038/ncomms4512.

Suzuki, S. C., A. Bleckert, P. R. Williams, M. Takechi, S. Kawamura, and R. O. L. Wong. 2013. ‘Cone Photoreceptor Types in Zebrafish Are Generated by Symmetric Terminal Divisions of Dedicated Precursors’. *Proceedings of the National Academy of Sciences* 110 (37): 15109–14. https://doi.org/10.1073/pnas.1303551110.

Sweeney, Neal T., Kiely N. James, Andreea Nistorica, Ryan M. Lorig-Roach, and David A. Feldheim. 2017. ‘Expression of Transcription Factors Divides Retinal Ganglion Cells into Distinct Classes’. *The Journal of Comparative Neurology* 527 (1): 225–35. https://doi.org/10.1002/cne.24172.

Syed, Mohsin Md., Seunghoon Lee, Shigang He, and Z. Jimmy Zhou. 2004. ‘Spontaneous Waves in the Ventricular Zone of Developing Mammalian Retina’. *Journal of Neurophysiology* 91 (5): 1999–2009. https://doi.org/10.1152/jn.01129.2003.

Tian, Ning, and David R. Copenhagen. 2003. ‘Visual Stimulation Is Required for Refinement of ON and OFF Pathways in Postnatal Retina’. *Neuron* 39 (1): 85–96.

Tissir, Fadel, and André M. Goffinet. 2003. ‘Reelin and Brain Development’. *Nature Reviews Neuroscience* 4 (6): 496–505. https://doi.org/10.1038/nrn1113.

Torben-Nielsen, Benjamin, and Erik De Schutter. 2014. ‘Context-Aware Modeling of Neuronal Morphologies’. *Frontiers in Neuroanatomy* 8: 92. https://doi.org/10.3389/fnana.2014.00092.

Torborg, Christine L., and Marla B. Feller. 2005. ‘Spontaneous Patterned Retinal Activity and the Refinement of Retinal Projections’. *Progress in Neurobiology* 76 (4): 213–35. https://doi.org/10.1016/j.pneurobio.2005.09.002.

Twig, Gilad, Hanna Levy, and Ido Perlman. 2003. ‘Color Opponency in Horizontal Cells of the Vertebrate Retina’. *Progress in Retinal and Eye Research* 22 (1): 31–68.

Valero, C., E. Javierre, J. M. García-Aznar, and M. J. Gómez-Benito. 2013. ‘Numerical Modelling of the Angiogenesis Process in Wound Contraction’. *Biomechanics and Modeling in Mechanobiology* 12 (2): 349–60. https://doi.org/10.1007/s10237-012-0403-x.

Valnegri, Pamela, Sidharth V. Puram, and Azad Bonni. 2015. ‘Regulation of Dendrite Morphogenesis by Extrinsic Cues’. *Trends in Neurosciences* 38 (7): 439–47. https://doi.org/10.1016/j.tins.2015.05.003.

Vaney, D. I. 1994. ‘Territorial Organisation of Direction-Selective Ganglion Cells in Rabbit Retina’. *The Journal of Neuroscience: The Official Journal of the Society for Neuroscience* 14 (11 Pt 1): 6301–16.

Vavourakis, Vasileios, Peter A. Wijeratne, Rebecca Shipley, Marilena Loizidou, Triantafyllos Stylianopoulos, and David J. Hawkes. 2017. ‘A Validated Multiscale In-Silico Model for Mechano-Sensitive Tumour Angiogenesis and Growth’. *PLoS Computational Biology* 13 (1): e1005259. https://doi.org/10.1371/journal.pcbi.1005259.

Wang, Chi-Hwa, and Jian Li. 1998. ‘Three-Dimensional Simulation of IgG Delivery to Tumors’. *Chemical Engineering Science* 53 (20): 3579–3600. https://doi.org/10.1016/S0009-2509(98)00173-0.

Weber, Isabell P., Ana P. Ramos, Paulina J. Strzyz, Louis C. Leung, Stephen Young, and Caren Norden. 2014. ‘Mitotic Position and Morphology of Committed Precursor Cells in the Zebrafish Retina Adapt to Architectural Changes upon Tissue Maturation’. *Cell Reports* 7 (2): 386–97. https://doi.org/10.1016/j.celrep.2014.03.014.

Weiner, G. A., S. H. Shah, C. M. Angelopoulos, A. B. Bartakova, R. S. Pulido, A. Murphy, E. Nudleman, R. Daneman, and J. L. Goldberg. 2019. ‘Cholinergic Neural Activity Directs Retinal Layer-Specific Angiogenesis and Blood Retinal Barrier Formation’. *Nature Communications* 10 (1). https://doi.org/10.1038/s41467-019-10219-8.

Wendling, F., U. Gerber, D. Cosandier-Rimele, A. Nica, J. De Montigny, O. Raineteau, S. Kalitzin, F. Lopes da Silva, and P. Benquet. 2016. ‘Brain (Hyper)Excitability Revealed by Optimal Electrical Stimulation of GABAergic Interneurons’. *Brain Stimulation* 9 (6): 919–32. https://doi.org/10.1016/j.brs.2016.07.001.

Wendling, Fabrice, Pascal Benquet, Fabrice Bartolomei, and Viktor Jirsa. 2016. ‘Computational Models of Epileptiform Activity’. *Journal of Neuroscience Methods* 260 (February): 233–51. https://doi.org/10.1016/j.jneumeth.2015.03.027.

Whitney, I. E., P. W. Keeley, A. J. St. John, A. G. Kautzman, J. N. Kay, and B. E. Reese. 2014. ‘Sox2 Regulates Cholinergic Amacrine Cell Positioning and Dendritic Stratification in the Retina’. *Journal of Neuroscience* 34 (30): 10109–21. https://doi.org/10.1523/JNEUROSCI.0415-14.2014.

Wood, Levi B., Ruowen Ge, Roger D. Kamm, and H. Harry Asada. 2012. ‘Nascent Vessel Elongation Rate Is Inversely Related to Diameter in in Vitro Angiogenesis’. *Integrative Biology* 4 (9): 1081. https://doi.org/10.1039/c2ib20054f.

Wu, Min, Hermann B. Frieboes, Steven R. McDougall, Mark A.J. Chaplain, Vittorio Cristini, and John Lowengrub. 2013. 'The Effect of Interstitial Pressure on Tumor Growth: Coupling with the Blood and Lymphatic Vascular Systems'. *Journal of Theoretical Biology* 320 (March): 131–51. https://doi.org/10.1016/j.jtbi.2012.11.031.

Wyk, M. van, W. R. Taylor, and D. I. Vaney. 2006. 'Local Edge Detectors: A Substrate for Fine Spatial Vision at Low Temporal Frequencies in Rabbit Retina'. *Journal of Neuroscience* 26 (51): 13250–63. https://doi.org/10.1523/JNEUROSCI.1991-06.2006.

Xu, Hong-Ping, Timothy J. Burbridge, Meijun Ye, Minggang Chen, Xinxin Ge, Z. Jimmy Zhou, and Michael C. Crair. 2016. 'Retinal Wave Patterns Are Governed by Mutual Excitation among Starburst Amacrine Cells and Drive the Refinement and Maintenance of Visual Circuits'. *The Journal of Neuroscience* 36 (13): 3871–86. https://doi.org/10.1523/JNEUROSCI.3549-15.2016.

Xu, Nan-Jie, Suya Sun, Jay R Gibson, and Mark Henkemeyer. 2011. 'A Dual Shaping Mechanism for Postsynaptic Ephrin-B3 as a Receptor That Sculpts Dendrites and Synapses'. *Nature Neuroscience* 14 (11): 1421–29. https://doi.org/10.1038/nn.2931.

Yamagata, Masahito, and Joshua R. Sanes. 2008. 'Dscam and Sidekick Proteins Direct Lamina-Specific Synaptic Connections in Vertebrate Retina'. *Nature* 451 (7177): 465–69. https://doi.org/10.1038/nature06469.

Young, Richard W. 1984. 'Cell Death during Differentiation of the Retina in the Mouse'. *The Journal of Comparative Neurology* 229 (3): 362–73. https://doi.org/10.1002/cne.902290307.

Zeck, Günther, Armin Lambacher, and Peter Fromherz. 2011. 'Axonal Transmission in the Retina Introduces a Small Dispersion of Relative Timing in the Ganglion Cell Population Response'. Edited by Steven Barnes. *PLoS ONE* 6 (6): e20810. https://doi.org/10.1371/journal.pone.0020810.

Zhang, Ling-Li, Hemal R. Pathak, Douglas A. Coulter, Michael A. Freed, and Noga Vardi. 2006. 'Shift of Intracellular Chloride Concentration in Ganglion and

Amacrine Cells of Developing Mouse Retina'. *Journal of Neurophysiology* 95 (4): 2404–16. https://doi.org/10.1152/jn.00578.2005.

Zhang, X. M., and X. J. Yang. 2001. 'Regulation of Retinal Ganglion Cell Production by Sonic Hedgehog'. *Development* 128 (6): 943–57.

Zhang, Y., I.-J. Kim, J. R. Sanes, and M. Meister. 2012. 'The Most Numerous Ganglion Cell Type of the Mouse Retina Is a Selective Feature Detector'. *Proceedings of the National Academy of Sciences* 109 (36): E2391–98. https://doi.org/10.1073/pnas.1211547109.

Zeng H, Sanes JR. Neuronal cell-type classification: challenges, opportunities and the path forward. *Nat Rev Neurosci*. 2017;18(9):530-546. doi:10.1038/nrn.2017.85

Zheng, Jijian, Seunghoon Lee, and Z Jimmy Zhou. 2006. 'A Transient Network of Intrinsically Bursting Starburst Cells Underlies the Generation of Retinal Waves'. *Nature Neuroscience* 9 (3): 363–71. https://doi.org/10.1038/nn1644.

Zheng, Ji-jian, Seunghoon Lee, and Z.Jimmy Zhou. 2004. 'A Developmental Switch in the Excitability and Function of the Starburst Network in the Mammalian Retina'. *Neuron* 44 (5): 851–64. https://doi.org/10.1016/j.neuron.2004.11.015.

Zhou, Z. J., and D. Zhao. 2000. 'Coordinated Transitions in Neurotransmitter Systems for the Initiation and Propagation of Spontaneous Retinal Waves'. *The Journal of Neuroscience: The Official Journal of the Society for Neuroscience* 20 (17): 6570–77.

Zubler, Frederic, and Rodney Douglas. 2009. 'A Framework for Modeling the Growth and Development of Neurons and Networks'. *Frontiers in Computational Neuroscience* 3: 25. https://doi.org/10.3389/neuro.10.025.2009.